TN 295
.U4

No. 8936

THE LIBRARY OF CONGRESS

THE LIBRARY OF CONGRESS

IC 8936

Bureau of Mines Information Circular/1983

LIBRARY OF CONGRESS
4
DEC 12 1983
COPY
EXCHANGE & GIFT DIVISION

Electron Microscopy Studies of Explosion and Fire Residues

By Daniel L. Ng, Kenneth L. Cashdollar,
Martin Hertzberg, and Charles P. Lazzara

UNITED STATES DEPARTMENT OF THE INTERIOR

Information Circular 8936

Electron Microscopy Studies of Explosion and Fire Residues

By Daniel L. Ng, Kenneth L. Cashdollar,
Martin Hertzberg, and Charles P. Lazzara

UNITED STATES DEPARTMENT OF THE INTERIOR
James G. Watt, Secretary

BUREAU OF MINES
Robert C. Horton, Director

UNIT OF MEASURE ABBREVIATIONS USED IN THIS REPORT

A	ampere	mbar	millibar
atm	atmosphere	min	minute
° C	degree Celsius	mm	millimeter
° C/sec	degree Celsius per second	msec	millisecond
		µA	microampere
cm	centimeter	µm	micrometer
eV	electron volt	nm	nanometer
g	gram	pct, %	percent
g/m^3	gram per cubic meter	sec	second
J	joule	W	watt
K	kelvin	W/cm^2	watt per square centimeter
keV	kilo electron volt	$W\ cm^{-1}°C^{-1}$	watt per centimeter per degree Celsius
L	liter		

TN295
.U4
no.8936

This publication has been cataloged as follows:

Electron microscopy studies of explosion and fire residues.

(Information circular / Bureau of Mines ; 8936)

Bibliography: p. 61-63.

Supt. of Docs. no.: I 28.27:8936.

1. Mine fires. 2. Mine explosions. 3. Mine dusts—Measurement. 4. Scanning electron microscope. I. Ng, Daniel L. II. Series: Information circular (United States. Bureau of Mines) ; 8936.

TN295.U4 [TN315] 622s [622'.8] 83-600080

CONTENTS

	Page
Abstract	1
Introduction	1
Acknowledgments	2
Experimental apparatus and methods	2
Optical and electron microscope comparison	2
Scanning electron microscope	2
Sample preparation	4
SEM operation	7
Experimental results	11
Dust explosions in an 8-L chamber	11
Pittsburgh coal dust (22-μm) in air	12
Pittsburgh coal dust (22-μm) in 50% O_2	21
Pittsburgh coal dust (2-μm) in air	23
Pittsburgh coal dust (84-μm) in air	23
Particle size effects for Pittsburgh and Pocahontas coals	26
Pocahontas coal dust in air	29
Anthracite dust in air and in 50% O_2	31
Graphite dust in 50% O_2	34
Diamond dust in 50% O_2	37
Pittsburgh coal and rock dust in air	40
Experimental mine dust explosions	43
Mine explosion disaster investigations	47
Dust explosions in a 1.2-L furnace	47
Laser pyrolysis of coal dust	50
Slow heating of coal dust	54
Surface characteristics of bituminous and lignite coals	54
Chemically treated wood	54
Discussion	57
Conclusion	61
References	61

ILLUSTRATIONS

1.	Schematic of scanning electron microscope	3
2.	Electron beam interaction region with specimen	3
3.	Scanning electron microscope	5
4.	SEM and associated instrumentation	6
5.	Typical SEM photograph of dust particles	8
6.	X-ray spectra of coal and Purple K dust	9
7.	Potassium X-ray elemental map of dust in figure 5	10
8.	8-L flammability chamber	11
9.	Coulter Counter size distributions of three classified Pittsburgh coal dusts	12
10.	8-L chamber flammability data for 22-μm Pittsburgh coal dust in air	13
11.	Pressure traces for explosions of 22-μm Pittsburgh coal dust in air	14
12.	Pittsburgh coal dust (22-μm), unburned and a low concentration burned in air	16
13.	Pittsburgh coal dust (22-μm), intermediate concentrations burned in air	17
14.	Pittsburgh coal dust (22-μm), high concentration burned in air	18
15.	Pittsburgh coal dust (22-μm), burned in air	19
16.	Optical micrograph of sectioned Pittsburgh coal dust	20
17.	Flammability data from the 8-L chamber for 22-μm Pittsburgh coal dust in 50% O_2	22

ILLUSTRATIONS--Continued

Page

18. Pressure traces for explosions of 22-μm Pittsburgh coal dust in 50% O_2.... 23
19. Pittsburgh coal dust (22-μm), unburned and burned in 50% O_2..... 24
20. Pittsburgh coal dust (22-μm), burned in 50% O_2..... 25
21. Flammability data from the 8-L chamber for 2-μm Pittsburgh coal dust in air..... 26
22. Unburned Pittsburgh coal dust (2-μm)..... 27
23. Pittsburgh coal dust (2-μm), burned in air..... 28
24. Flammability data from the 8-L chamber for 84-μm Pittsburgh coal dust in air..... 29
25. Pittsburgh coal dust (84-μm), unburned and burned in air..... 30
26. Lean flammable limit for Pittsburgh and Pocahontas coals as a function of particle size..... 31
27. Flammability data from the 8-L chamber for 13-μm Pocahontas coal dust in air..... 32
28. Pocahontas coal dust (13-μm), unburned and burned in air..... 33
29. Flammability data from the 8-L chamber for anthracite in air and in 50% O_2 34
30. Anthracite dust, unburned and burned in air..... 35
31. Anthracite dust, burned in 50% O_2..... 36
32. Flammability data from the 8-L chamber for graphite and diamond dust in 50% O_2..... 37
33. Graphite dust (4-μm), unburned and burned in 50% O_2..... 38
34. Diamond dust (2-μm), unburned and burned in 50% O_2..... 39
35. X-ray spectra of diamond and match particles..... 40
36. Flammability data from the 8-L chamber for a Pittsburgh coal and rock dust mixture..... 41
37. Unburned Pittsburgh coal and rock dust mixture..... 42
38. X-ray spectra of limestone rock and coal particles..... 43
39. Pittsburgh coal and rock dust mixture, burned in air..... 44
40. Unburned Pittsburgh coal and rock dust mixture..... 45
41. Pittsburgh coal and rock dust, postexplosion sample from the Bruceton Experimental Mine..... 46
42. 1.2-L furnace and rapid sampling system..... 47
43. Pressure and thermocouple recorder traces from an explosion in the 1.2-L furnace..... 48
44. Dust cloud thermal ignition data from the 1.2-L furnace for 55-μm Pittsburgh coal in air..... 49
45. Unburned Pittsburgh coal dust (55-μm)..... 50
46. Pittsburgh coal dust (55-μm), heated in the 1.2-L furnace but before thermal ignition..... 51
47. Pittsburgh coal dust (55-μm) after an explosion in the 1.2-L furnace..... 52
48. Laser-pyrolyzed 84-μm Pittsburgh coal at various heating times..... 53
49. Pittsburgh coal dust slowly heated in a furnace at various temperatures... 55
50. Comparison of surface characteristics of bituminous and lignite coals..... 56
51. Relative distribution of phosphorus as a function of distance from the surface, in oak timber chemically treated with NCX inhibitor..... 57
52. Relative distribution of phosphorus as a function of distance from the surface, in chemically treated oak timber after charring..... 58

TABLE

1. X-ray energies of some common chemical elements..... 8

ELECTRON MICROSCOPY STUDIES OF EXPLOSION AND FIRE RESIDUES

By Daniel L. Ng,[1] Kenneth L. Cashdollar,[2] Martin Hertzberg,[3]
and Charles P. Lazzara[3]

ABSTRACT

This Bureau of Mines report describes the results of scanning electron microscopic (SEM) studies of the combustion residues of carbonaceous dust particles resulting from explosions and thermal ignitions in laboratory and full-scale mine tests. The dusts studied varied widely in rank and volatility: Pittsburgh seam bituminous coal (35% volatility), Pocahontas seam bituminous coal (16% volatility), anthracite (7% volatility), graphite, and diamond. The most systematic explosion studies were performed in an 8-L chamber with narrow size distributions of Pittsburgh coal dust with surface mean diameters of 2, 22, and 84 μm. Experiments were conducted mainly in air, with some data obtained in 50% O_2. Observations of the bituminous coal explosion residues showed particles with rounded edges, particles with blowholes, and some cenospheres. The lower volatility dust residues showed fewer changes from the original, unburned dust.

In addition to the experimental studies, results of SEM observations of residues from a mine explosion disaster are reported. Comparison of such residues with those from the laboratory and experimental mine explosions can help investigators determine the extent of dust participation in the disaster and in identifying the possible ignition sources.

INTRODUCTION

It has been over 70 years since the Bureau of Mines was created by Congress and given specific authority to inquire into the causes of gas and dust explosions in U.S. mines. In that period, over 1,000 mine explosion disasters have been investigated, and an even larger number of experimental dust explosion tests have been conducted by the Bureau.

Since 1979, the scanning electron microscope (SEM) facility has been used to study the microscopic structure of dust residues from such explosions, to gain fundamental data on the character of these residues and provide a basis for determining the extent of dust participation in specific mine disasters. Some of the studies of laboratory-scale explosions reported herein are systematic; others are only examples of the capability of the instrumentation and methodology for assisting in field investigations.

[1]Research physicist.
[2]Physicist.
[3]Supervisory research chemist.
Pittsburgh Research Center, Bureau of Mines, Pittsburgh, PA.

ACKNOWLEDGMENTS

The authors wish to acknowledge the contributions of R. S. Conti, W. T. Corpus, and J. Leff (all of the Pittsburgh Research Center) to the experimental work in this report. In particular, the authors wish to thank R. S. Conti for permission to use his thermal ignition data from the 1.2-L furnace (8).[4] Special acknowledgment is made to P. J. Street of the Central Electricity Generating Board in the United Kingdom for permitting the use of his optical microscopy observations (35) of coal dust residues from the Bureau's laboratory-scale explosions.

EXPERIMENTAL APPARATUS AND METHODS

OPTICAL AND ELECTRON MICROSCOPE COMPARISON

In all microscopy the important quantity is the resolution. In an optical microscope (3, 9), the diffraction-limited resolution for visible light ($\lambda \cong 550$ nm) is about 350 nm in air, or about 250 nm for an oil-immersed lens. The resolving power of the unaided human eye is about 2 min of arc, which corresponds to about 0.2 mm at a distance of 25 cm. Therefore, the maximum practical magnifications for the optical microscope are about 500 in air and 700 in oil.

In general, the resolution can be improved by going to light of shorter wavelength. According to quantum physics (2), a particle such as an electron has a wavelength that is much shorter than that of visible light. The de Broglie wavelength λ is related to the particle's energy by

$$\lambda = \frac{h}{p} = \frac{h}{(2mE)^{1/2}} , \qquad (1)$$

where h is Planck's constant, p is the particle momentum, m is the particle mass, and E is the particle energy. For example, a 30-keV electron has a de Broglie wavelength of about 0.007 nm, and a 200-keV electron corresponds to a wavelength of 0.003 nm. Electron microscopes (11, p. 3; 39, p. 13; 40) were made to take advantage of the shorter wavelengths of electrons to achieve higher resolution than optical microscopes. The theoretical resolution for a scanning electron microscope operating at 30 keV is about 0.4 nm. In practice the resolution is limited by the beam spot size, which is 1 to 2 nm. This corresponds to practical maximum magnifications of 50,000 to 100,000 for the SEM.

Compared to the glass lenses of optical microscopes, the electromagnetic lenses of the SEM have much greater spherical and chromatic aberrations (11, pp. 32-40; 39, ch. 4). To overcome these imperfections, the SEM operates at a large f number (or small cone angle). This also results in a large depth of field (about 100 times the resolution) for the SEM.

SCANNING ELECTRON MICROSCOPE

Details of the image formation system of the SEM appear in the literature (11, ch. 4; 40), but a brief description is given here. The major components of the SEM are illustrated in figure 1. The filament is the source of electrons, which are accelerated by a high voltage. Condenser and objective lenses focus the electrons to a fine spot on the sample. The scan generator produces a signal sweeping in synchronism both the electron beam inside the microscope and the electron beam inside the cathode ray tube (CRT), on which the image of the sample under study is displayed. The image is produced by modulating the intensity of the CRT beam with signals coming from the output of the video amplifier. Input signals to the video amplifier are usually from secondary electrons produced by the interaction between the electron beam and the sample. The strength of the interaction varies from point to point

[4] Underlined numbers in parentheses refer to items in the list of references at the end of this report.

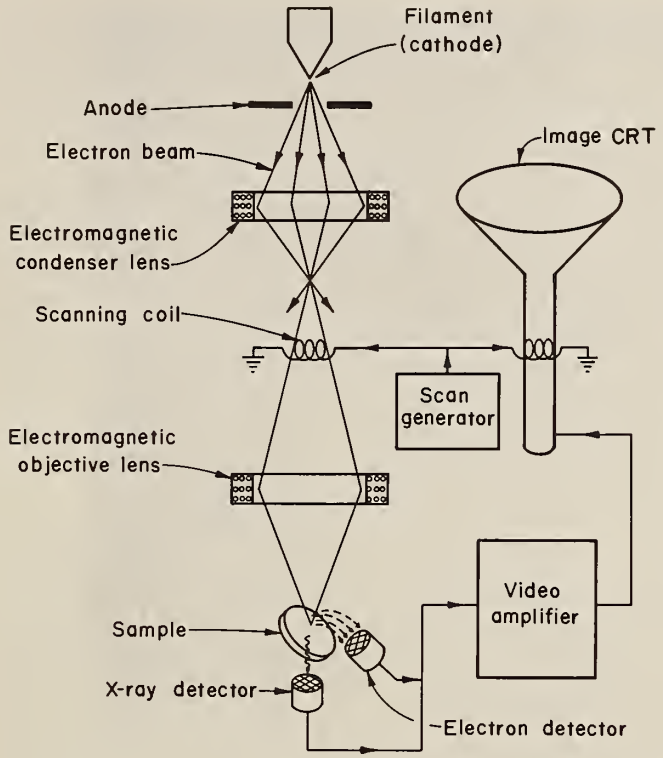

FIGURE 1. - Schematic of scanning electron microscope.

according to the local topography and chemical composition of the sample. For example, the production of secondary electrons varies according to the sample material and the angle between the beam and the sample surface. Image production is by a one-to-one correspondence between the position scanned by the focused electron beam on the sample and the position traversed by the electron beam in the CRT. The amplitude modulation is the variation in secondary electron production rate with respect to position. Thus, the secondary electrons are collected at the detector, where they strike a scintillator to produce flashes of light. This light signal is guided by a light pipe to a photomultiplier, which converts it into electrical signals suitable for input to the video amplifier. The magnification is simply the ratio of the distances scanned by the two electron beams: the one in the microscope, the other in the video display.

Though secondary electrons are most often employed to produce images in an SEM, other information-carrying signals such as backscattered electrons and X-ray photons can also be used as input signals to the video amplifier to produce images. All these signals are produced as a result of the interactions between the electron beam and the specimen, as shown schematically in figure 2. The secondary electrons are most often used in high-resolution imaging because they are produced from an area of the sample only slightly larger in diameter than the focused spot of the beam, and they originate from no deeper than 5 to 50 nm. The other signals originate from a much larger volume of the beam sample interaction region, resulting in poorer resolution. In spite of their lower resolution, images obtained from these other signals are useful because they contain information of a different kind. For example, X-ray-produced SEM micrographs give the spatial distribution of a chemical element of interest. This will be discussed in more detail in the next section.

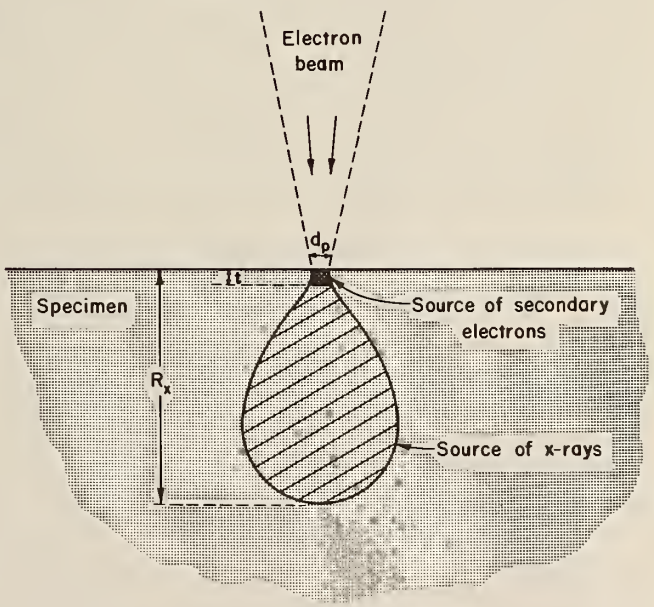

FIGURE 2. - Electron beam interaction region with specimen.

The Bureau of Mines Pittsburgh Research Center is engaged in mine health and safety research. One such area of research is the prevention of fires and explosions in mining-related activities. The Center has a JEOL[5] JSM U3 scanning electron microscope equipped with a solid state X-ray detector and multichannel analyzer to perform energy-dispersive X-ray analysis. Figure 3 is a photograph of the SEM with the electron gun (filament source) at the top, condenser lens and scanning coils in the middle, and sample manipulation controls at the bottom. Figure 4 shows the SEM, console, and associated instrumentation.

SAMPLE PREPARATION

Sample preparation for scanning electron microscopy is very simple. If the sample is conductive, such as a metal or semiconductor, and if it is small enough to be introduced into the vacuum chamber below the objective lens, no preparation is necessary at all. However, care should be taken to sufficiently degas the sample so that it will not disturb the relatively high vacuum (about 10^{-9} bar) requirement of the SEM. It is always good practice to have clean samples in the SEM, because dirty samples often give off hydrocarbon molecules which, under intense electron bombardment, produce contamination on the surface as a result of hydrocarbon cracking and subsequent polymerization into a carbon layer.

Observation of insulating (nonconductive) materials can be done without much preparation, as in the conductive material case; however, the image quality will suffer from charging effects. Charging is due to the accumulation of beam electrons absorbed by the insulator because there is no conducting path for the absorbed electrons to dissipate to the electrical ground. This electron accumulation leads to space charge regions on the sample which can actually deflect the incident electron beam. This results in sudden streaks of bright lines and distortion in the CRT image. The buildup of charges also changes the secondary electron emission probability and hence the signal strength. Methods to overcome charging effects usually involve operating the SEM at a low accelerating voltage or coating the sample with a layer of conductive material. Lowering the accelerating voltage usually results in lower resolution. The better method is to apply a thin layer of conductive material on the insulator's surface. The metal most often employed is an alloy of gold and palladium, and the thickness of the coating can be between 10 and 100 nm.

In addition to minimizing charging effects in SEM images, the application of a conductive coating also reduces damage to the sample due to heating produced by the electron beam. This is particularly important in heat-sensitive specimens such as biological samples. It can be shown (11, p. 513) that the rise in temperature ΔT due to the impact of an electron beam of current i (in μA) with energy E_o (in keV) and a beam diameter d_p (in μm) on a material with thermal conductivity k (in W $cm^{-1}°C^{-1}$) is

$$\Delta T = \frac{4.8\ E_o\ i}{k\ d_p} . \qquad (2)$$

The rise in temperature is only about 10° C for metals but can be as high as 1,000° C for plastics. Thus, for example, an aluminum coating 20 nm thick can reduce the value of ΔT from 1,430° C to 515° C for some nonconductive samples (11, p. 513).

Coal can sometimes be classified as an electrical semiconductor, but in scanning electron microscopy, it behaves more like an insulator. Uncoated coal samples exhibit strong charging effects. To obtain quality images, they need to be conductively coated.

If the material to be studied contains a large quantity of water, it is necessary to have the water removed. This can be done simply by drying. If the features of interest are delicate, special

[5]Reference to trade names is made for identification only and does not imply endorsement by the Bureau of Mines.

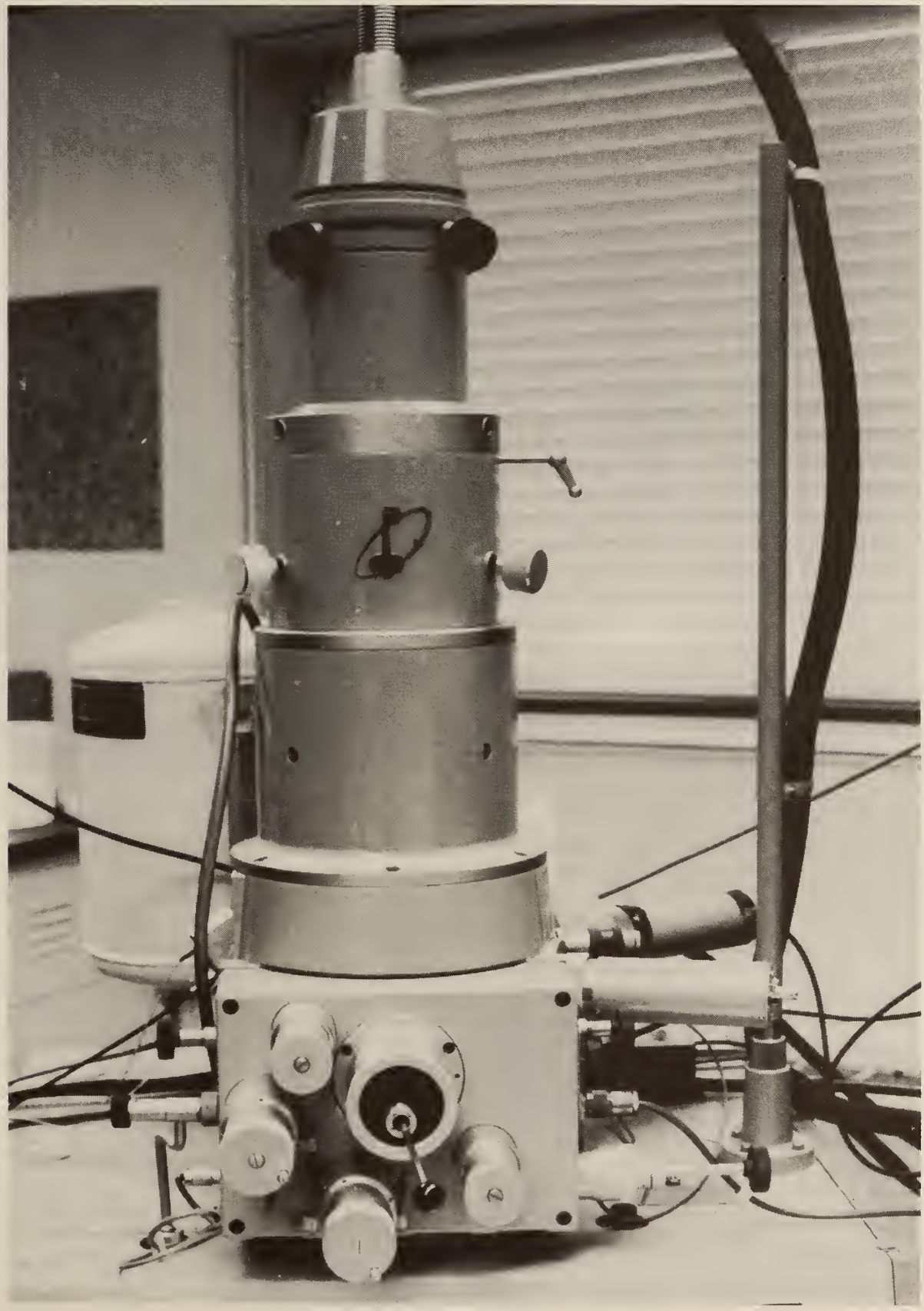

FIGURE 3. - Scanning electron microscope.

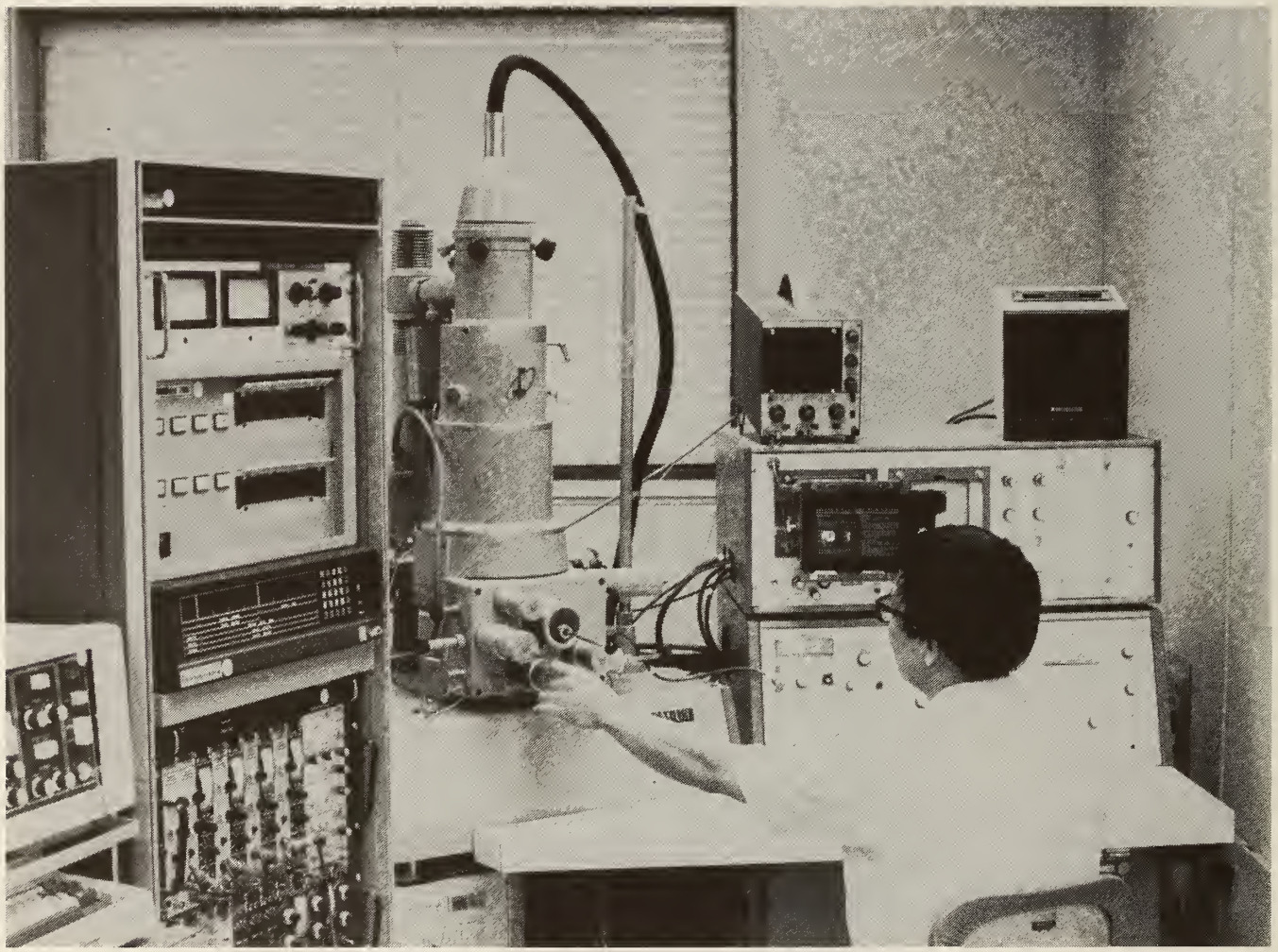

FIGURE 4. - SEM and associated instrumentation.

methods of drying have to be used, because ordinary drying occurs by transport of water across a liquid-vapor interface. Surface tension of the receding liquid can exert a very large force per unit area, and the result is that delicate microscopic features can be squashed and collapsed. To prevent this, special methods such as freeze drying and critical point drying should be used (11, pp. 495-505). Since these considerations are unimportant with respect to coal dust and other dusts whose investigations are reported here, we will not go into detail concerning them. It is generally sufficient to air-dry coal dust samples.

Samples are collected in several ways as will be described. Once they have been collected, they are prepared essentially as follows. Dust samples are transferred using a microspatula onto a vinyl tape coated with adhesive on both sides. This tape is chosen over a similar cellophane tape because of its low outgas characteristics, which make it compatible with the SEM's high-vacuum requirement. The tape is mounted on an 18-mm-diameter copper or aluminum disc. If necessary, the quantity of dust sampled can be determined by weighing with an electronic balance. For solid samples, the sample is cut to a suitable size (usually less than 25 mm in maximum dimension) and mounted similarly.

The application of a layer of conductive material is usually accomplished by

sputtering or evaporative deposition. Sputtering is done by placing the prepared sample inside the chamber of a sputter coater. The chamber is evacuated to a low pressure. By using a leak valve, a steady vacuum of about 0.13 mbar is maintained. A plasma discharge is produced by the application of a high voltage between the sample and a metallic anode. Positive ions that are produced by the gas discharge impact on the anode and sputter a metallic coating from the anode target (usually a gold and platinum alloy) onto the sample. The thickness of the metallic layer can be controlled by varying the magnitude of the discharge current, the voltage setting, and the length of sputtering time according to calibration curves. Coating by evaporative deposition is done inside a vacuum evaporator. A measured quantity of Au-Pd alloy wire is placed inside a tungsten wire basket, which is supported on electrodes. The sample is placed on a planetary rotating platform below the wire basket, and the whole assembly is enclosed inside a bell jar evacuated to a vacuum of about 10^{-6} mbar. A high current (20 to 30 A) is passed through the tungsten basket to melt and then evaporate the Au-Pd wire. A fine mist of vaporized metal is produced which condenses onto the sample to produce the desired coating. Coating by the evaporation of a metal is the preferred method when working with heat-sensitive materials.

SEM OPERATION

When a sample is studied in the SEM, it is observed at a magnification appropriate for the information to be sought, usually from 100 X to 10,000 X. For magnifications above 500 X, it is the higher resolving power of the SEM that makes it more useful than the optical microscope. Below 500 X, its larger depth of focus allows one to observe features not possible with the light microscope. There are usually two imaging modes for the SEM imaging, the slow scan mode and the TV scan mode. In the TV mode, the TV scan generator sweeps the electron beam over the observed surface about 30 times a second; i.e., 30 TV picture frames are presented to the eye in 1 sec. This rapid scan speed allows the eye to follow motions from one region of the sample to another because the image follows the sample movement instantaneously. This is not the case in the slow scan mode, where it takes up to tens of seconds to scan a particular region. However, the ability to rapidly scan a region of the sample at the TV rate is achieved with a loss of resolution and image quality. This is so because, in the fast TV scan mode, the electron beam does not dwell on a spot long enough to collect enough electrons to obtain a good signal-to-noise ratio. Therefore, in the TV scanning mode, the signal-to-noise ratio must be improved by increasing the beam spot size. This increases the number of electrons striking the sample but decreases the resolution. To increase the signal-to-noise ratio and at the same time maintain high resolution requires a longer sampling time. This is achieved in the slow scan mode, which is the mode one employs to photograph the image. A recording time of 50 to 100 sec is typical. Consequently, the normal practice is to use the TV mode to locate the features of interest and then to switch over to the slow scan mode and adjust the various electronic controls to obtain the best contrast, brightness, and image sharpness. The image is then recorded photographically on Polaroid type 52 positive or type 55 positive-negative film. Sometimes it is advantageous to record stereo pairs, which are two micrographs of the same area, viewed 5° to 7° apart by rotating the tilt of the specimen stage. When this pair of micrographs is viewed with the aid of stereo viewer, a lifelike three-dimensional-appearing image of the original object results.

As discussed previously, the images produced by secondary electrons have the highest resolution. All of the SEM photomicrographs in this report were made using an accelerating voltage of 25 keV for the incident electron beam and secondary electrons for imaging.

Figure 5 is a typical SEM photomicrograph of a sample containing coal dust and a dry chemical fire extinguishing agent called Purple K (fluidized $KHCO_3$). Often times it is desirable to know the chemical composition of a sample, or where in the sample a given element or impurity is located. A nondestructive method of determining the chemical or elemental composition of a sample is the electron probe microanalyzer (EPMA). This is an instrument in which the sample is bombarded with electrons of sufficiently high energy (i.e., with kinetic energy higher than the bonding energy of the inner orbital electrons of the atoms making up the sample) so that some of these orbiting electrons will be ejected from the atom, leaving it in an excited state. The excited atom relaxes by having an electron from an outer orbit fall into the vacancy left behind by the ejected electron. According to quantum theory, the difference in energy between the initial and final state of the electron making this transition causes the emission of a characteristic X-ray, called the K, L, or M line depending on whether the vacancy was created in the K, L, or M shell (11, pp. 69-78; 39, pp. 243-247). (K, L, M, etc., are names given to the electrons in different orbits around the atom.) Using suitable instrumentation, these X-rays are collected and analyzed by the EPMA. It was discovered by Moseley (11, p. 74; 28) in 1913 that the characteristic X-rays are related to the atomic number Z of the bombarded atoms by the following equations:

$$\lambda = \frac{K}{(Z-\sigma)^2} \tag{3}$$

or

$$E \propto (Z-\sigma)^2 \tag{4}$$

where λ and E are the wavelength and energy of the X-ray photons and K and σ are semiempirical constants. Thus the presence of X-rays of a particular energy indicates the presence of an atom of a particular atomic number, i.e., a particular element. In an electron probe microanalyzer, the concentration of elements in a sample can be quantitatively determined from the intensity of the lines. The X-ray energies of the common elements of interest are found in table 1. The K_α-line results from an electron falling from the L-shell to the K-shell, and the K_β-line results from an electron falling from the M-shell to the K-shell.

FIGURE 5. - Typical SEM photograph of dust particles.

TABLE 1. - X-ray energies of some common chemical elements

Atomic number (Z)	Name	Symbol	Energy, keV	
			K_α	K_β
11	Sodium.....	Na	1.04	1.07
12	Magnesium...	Mg	1.25	1.30
13	Aluminum....	Al	1.49	1.55
14	Silicon.....	Si	1.74	1.83
15	Phosphorus..	P	2.01	2.14
16	Sulfur.....	S	2.31	2.46
17	Chlorine....	Cl	2.62	2.82
19	Potassium...	K	3.31	3.59
20	Calcium.....	Ca	3.69	4.01
22	Titanium....	Ti	4.51	4.93
24	Chromium....	Cr	5.41	5.95
26	Iron.....	Fe	6.40	7.06
27	Cobalt.....	Co	6.92	7.65
28	Nickel.....	Ni	7.47	8.26
29	Copper.....	Cu	8.04	8.90

As mentioned earlier, the SEM has an electron beam-specimen interaction region which produces X-rays in addition to secondary electrons. The mechanism for the X-ray production is exactly the same as in the electron probe microanalyzer. If these X-rays are collected and analyzed according to wavelength or, equivalently, according to energy, the SEM is actually an EPMA. Almost all SEM's are equipped with X-ray analyzers. There are two kinds of X-ray analyzer in use: wavelength-dispersive and energy-dispersive analyzers. The wavelength-dispersive analyzer (11, pp. 263-274; 39, pp. 252-256) uses crystals to diffract the X-rays according to Bragg's law. The diffracted X-rays are detected using a proportional counter, and the elements are identified according to Moseley's law (equation 3). For the energy-dispersive analyzer (11, pp. 274-281; 39, pp. 265-272), X-rays pass through a thin beryllium window into an evacuated chamber where they are detected by a liquid-nitrogen-cooled, lithium-drifted silicon crystal. When X-ray photons are absorbed in the detector's crystal, electron-hole pairs are created and are collected by an applied electric field to produce pulses which are amplified and then processed by a multichannel analyzer where they are sorted according to voltages. The pulse voltages are proportional to the energy of the incident X-rays. The energy-dispersive analyzer cannot detect X-rays of elements whose atomic number Z is less than 11 because the detector window,

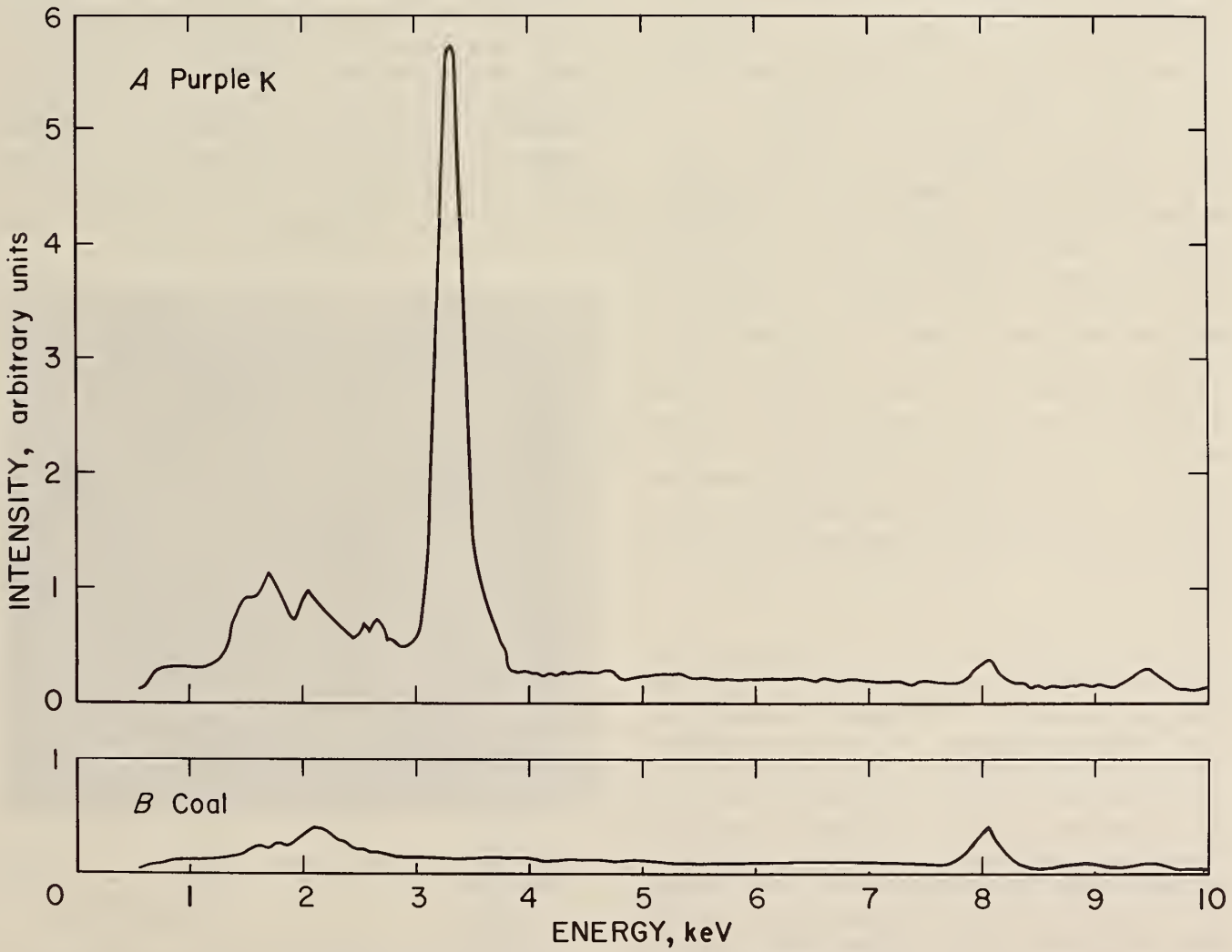

FIGURE 6. - X-ray spectra of coal and Purple K dust.

usually made of beryllium about 10 μm thick, strongly absorbs these lower energy X-rays. Also the characteristic X-rays of the elements of $4 < Z < 7$ are only about 100 to 150 eV apart, and the energy resolution of solid state detectors is usually not sufficient to resolve these X-rays. The Bureau detector has a resolution of about 180 eV at the 6.40-keV iron line. To analyze X-rays below atomic number Z = 11 (i.e., for carbon, oxygen, nitrogen, etc.), the wavelength-dispersive analyzer is recommended.

If all the X-rays emitted from the sample are collected and analyzed by energy, spectra like those shown in figure 6 are obtained. These particular X-ray spectra are from two of the dust particles shown in figure 5. Qualitative analysis of the elemental composition of the sample is trivially done by noting whether X-rays of energies corresponding to a particular element are present in the spectrum. The strong line at 3.3 keV in figure 6*A* is the potassium K_α-line; this must be a Purple K particle since Purple K is composed mainly of potassium bicarbonate, $KHCO_3$. The other particle has no strong lines (except for the K-line of copper at 8.0 keV due to the copper sample holder and the M-lines of gold and platinum at about 2.1 keV from the coating). The other particle must therefore be a coal particle, since its main component, carbon, has too low an energy to be observed. With suitable instrumentation, such as a small dedicated computer, quantitative information concerning the concentration of elements could also be obtained.

The X-ray spectrum can be accumulated with the electron beam scanning over the entire region of the sample being examined by the SEM, or with the electron beam directed towards a single spot on the sample. The spectrum accumulated in the scanning mode would give an indication of the elements that are present in the group of particles in the region under observation, whereas that of the spot mode would give a spectrum of only that particle or portion of the particle that is present in the localized spot. Comparison of spectra from different particles would give semiquantitative information as to the relative concentration of elements in each by comparing the relative intensities of their X-ray lines.

A map of the distribution of a particular element throughout the sample can be obtained by collecting only the X-rays that originate from the element of interest and using these signals instead of the secondary electrons to produce an image. For example, figure 7 is an X-ray map using only the potassium K-line, 3.3 keV, shown in figure 6*A*. A dot in figure 7 represents the presence of potassium atoms. By comparing figures 5 and 7, the various particles shown in figure 5 can be identified as either Purple K or coal, since only the Purple K particles appear in figure 7. Elemental X-ray maps provide information about the spatial distribution of the element of interest in relation to the rest of the sample. Elemental distribution measurements are not limited to potassium but can be made for any other element by selecting its characteristic line.

FIGURE 7. - Potassium X-ray elemental map of dust in figure 5.

EXPERIMENTAL RESULTS

DUSTS EXPLOSIONS IN AN 8-L CHAMBER

These studies are part of the research activities of the Bureau of Mines and were performed in conjunction with studies of the flammability of coals and other dusts. Laboratory-scale studies of dust flammability in an 8-L chamber have been reported previously (13, 16-17). A schematic drawing of the chamber and air dispersion tank is shown in figure 8. The drawing shows the position of an optical dust probe (7, 23), pressure transducer, oxygen sensor, dust cup, and ignition point. The top plate of the chamber is usually fitted with a sapphire window assembly (not shown), through which the infrared radiance of the explosion can be measured (4-5). The normal procedure is to spread a measured mass of dust uniformly around the disperser cone. The top plate is then bolted on, and the chamber is partially evacuated to about 0.2 atm. The air-dispersion tank is pressurized (to about 6 atm); when the solenoid valve between it and the preevacuated chamber is opened, an intense air-jet impulse is injected. This air impulse disperses the dust, mixes with it, and raises the chamber pressure to 1.0 atm absolute. The dispersion air pulse lasts for 0.2 sec, and after another 0.1-sec delay to allow for more uniform dispersion, the ignition source is energized. The standard ignitor is an array of four electrically activated, pyrotechnic matches, which deposit their energy (140 J) in about 0.05 sec. If the mixture is flammable, the developing pressure and infrared spectral radiance are monitored. When flame propagation is complete and after the combustion products cool, the residual oxygen content is measured and dust or gas samples may be collected for analysis.

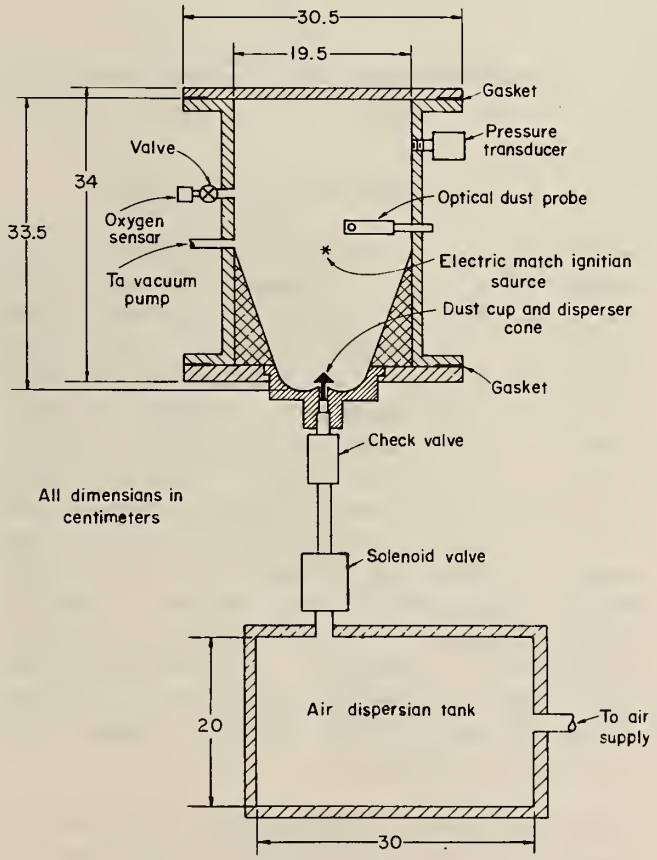

FIGURE 8. - 8-L flammability chamber.

Dust flammability has been studied as a function of dust volatility, particle size, initial oxygen concentration, and added inhibitor dusts. Size distributions for three classified Pittsburgh seam coal dusts used in these studies are shown in figure 9. The data are from Coulter Counter size analyses and are plotted as a surface-area-weighted distribution using a semilogarithmic plot. The smallest dust has a surface mean diameter $\bar{D}_s$ = 2.2 μm, a mass mean diameter $\bar{D}_w$ = 2.6 μm, and a geometric standard deviation σ_g = 1.46. The intermediate-size dust has $\bar{D}_s$ = 22 μm, $\bar{D}_w$ = 32 μm, and σ_g = 1.82. The coarsest dust has $\bar{D}_s$ = 84 μm, $\bar{D}_w$ = 89 μm, and σ_g = 1.14. The two finer size distributions were obtained with a centrifugal classifier, and the coarsest dust was sieve-classified (200 × 140 mesh). The data in figure 9 are for unagglomerated dusts since they were dispersed in alcohol for the Coulter Counter size analyses. When dispersed in air, the dusts tend to agglomerate to somewhat larger sizes (7, 16), but this agglomeration does not affect the flammability behavior significantly. These narrow size distributions of coal dust make it much easier to observe with the SEM any size changes that might occur during an explosion.

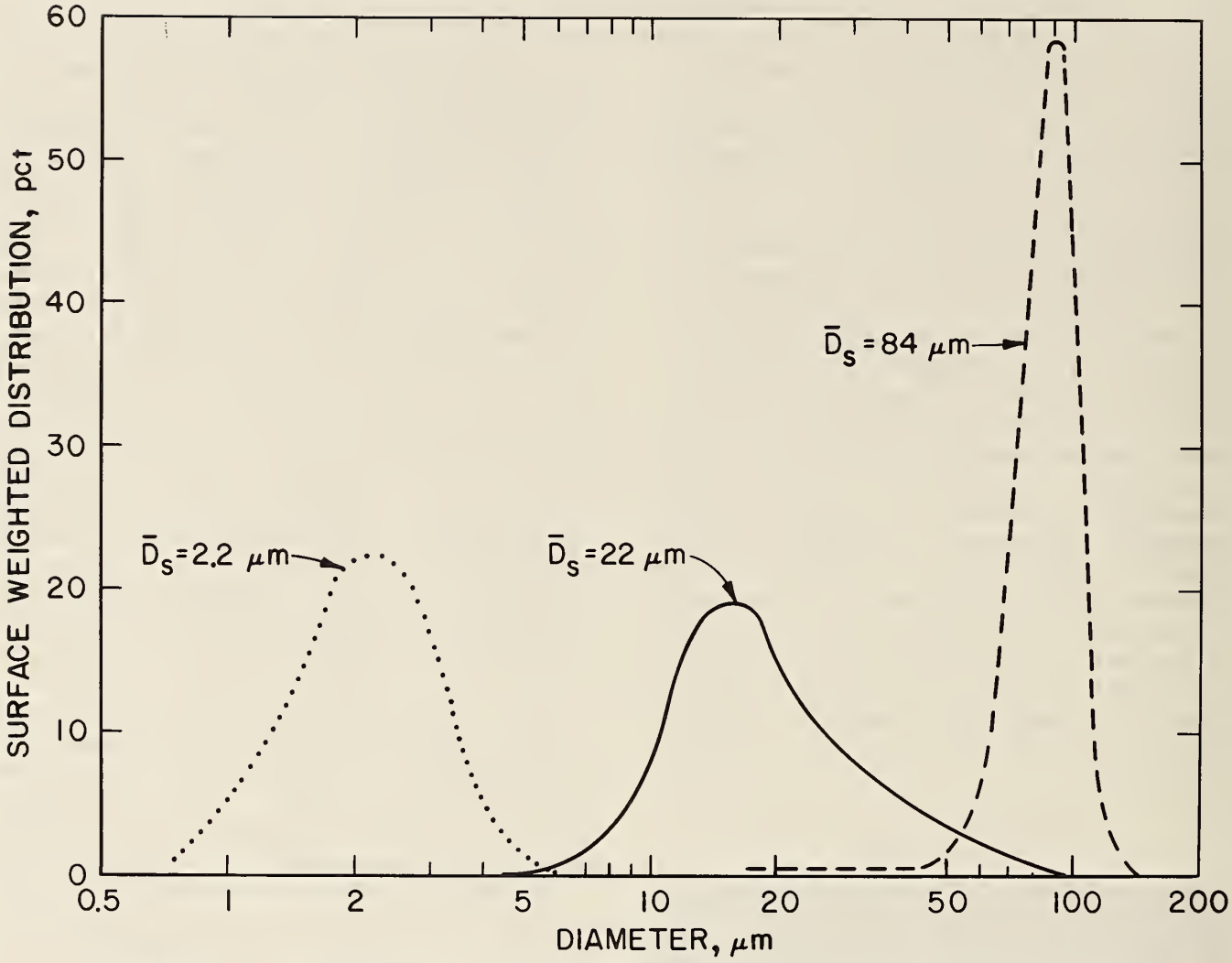

FIGURE 9. - Coulter Counter size distributions of three classified Pittsburgh coal dusts.

Pittsburgh Coal Dust (22-μm) in Air

Figure 10 shows flammability data for explosions of the 22-μm Pittsburgh seam coal dust in air in the 8-L chamber. This coal had an "as received" volatility of about 35% according to the ASTM D3175 standard test (1), although the real volatility under the faster heating rates of explosions would probably be higher (19). The data include temperatures, oxygen consumed, and pressures as a function of dust concentration. The measured pressure ratio in figure 10*C* was the maximum explosion pressure (absolute) divided by the initial pressure (about 1 atm absolute), with a small correction for the pressure rise caused by the matches themselves. The data show no flame propagation, and therefore no pressure rise, below 100 g/m^3. Between 125 and 175 g/m^3 there is a rapid increase in the explosion pressure. In previous publications (13, 16), the authors chose a pressure ratio of 2.0 as a criterion of significant flame propagation. That criterion gives a lean flammable limit of 130 g/m^3 for Pittsburgh coal dust. At the higher concentrations, the pressure curve levels off as all the oxygen in the air is consumed. This is shown in figure 10*B*, which is a graph of the decimal fraction of the oxygen in the air that is consumed during the explosion. The decimal fraction was calculated from the measured amount of oxygen left in the chamber after the explosion.

The pyrometer temperatures shown in figure 10*A* were calculated at the time of

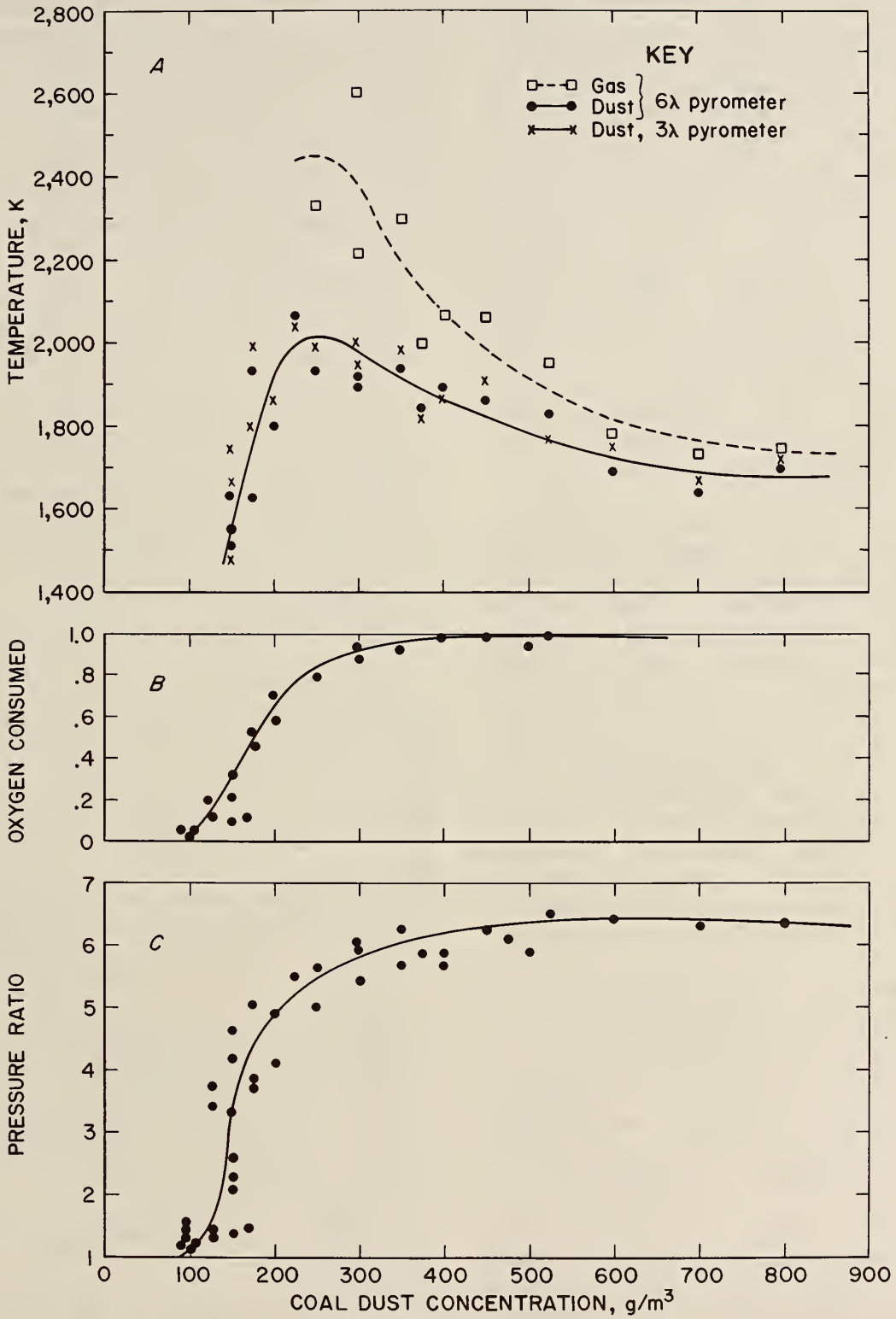

FIGURE 10. - 8-L chamber flammability data for 22-μm Pittsburgh coal dust in air.

maximum radiance for each explosion. The particle temperatures were calculated from the infrared continuum radiance measured by a three-wavelength (3λ) pyrometer (4-5) and by a six-wavelength (6λ) pyrometer (5-6). The 6λ pyrometer also measured the gas temperature in the explosion by observing the 4.4-μm CO_2 emission band radiance. For the data of figure 10, the maximum dust particle temperature and the maximum gas temperature occur at a concentration of about 250 g/m^3; this value is close to the concentration at which the burning velocity is a maximum for dusts in this size range (18, 33-34). It is also approximately the concentration at which the amount of combustible volatiles from the coal is at a stoichiometric ratio with respect to the air. The temperatures measured in this constant-volume chamber are higher than those of atmospheric flames due to adiabatic compression. The gas temperatures for these explosions are from one hundred to several hundred degrees higher than the dust particle temperatures. This tends to confirm a combustion mechanism in which the coal particles devolatilize, generating hydrocarbon gases that burn in the gas phase. The dust particles remain cooler because of their continuing endothermic pyrolysis and the fact that the seat of the exothermic reaction is in the gas phase at a significant distance from the particle.

Dust samples for SEM analysis were collected for numerous explosions of the 22-μm Pittsburgh coal dust in the 8-L chamber. Pressure traces as a function of time for several of these explosions are shown in figure 11. As the concentration increases, both the maximum pressure and the rate of pressure rise increase.

To answer the question of what actually happens to each coal dust particle during the course of an explosion, one must compare the features and appearances of dusts before and after the explosion. After an explosion has been set off in the 8-L vessel, ample time is allowed for the dusts to settle. A small quantity of dust is then collected with a spatula, usually from the surface layer at the bottom of the vessel. Sometimes at low dust concentrations, almost all the dust appears to be consumed. In that case, vinyl tape coated with adhesive on both sides is applied to the wall of the vessel to pick up the dust residue that adheres to the wall. These samples are then prepared for SEM examination.

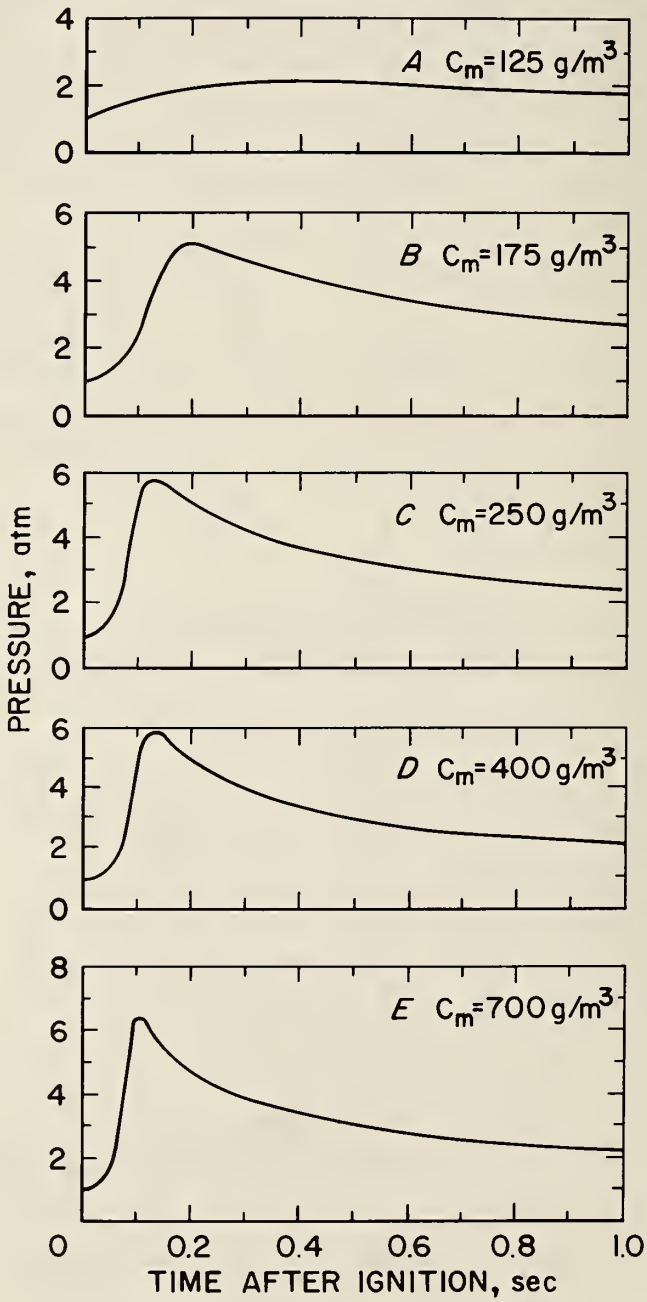

FIGURE 11. - Pressure traces for explosions of 22-μm Pittsburgh coal dust in air.

In the series of experiments using the classified Pittsburgh coal ($\bar{D}_s$ = 22 μm), the dust concentrations were varied from 125 to 700 g/m^3. The variations of temperature and peak pressure ratio as a function of concentration are shown in figure 10, and the pressure-time traces of these experiments appear in figure 11. The 125-g/m^3 concentration was a partial explosion, with a recorded pressure ratio of 1.9. Because of the small amount of dust used, very little of it was left behind to be collected, and the double-adhesive-tape procedure was used to sample the residues. SEM micrographs obtained at different magnifications from dusts before and after the explosion are shown in figure 12. Figures 12*A*-12*C* are the unburned or before-explosion dusts at three magnifications; figures 12*D*-12*F* are the residue particles from the test at 125-g/m^3 concentration. (The mass concentration of dust is denoted by C_m in the figure.) Notice the following features of figure 12:

1. After the explosion, the particles are noticeably larger than before the explosion. They exhibit rounded and smoothed surfaces in contrast to the angular and sharp edges of the particles before the explosion.

2. The particles having undergone explosions also have blowholes, and some have formed cenospheres (29).

3. Some of the particles after explosion, e.g., those in the upper middle section of figure 12*D*, are practically the same as those before the explosion. Thus a small number of particles are almost untouched by the explosion. It has been known that in explosions with low pressure ratios, the explosion fireball propagates preferentially upward and along certain directions in which the local dust concentration is higher than the average dust concentration. Particles in other directions will thus be untouched.

Those particles that are involved in the explosion are subject to rapid heating. Absorption of energy by the particles causes softening, resulting in a plastic state. Surface tension begins to smooth the edges and to produce the minimum surface energy configuration, which is a sphere. If two such particles should come into contact, these surface tensional forces cause them to adhere. Continued rapid heating subsequently leads to outgassing of volatiles, which are then burned, contributing to the explosion through rapid release of energy. This outgassing causes the deformed coal particle to swell and balloon and eventually leads to the formation of blowholes of various sizes. A variety of devolatilization models for bituminous coals have been proposed (38).

For higher dust concentrations, the resulting explosions produce progressively higher pressure ratios. The flame temperatures first increase rapidly as the concentration increases above the lean limit but then level off at the higher concentrations. Data were also obtained for the same 22-μm Pittsburgh coal dust from explosion tests at the higher concentrations of 175, 250, 400, and 700 g/m^3. Typical SEM micrographs of dust residues from these explosions are displayed in figures 13, 14, and 15. As the dust concentration increases, the fraction of dust involved in the explosion increases. As shown in figures 13*A*-13*C*, none of the dust residue particles from the test at 175 g/m^3 has any resemblance to the original dust. The same is true for the 250-, 400-, and 700-g/m^3 concentrations. The degree of agglomeration increases with concentration. At the highest dust concentration explosion, huge lumpy materials were collected, as shown in figure 15*D*, which is an optical microscope image at low magnification. These agglomerated masses bore no resemblance to the original dusts. At these higher concentrations, near the peak of the explosion pressure when all the particles are rapidly heated and becoming plastic, the probability for collision between particles is high, and the collisions result in large agglomerates.

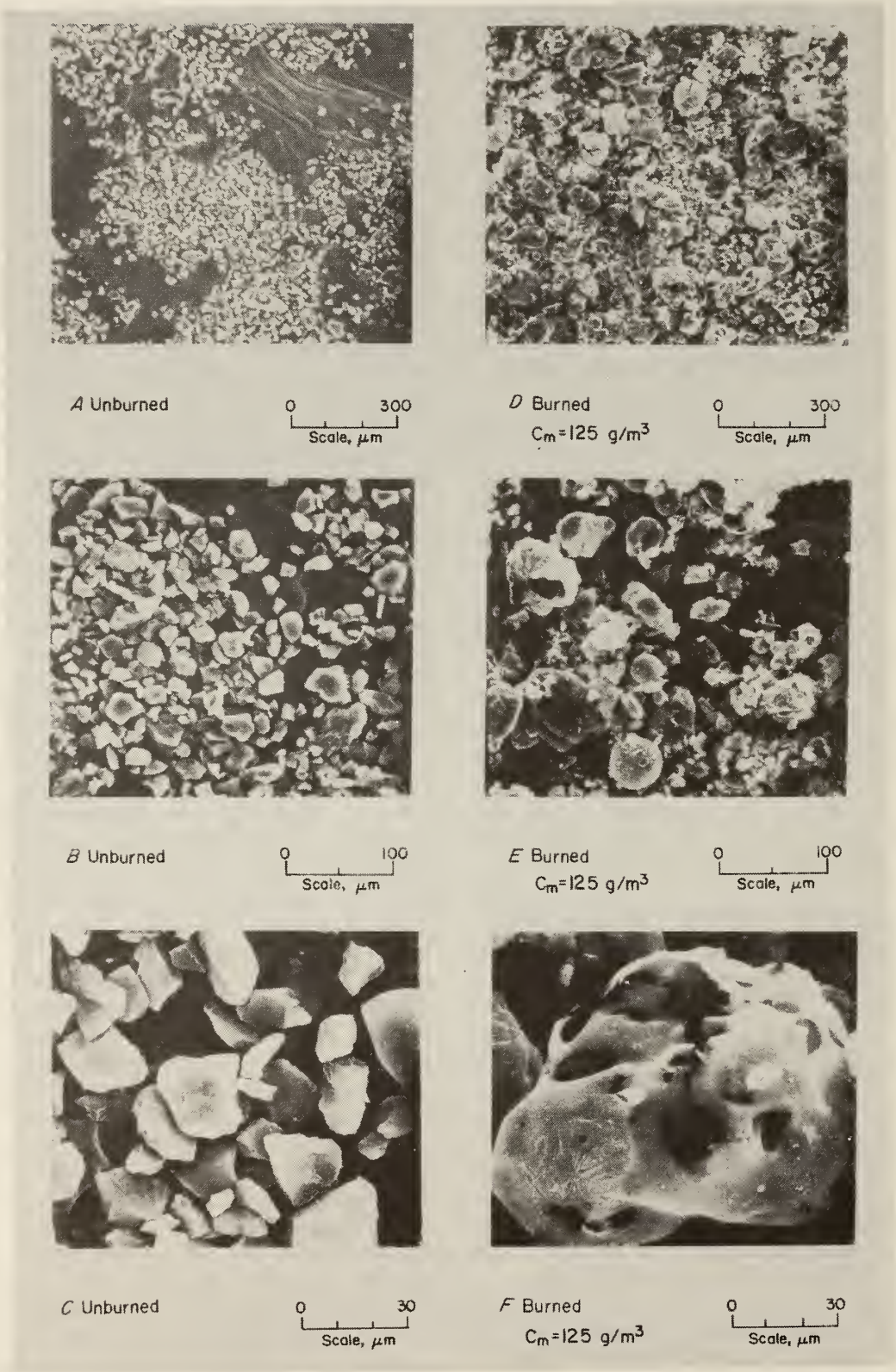

FIGURE 12. - Pittsburgh coal dust (22-μm), unburned and a low concentration burned in air.

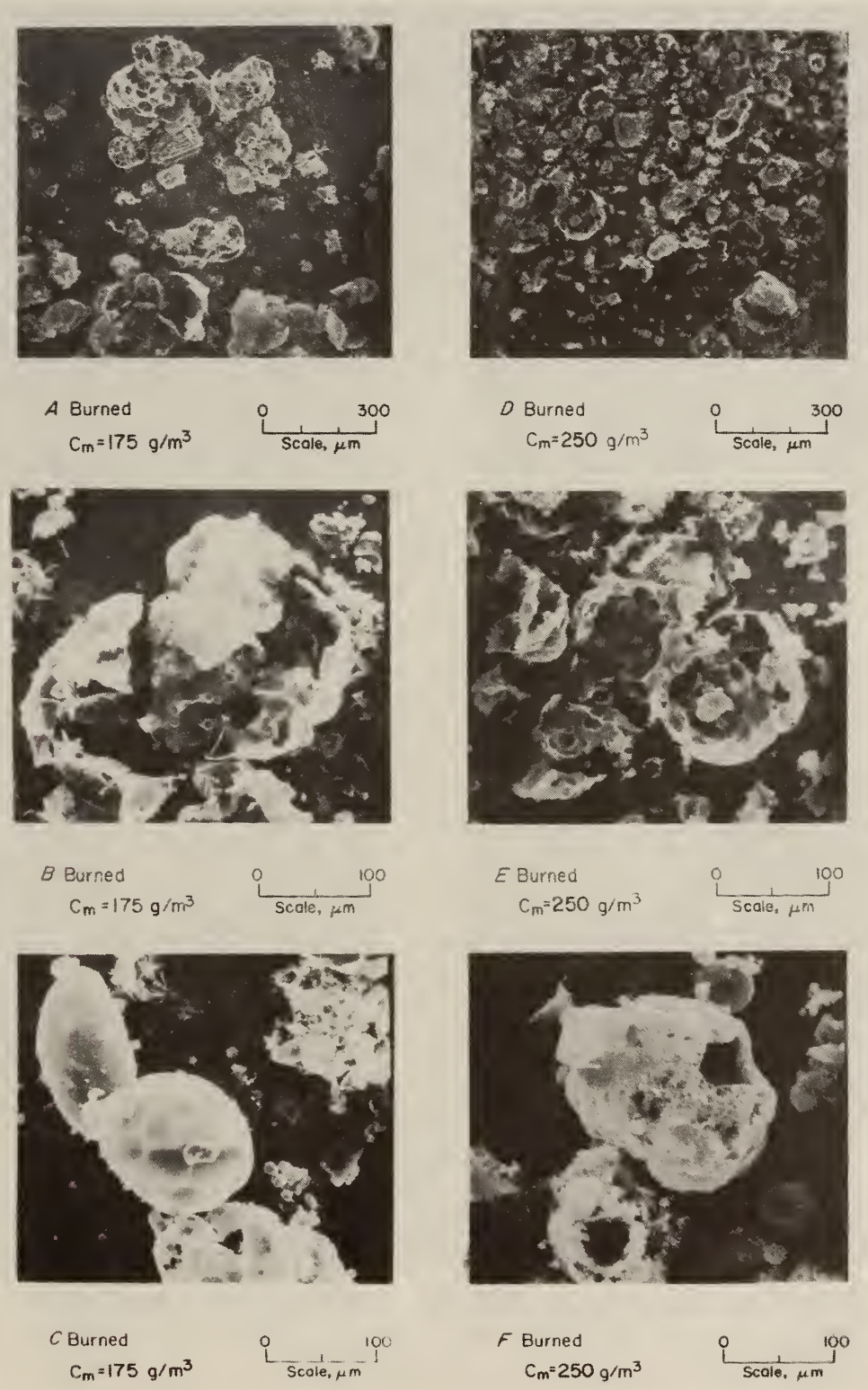

FIGURE 13. - Pittsburgh coal dust (22-μm), intermediate concentrations burned in air.

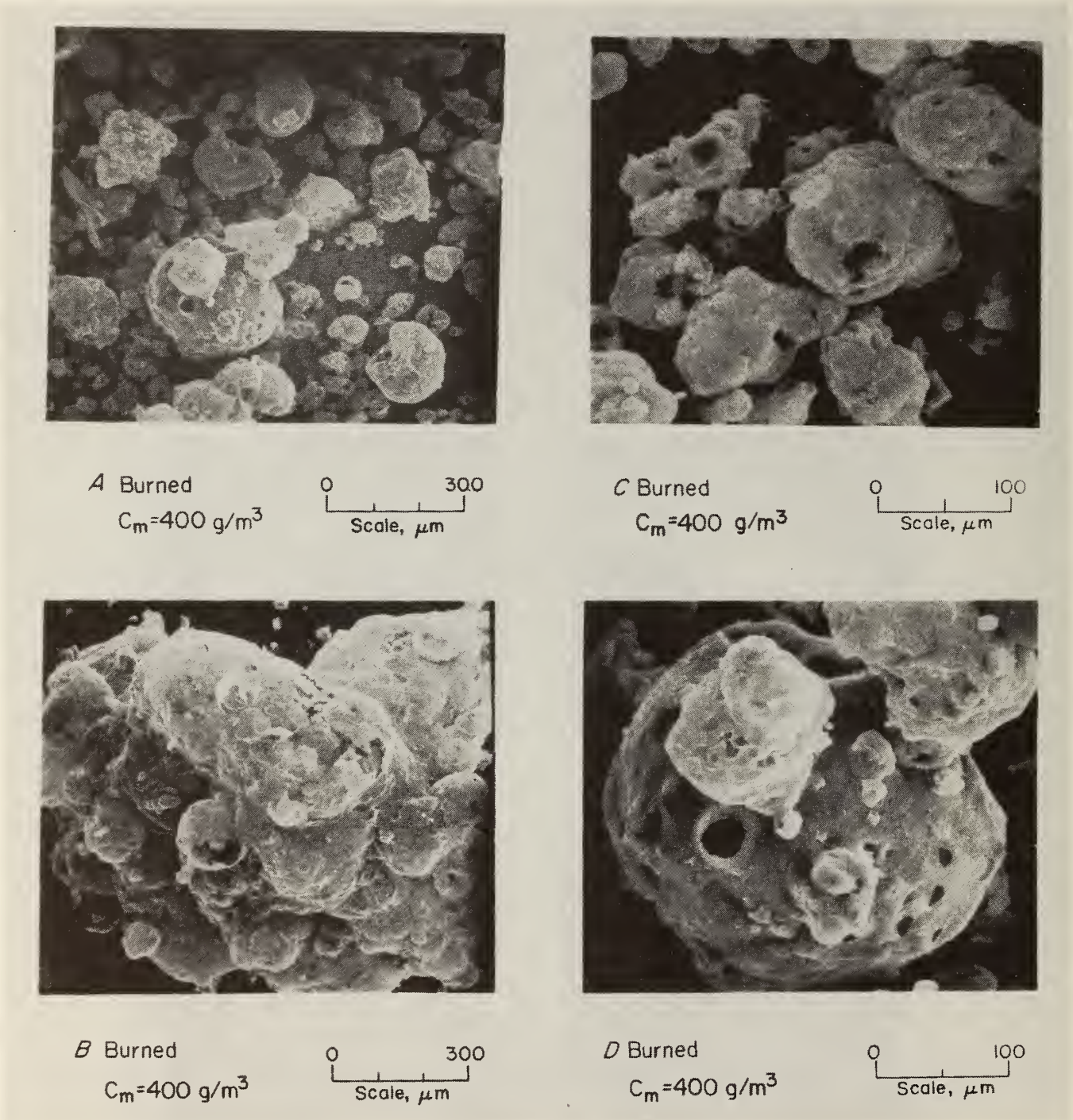

FIGURE 14. - Pittsburgh coal dust (22-μm), high concentration burned in air.

FIGURE 15. - Pittsburgh coal dust (22-μm), burned in air. (*D*, optical microscope photograph.)

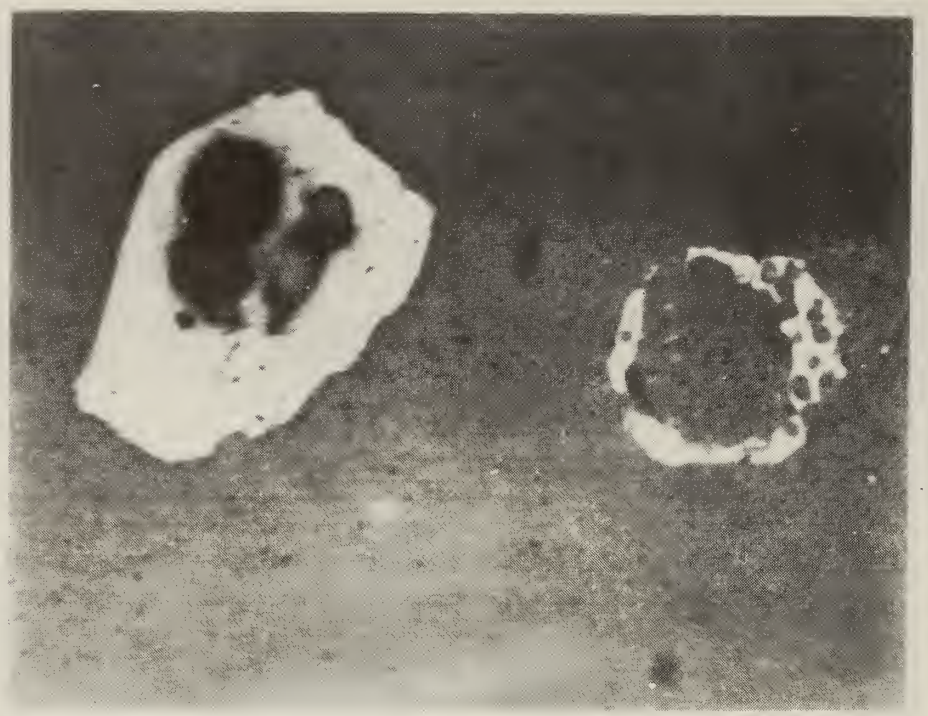

A Burned in air
C_m=400 g/m^3

0 20
Scale, μm

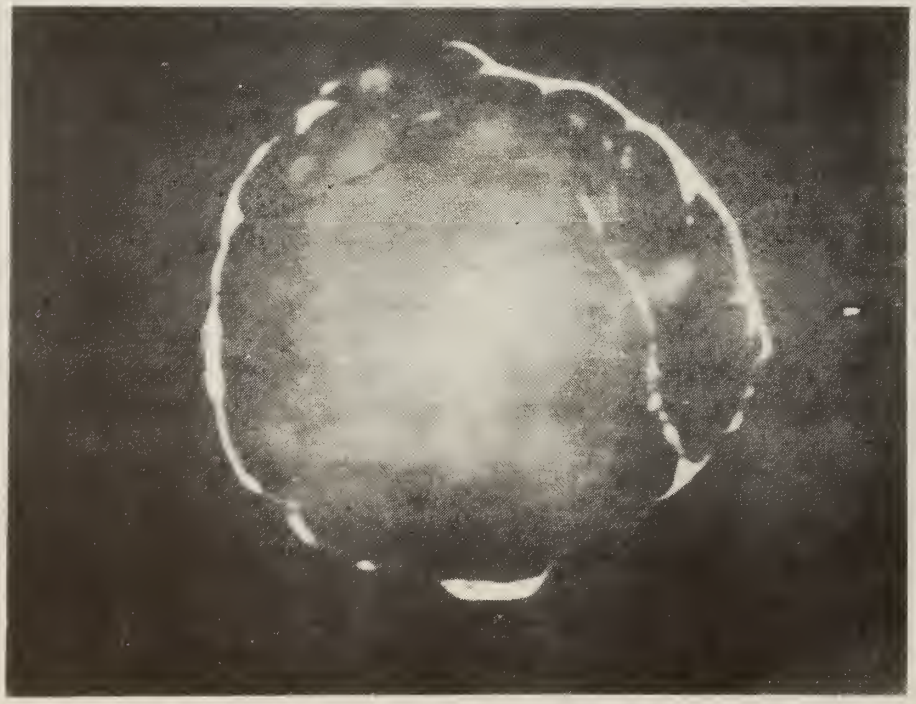

B Burned in air
C_m=400 g/m^3

0 50
Scale, μm

FIGURE 16. - Optical micrograph of sectioned Pittsburgh coal dust (35).

Occasionally, at the higher magnification micrographs (see figure 13*F*, lower right corner), one can notice some particles that are almost perfect spheres with sizes varying from 1 to 20 μm in diameter. These particles were not derived from the coal dusts but came from the electric match ignition source. When the matches are set off, their component metal compounds such as lead and cerium are vaporized and then recondensed. The almost perfect spherical shapes are produced by the condensing metals. These spherical droplets were identified as metals by their characteristic X-rays in a separate experiment in which only electric matches were set off in the 8-L chamber. The particles collected after that experiment showed the same shape as the type of particle shown in the lower right corner of figure 13*F* and gave similar X-ray spectra.

Dust residue samples from the explosions shown in figures 12-15 were also sent to P. J. Street of the Central Electricity Generating Board Marchwood Engineering Laboratories in England. His optical microscopy observations (35) of sectioned explosion residues are briefly reported here with his kind permission.

The dust samples were vacuum-dried at 105° C. Then, a few milligrams were mounted in epoxy resin, cross-sectioned, and polished before being examined under an optical microscope using reflected light. At the lower dust concentrations, many of the residue particles were unchanged; others were thick-walled hollow spheres or C-shaped partial spheres.

At the higher concentrations, almost all of the residue particles were changed from their original shapes. Figure 16 shows sectioned particles from the residue of the 400-g/m^3 coal dust explosion and can be compared to the SEM micrographs in figure 14. One particle in figure 16*A* is a thick walled cenosphere; the other particle shows internal bubbles, probably formed by the rapid generation of volatiles that had not yet vented. The particle in figure 16*B* is a thin-walled "balloon" or cenosphere. Street also observed "agglomerated balloons" up to 500 μm in size with "networks of partitions," which probably correspond to the walls of the original particles before they agglomerate as in figure 14*B*; the sectioning by Street shows the internal structure, while figure 14*B* shows only the external structure.

Pittsburgh Coal Dust (22-μm) in 50% O_2

A similar series of 8-L explosion experiments using the same 22-μm Pittsburgh coal dust was performed in an atmosphere consisting of 50% O_2 and 50% N. The variations of particle temperature (from 6λ pyrometer data) and peak pressure ratio as a function of dust concentration are shown in figure 17. The measured lean limit in 50% O_2 was about 90 g/m^3. The explosion pressure ratios and particle temperatures are higher at all concentrations than for explosions of the same dust in air. The pressure-time traces of three of these explosions are shown in figure 18. Except for the test with 350-g/m^3 dust concentration, not enough dust residue remained in the bottom of the chamber to be collected by a spatula. However, using the double-adhesive-tape sampling method, dust samples from the lower concentrations were obtained for SEM observation. Figure 19 shows the dust residue particles from a 100-g/m^3 dust explosion compared to the original dust particles at three magnifications. The dust particles show signs of having

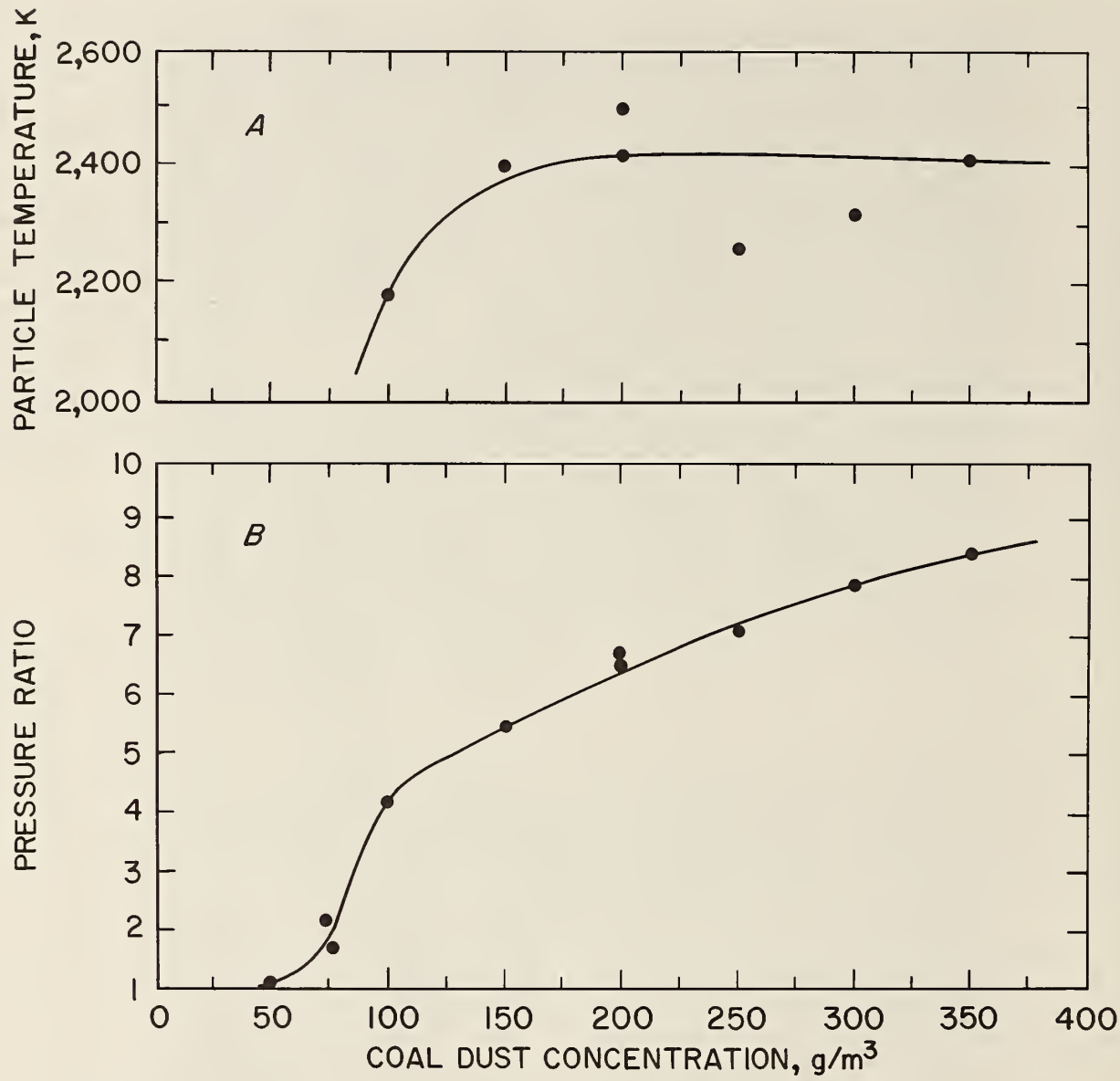

FIGURE 17. - Flammability data from the 8-L chamber for 22-μm Pittsburgh coal dust in 50% O_2.

gone through an explosion since they have blowholes and smoothed edges or corners, but the original shape of the coal particles is sometimes still discernible. Figure 20 shows the SEM micrographs of 250- and 350-g/m^3 dust explosions. It is obvious that all the particles shown have gone through explosions, with extensive blowholes, cenospheres, and heavy agglomeration. These explosions in 50% O_2 produced higher explosion pressure ratios, higher temperatures, and more rapid reactions. The formation of a plastic state followed by devolatilization and outgassing must occur at a faster rate than in air. The highest concentration

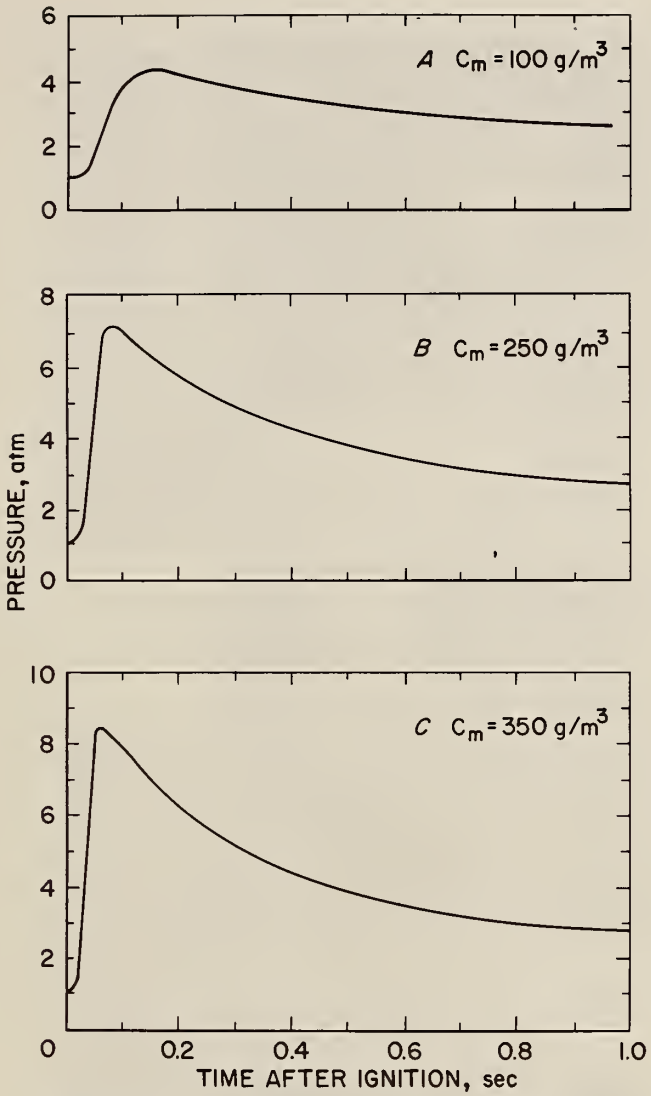

FIGURE 18. - Pressure traces for explosions of 22-μm Pittsburgh coal dust in 50% O_2.

studied, 350 g/m^3, is still a lean mixture in 50% O_2; hence the pressure ratio was still increasing (fig. 17*B*) at that concentration.

Pittsburgh Coal Dust (2-μm) in Air

Figure 21 shows the variation of explosion pressure with dust concentration for the 2-μm Pittsburgh coal dust ($\bar{D}_s$ = 2.2 μm in figure 9). Note that these data are very similar to those in figure 10*C* for the 22-μm dust. This is a very small-sized dust, as shown in the Coulter size distribution in figure 9 and the SEM micrographs of the unburned dust in figure 22. This dust is clearly much smaller than that used in the previously described experiments. SEM micrographs of this finer dust after a 200-g/m^3 explosion are shown in figure 23. A noticeable feature is that all the dust residues are considerably larger than the unburned dust. Blowholes and cenospheres abound. In many cases, the original particles have agglomerated to huge masses with diameters of the order of 100 μm. Since these large spheres show no trace of the original particles, they must have been formed while the particles were still plastic.

Pittsburgh Coal Dust (84-μm) in Air

A few tests were performed with Pittsburgh coal dust of much larger size, $\bar{D}_s$ = 84 μm in figure 9. The pressures and temperatures are plotted as a function of concentration in figure 24. Note that the lean flammable limit for this dust in air is 210 g/m^3, considerably higher than for the two smaller sizes of Pittsburgh coal. Also, the maximum explosion pressures and maximum particle temperatures are lower than those of the smaller dusts. SEM micrographs of the unburned and burned dust particles are shown in figure 25. The characteristic angular features of the unburned dust are clearly visible (figs. 25*A*-25*C*). Micrographs of the dust residues after a 300-g/m^3 explosion (figs. 25*D*-25*F*) showed that practically every particle has reacted at this concentration. The angular features are totally absent after explosion, indicating that the particles have undergone considerable heating and devolatilization. The inflated spheres are about twice the size of the unburned particles. Furthermore, agglomeration is quite evident.

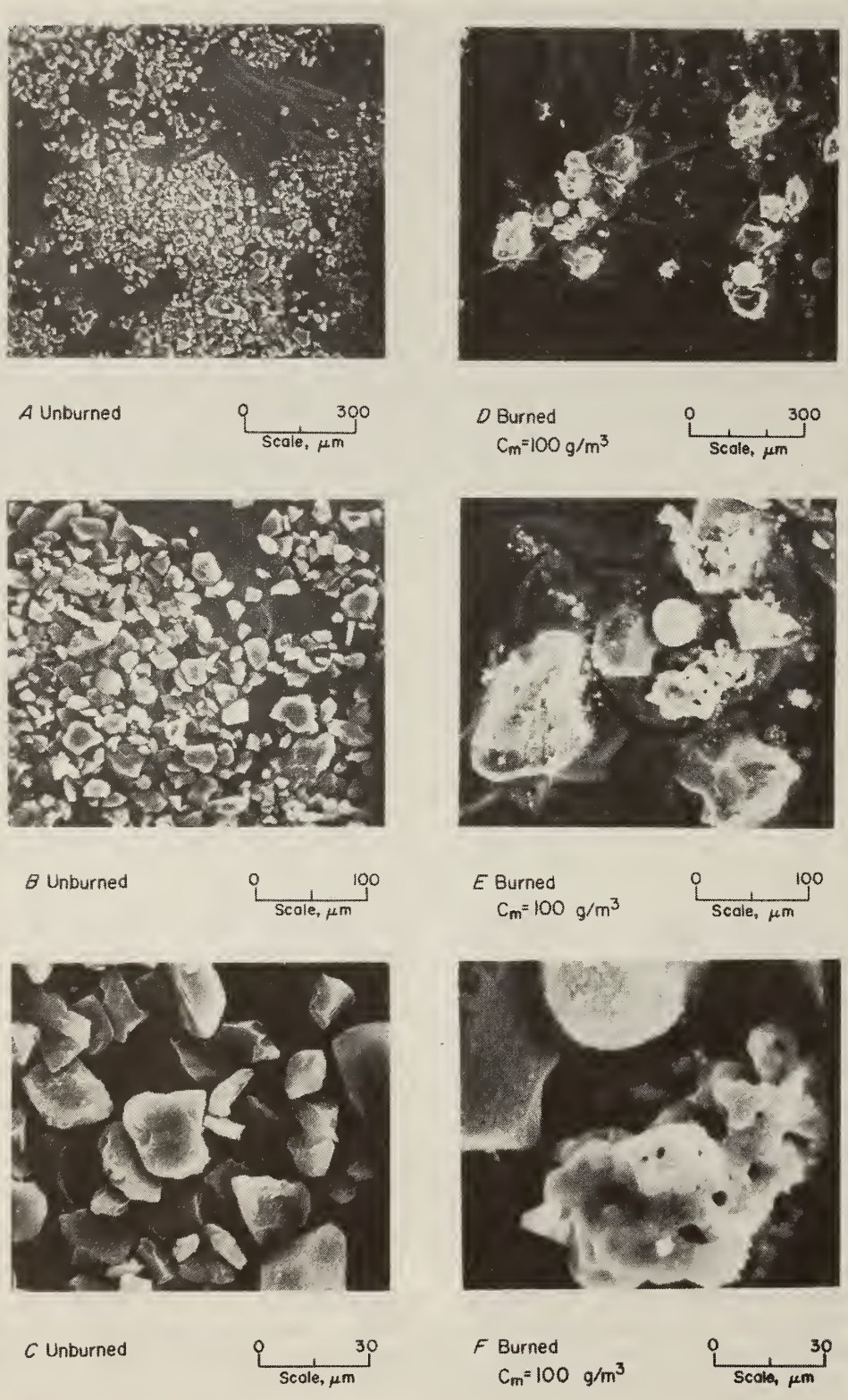

FIGURE 19. - Pittsburgh coal dust (22-μm), unburned and burned in 50% O_2.

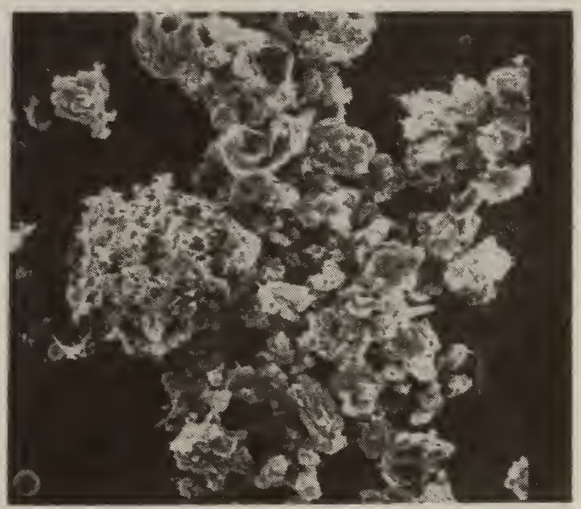

A Burned
C_m=250 g/m^3

0 300
Scale, μm

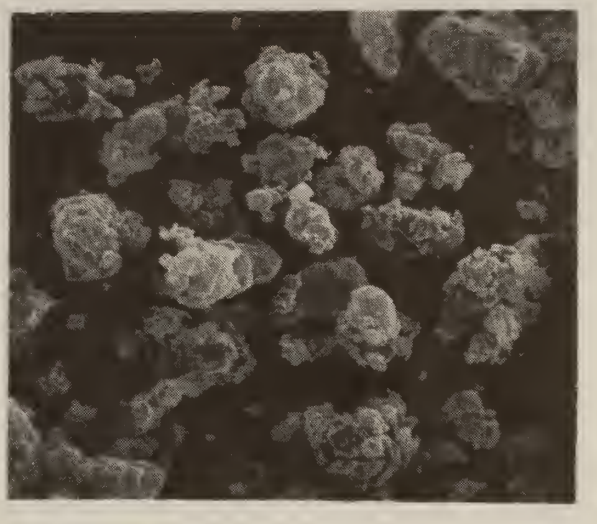

C Burned
C_m=350 g/m^3

0 300
Scale, μm

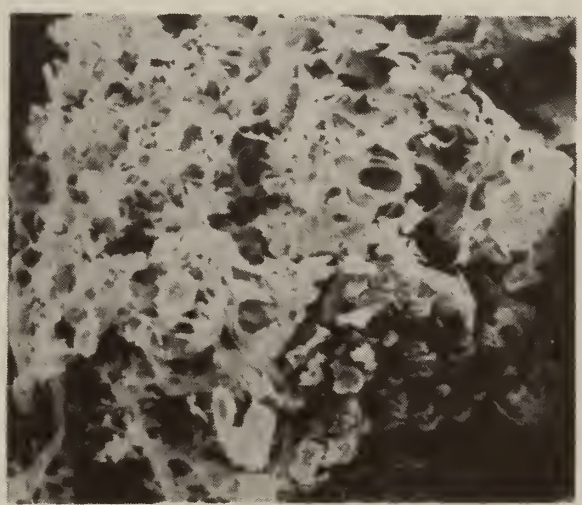

B Burned
C_m=250 g/m^3

0 100
Scale, μm

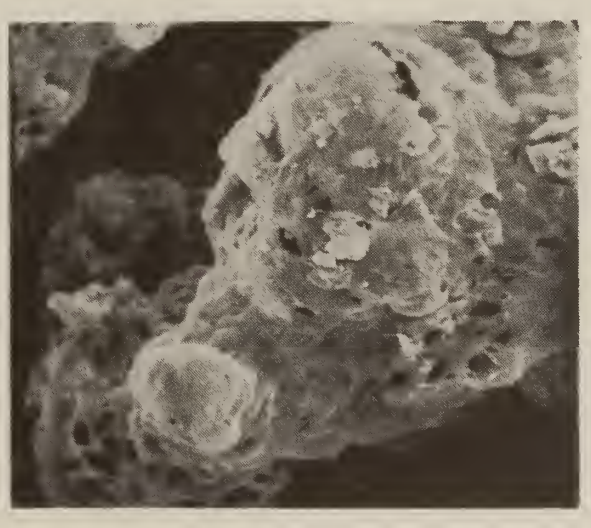

D Burned
C_m=350 g/m^3

0 100
Scale, μm

FIGURE 20. - Pittsburgh coal dust (22-μm), burned in 50% O_2.

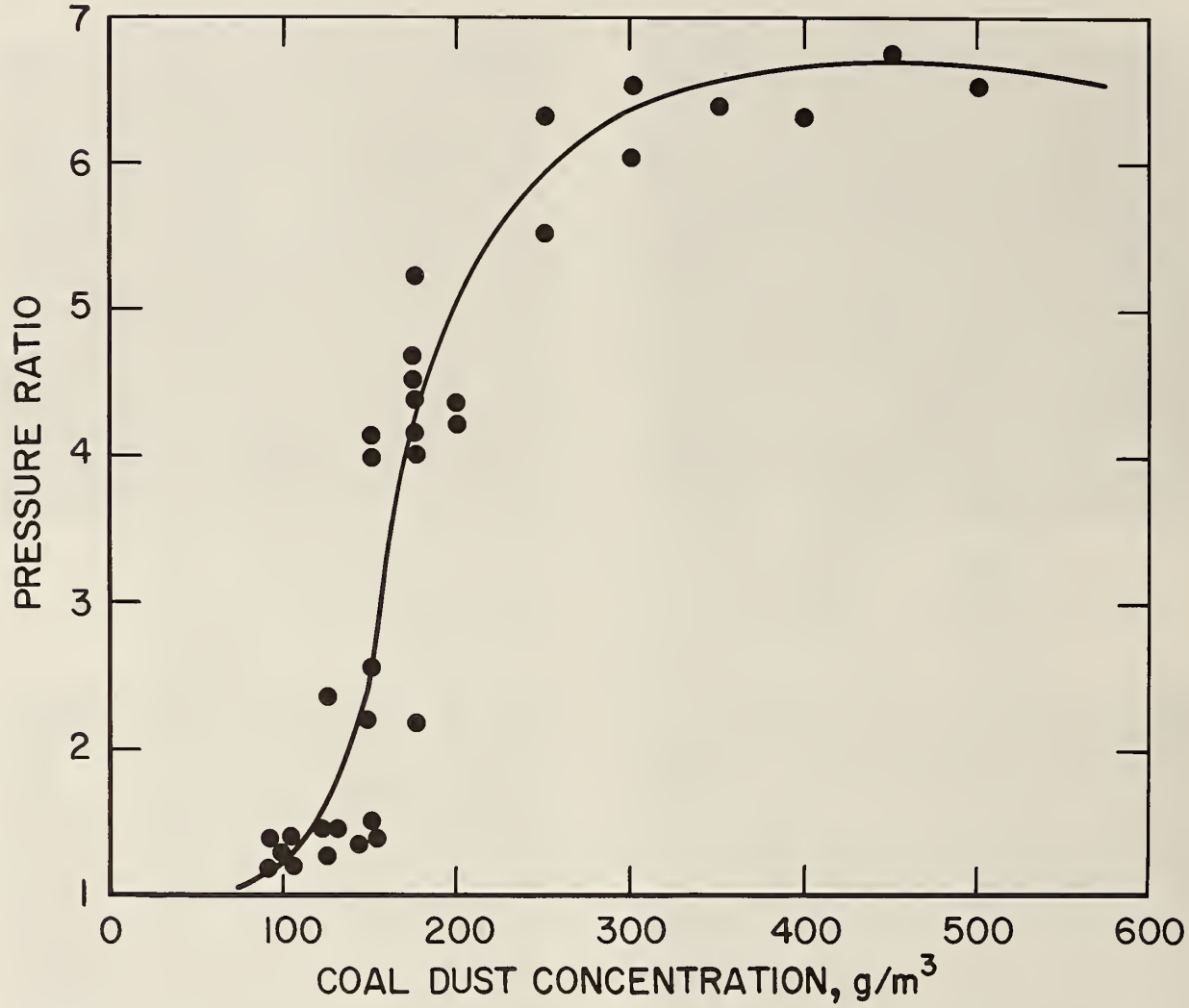

FIGURE 21. - Flammability data from the 8-L chamber for 2-μm Pittsburgh coal dust in air.

Particle Size Effects for Pittsburgh and Pocahontas Coals

Figure 26 shows the effect of particle size on the flammability of Pittsburgh (35% volatility by the ASTM D3175 test) and Pocahontas (16% volatility) coals (15). The Pittsburgh coal shows a constant lean flammable limit for particle sizes up to about 40 μm. The lean limit then rises, slowly at first and then more rapidly. Above 100 μm the dust becomes nonignitable even with a very strong ignition source (six matches). The Pocahontas coal shows a slow rise in the lean limit with increasing particle size even for the finest sizes studied. At 2 μm, it has a lean limit only slightly higher than that of Pittsburgh coal, but at 20 to 50 μm the limit is significantly higher. Above 80 μm, the Pocahontas coal becomes nonignitable. At the smaller sizes, the variation in the lean limit appears to be due to variations in the real volatility of the dusts at the high heating rates of flames compared to the standard ASTM volatility test. At the larger sizes, the lean limits for both coals increase because the particles are not able to devolatilize fast enough to feed the propagating flames (15). Consequently, a higher mass concentration of dust is necessary to provide the minimum amount of combustible volatiles at the lean limit.

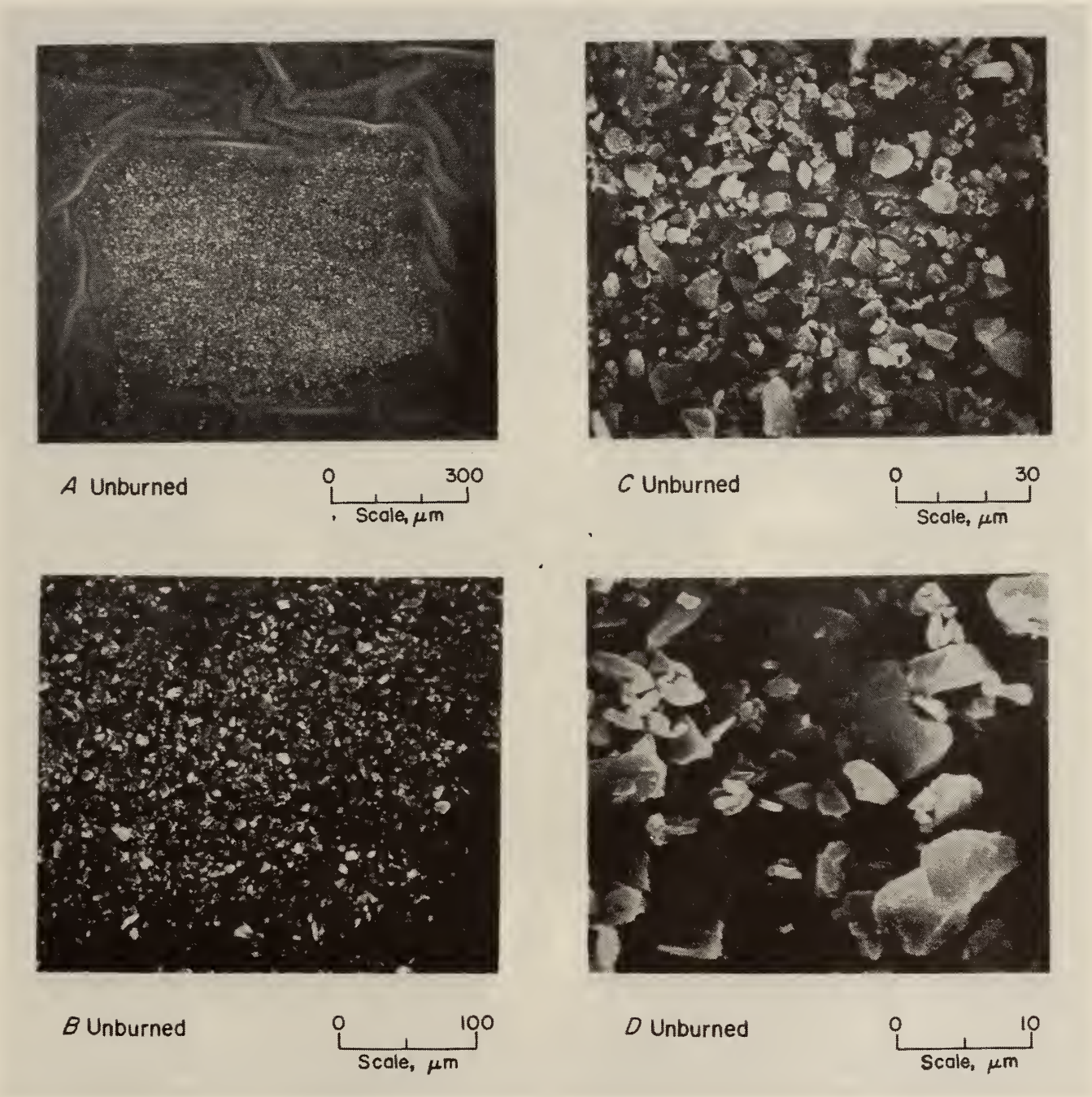

FIGURE 22. - Unburned Pittsburgh coal dust (2-μm).

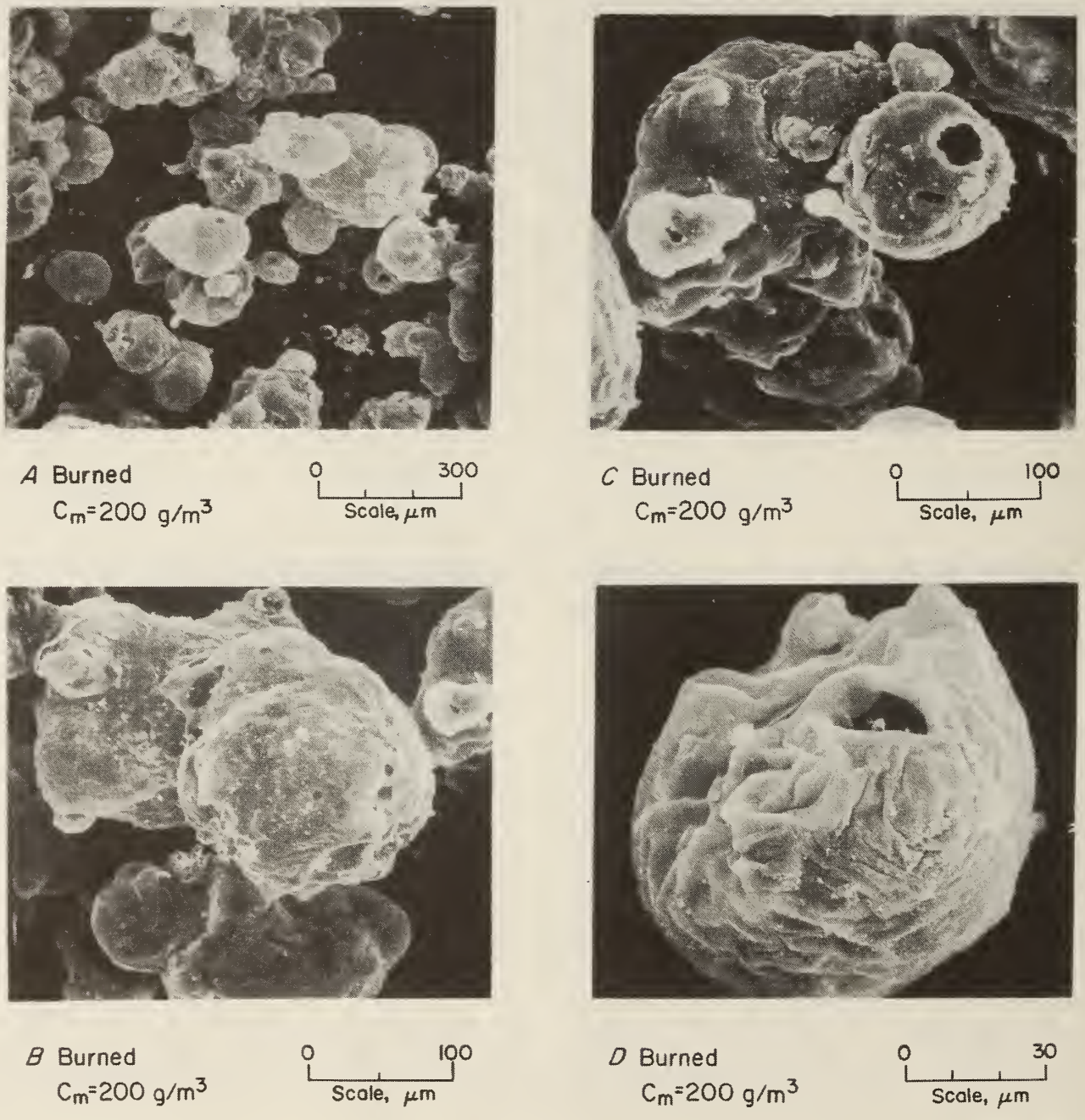

FIGURE 23. - Pittsburgh coal dust (2-μm), burned in air.

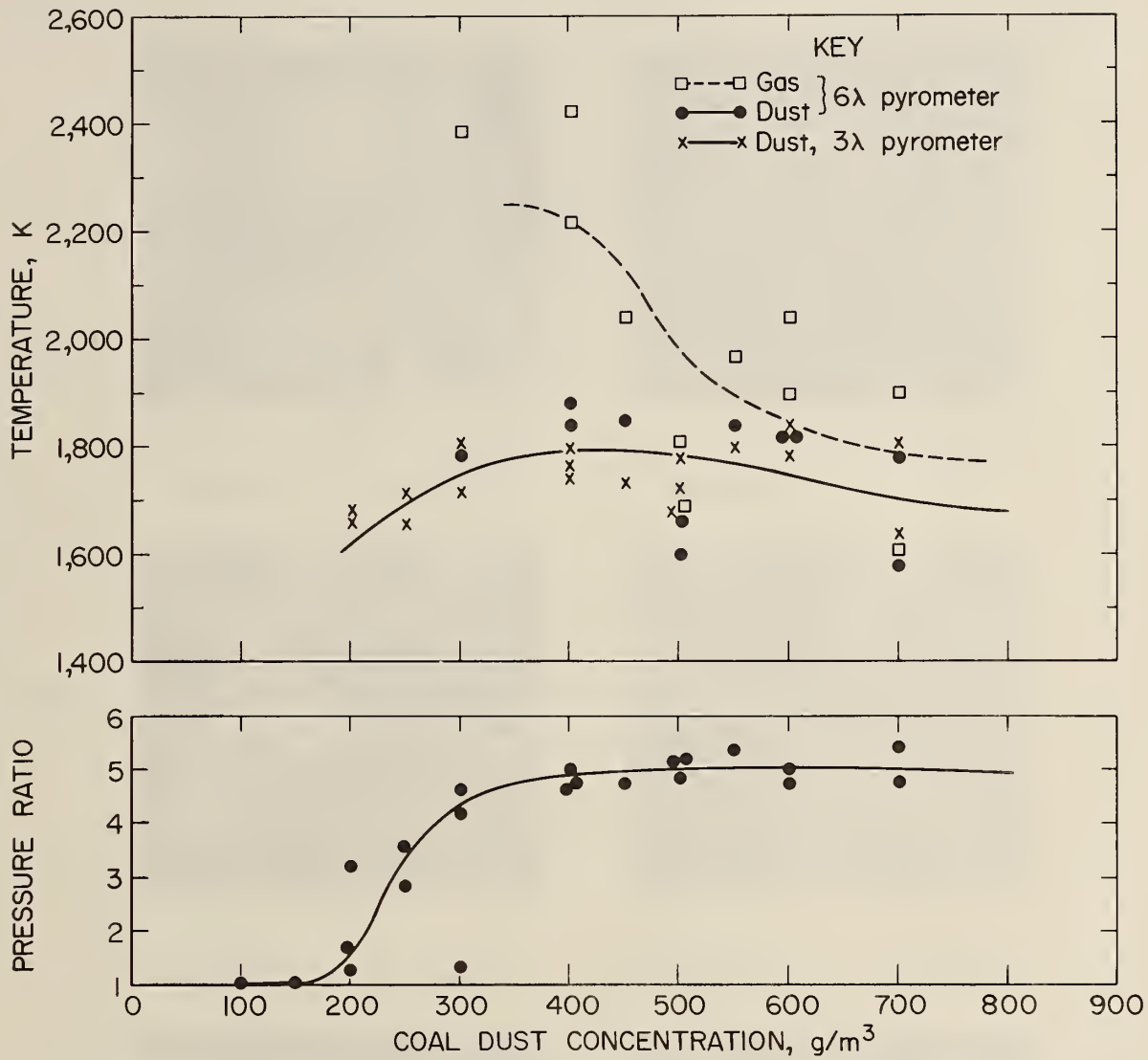

FIGURE 24. - Flammability data from the 8-L chamber for 84-μm Pittsburgh coal dust in air.

Pocahontas Coal Dust in Air

The explosion pressure variation with dust concentration for a size-classified Pocahontas seam coal is shown in figure 27. This dust has a surface mean diameter $\bar{D}_s$ = 13 μm and a mass mean diameter $\bar{D}_w$ = 17 μm. Note that the lean limit is only slightly higher than for Pittsburgh coal of similar size, but the maximum pressures are significantly lower. Micrographs of this coal before explosion are shown in figures 28*A*-28*C*. It looks very much like unburned Pittsburgh coal in that the surfaces exhibit sharp and angular features. The dust residues of Pocahontas coal after an explosion at a concentration of 450 g/m^3 are shown in figures 28*D*-28*F*. The burned particles also look much like the Pittsburgh coal dust residues after explosions at similar concentrations. There are extensive blowholes and cenospheres. Also evident in figure 28*E* is some agglomeration of coal dust due to collisions while still in the plastic state.

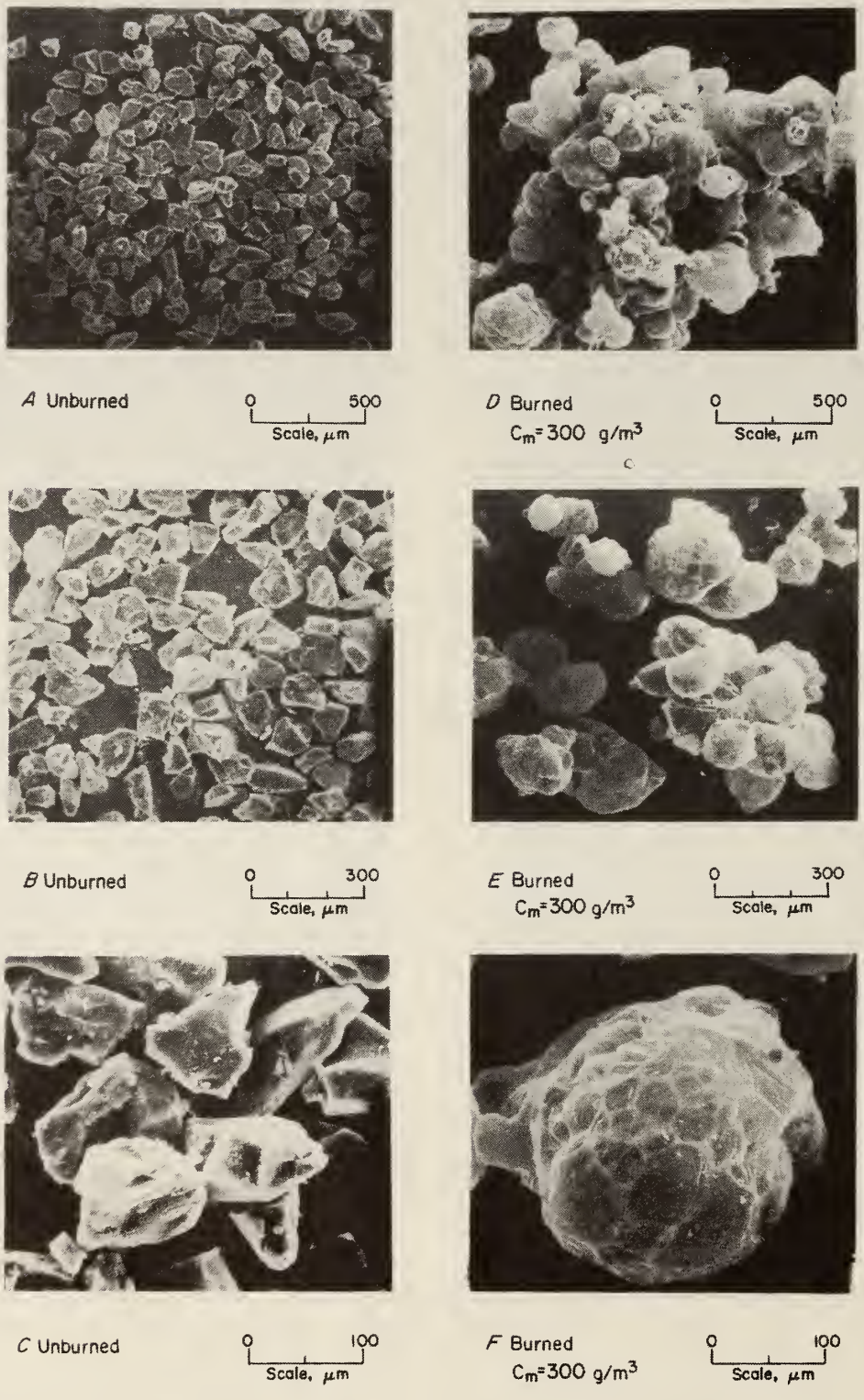

FIGURE 25. - Pittsburgh coal dust (84-μm), unburned and burned in air.

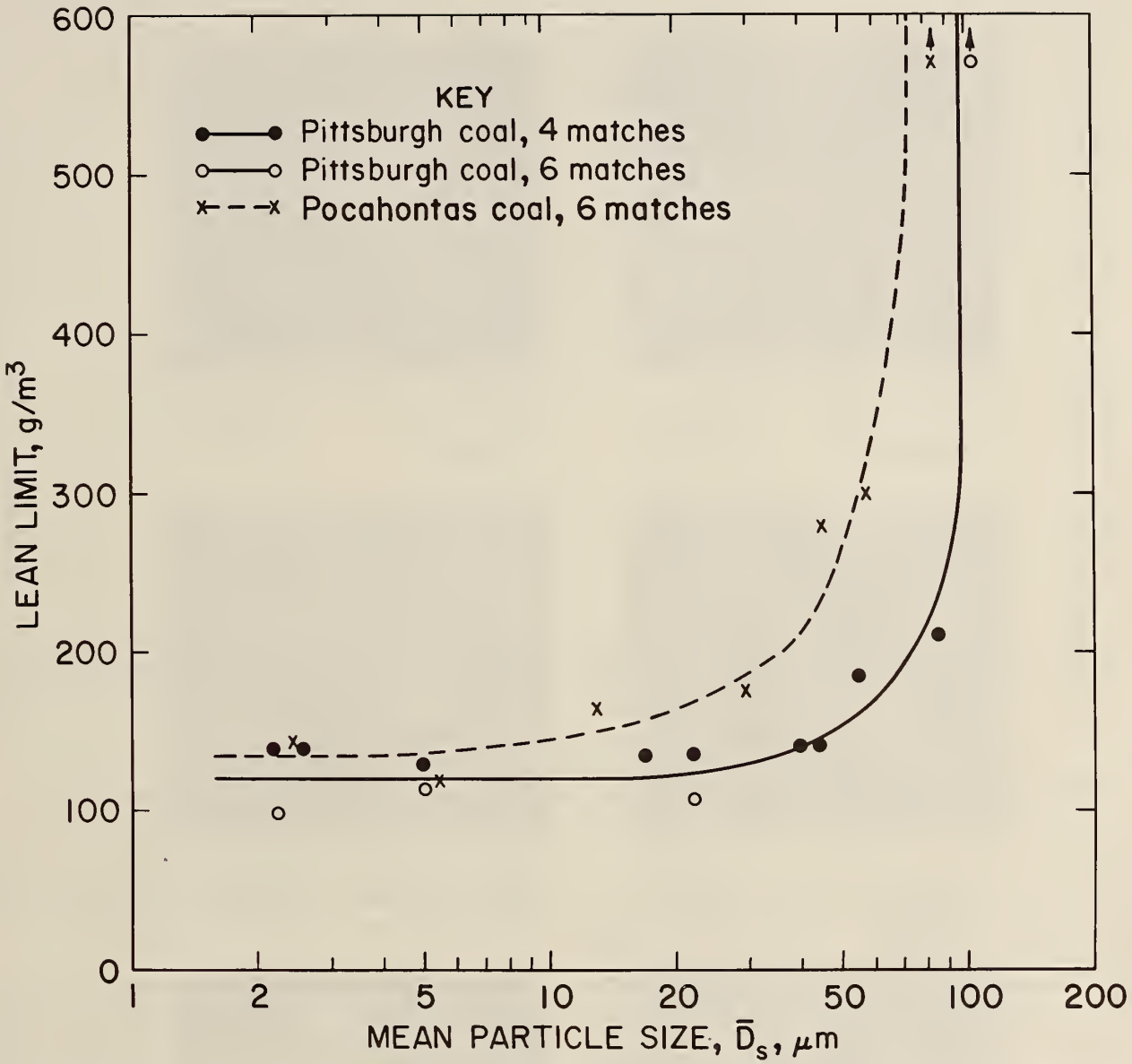

FIGURE 26. - Lean flammable limit for Pittsburgh and Pocahontas coals as a function of particle size.

Anthracite Dust in Air and in 50% O_2

Anthracite dust, which has a lower volatile content (7% by the ASTM D3175 test) than bituminous coal dusts, was also tested in the 8-L chamber. Anthracite dust is normally considered to be nonexplosive in air. However, with a strong ignition source and heavy dust loading (400 to 700 g/m^3), this very fine dust ($\bar{D}_s$ = 5 μm and $\bar{D}_w$ = 9 μm) was able to produce explosions in air (21% O_2). The pressures of these explosions are shown in figure 29, which shows both the lean and rich explosion limits of this dust in air. In a 50% O_2 atmosphere, the dust becomes explosive at a much lower concentration (150 g/m^3), and it continues to be explosive with increasing dust concentrations. SEM micrographs of dust

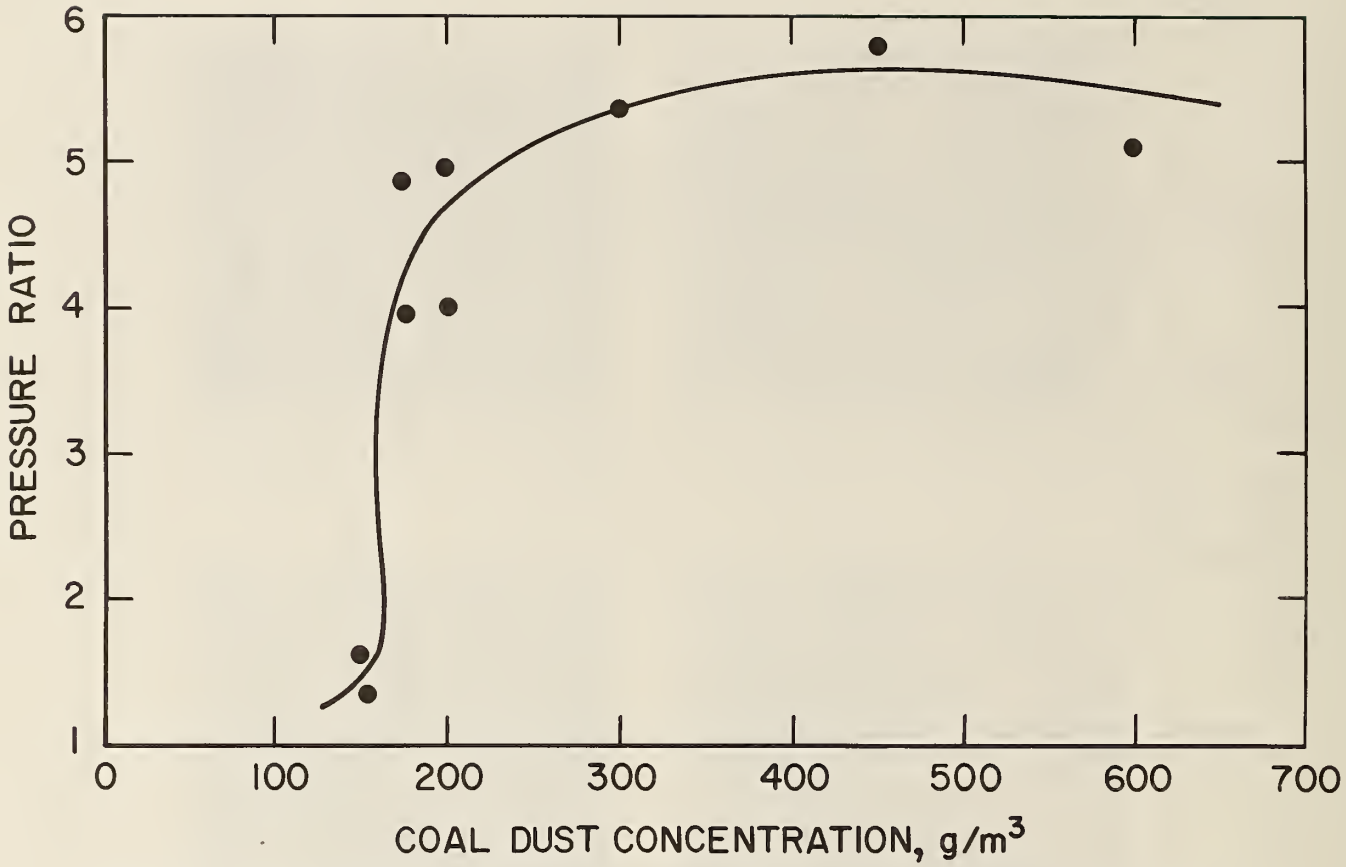

FIGURE 27. - Flammability data from the 8-L chamber for 13-μm Pocahontas coal dust in air.

residues from explosions in air and in 50% O_2 are shown in figures 30 and 31. The unburned anthracite dust shows a very broad size distribution (figs. 30*A*-30*C*). Sharp and angular features are evident. The majority of burned particles do not look much different from those before the explosion. However, some of them showed definite changes, such as the appearance of small blowholes. Because this is not a bituminous coal and does not go through a plastic phase during devolatilization, the particles do not become rounded and do not form cenospheres. The fraction of the coal particles covered by microblowholes is larger for coal particles in the 50% O_2 explosion than for that in air. The appearance of the particles in figures 31*C* and 31*F* seems to indicate layered structures.

The smallest particles that are easily visible in the unburned sample (figs. 30*A*-30*C*) are almost totally absent in the samples collected after explosions, especially for the 50% O_2 atmosphere. It is uncertain whether they were consumed by the explosion or were not sampled. However, it is unlikely that they totally escaped being sampled because the same sampling method used in other experiments successfully collected small particles.

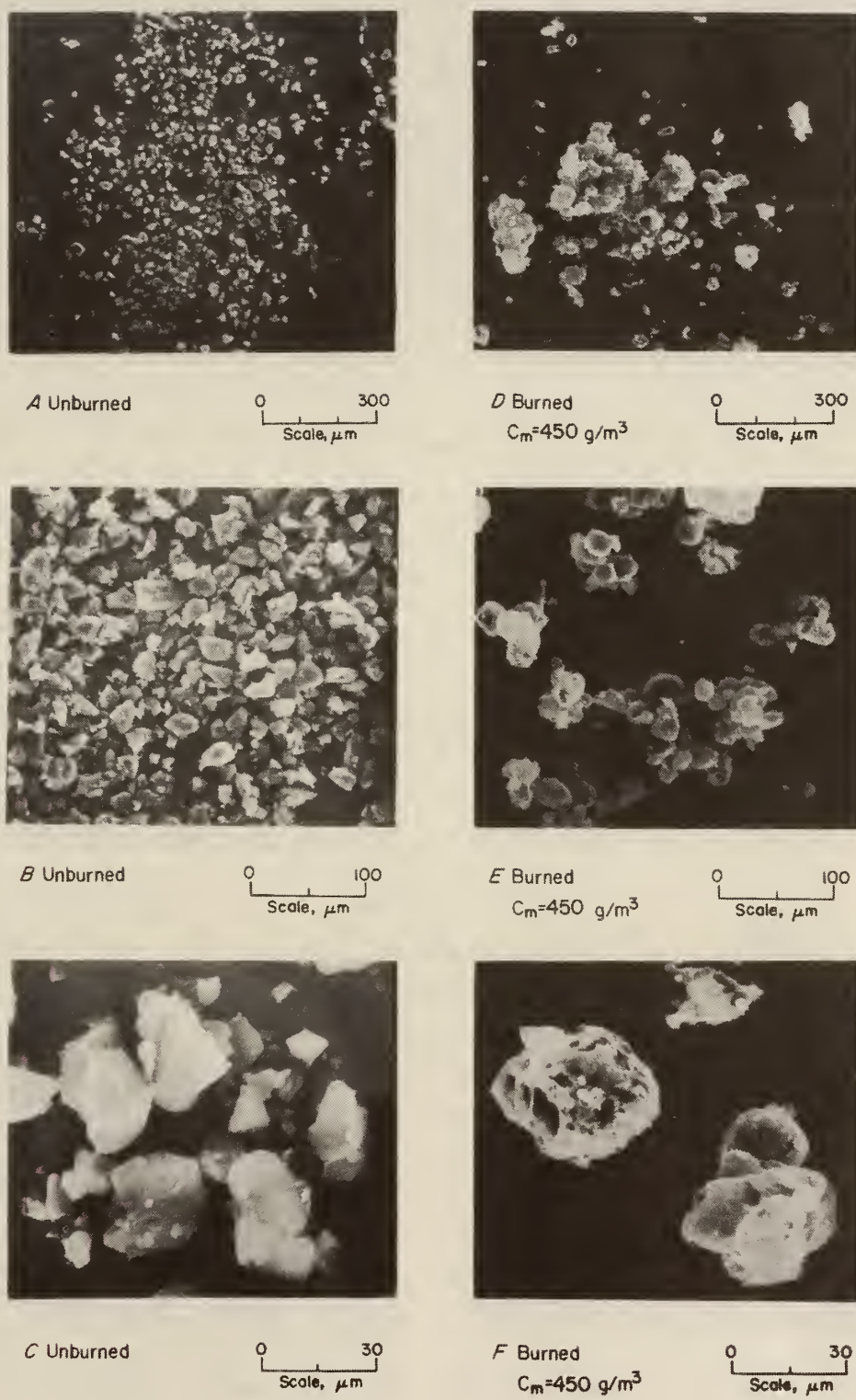

FIGURE 28. - Pocahontas coal dust (13-μm), unburned and burned in air..

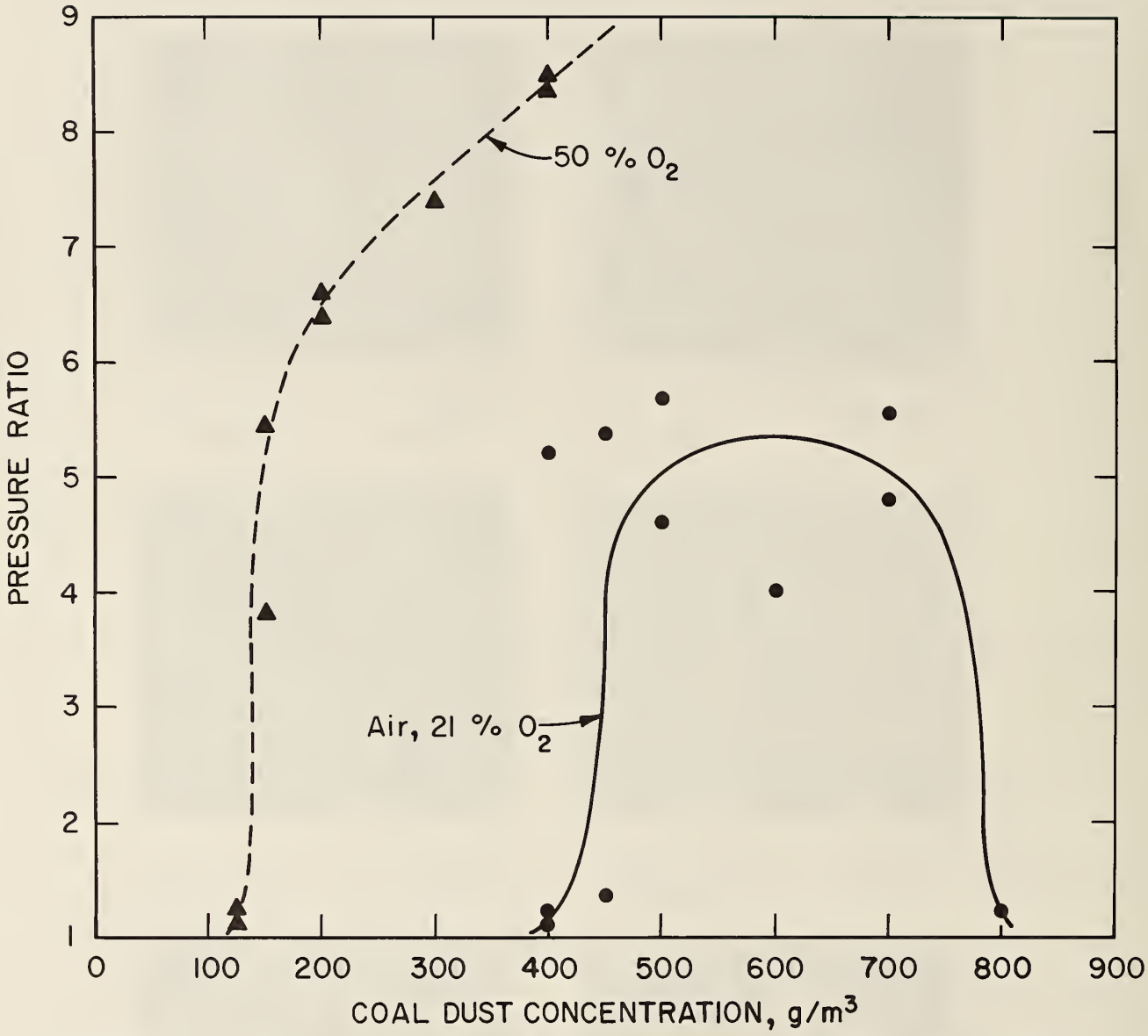

FIGURE 29. - Flammability data from the 8-L chamber for anthracite in air and in 50% O_2.

Graphite Dust in 50% O_2

To obtain combustible dusts of even lower volatile content, graphite powder and diamond dust were chosen. They have volatile contents of about 1/2% and 0%, respectively, and are allotropic forms of pure carbon. Graphite dust with $\bar{D}_s$ = 4 μm and $\bar{D}_w$ = 6 μm exploded in a 50% O_2 atmosphere. The explosion pressure variation with concentration is shown in figure 32. The micrographs of before and after explosion samples are shown in figure 33. There is not much difference in the appearance of the two samples. The graphite dust samples were amorphous graphite and, unlike the coal samples studied previously, do not exhibit sharp angular features. However, again, the small particles so visible in the unburned sample (fig. 33*A*) are less evident in the burned sample. It is quite possible that they are consumed in the explosion. No obvious blowholes or deformations of the remaining particles are evident.

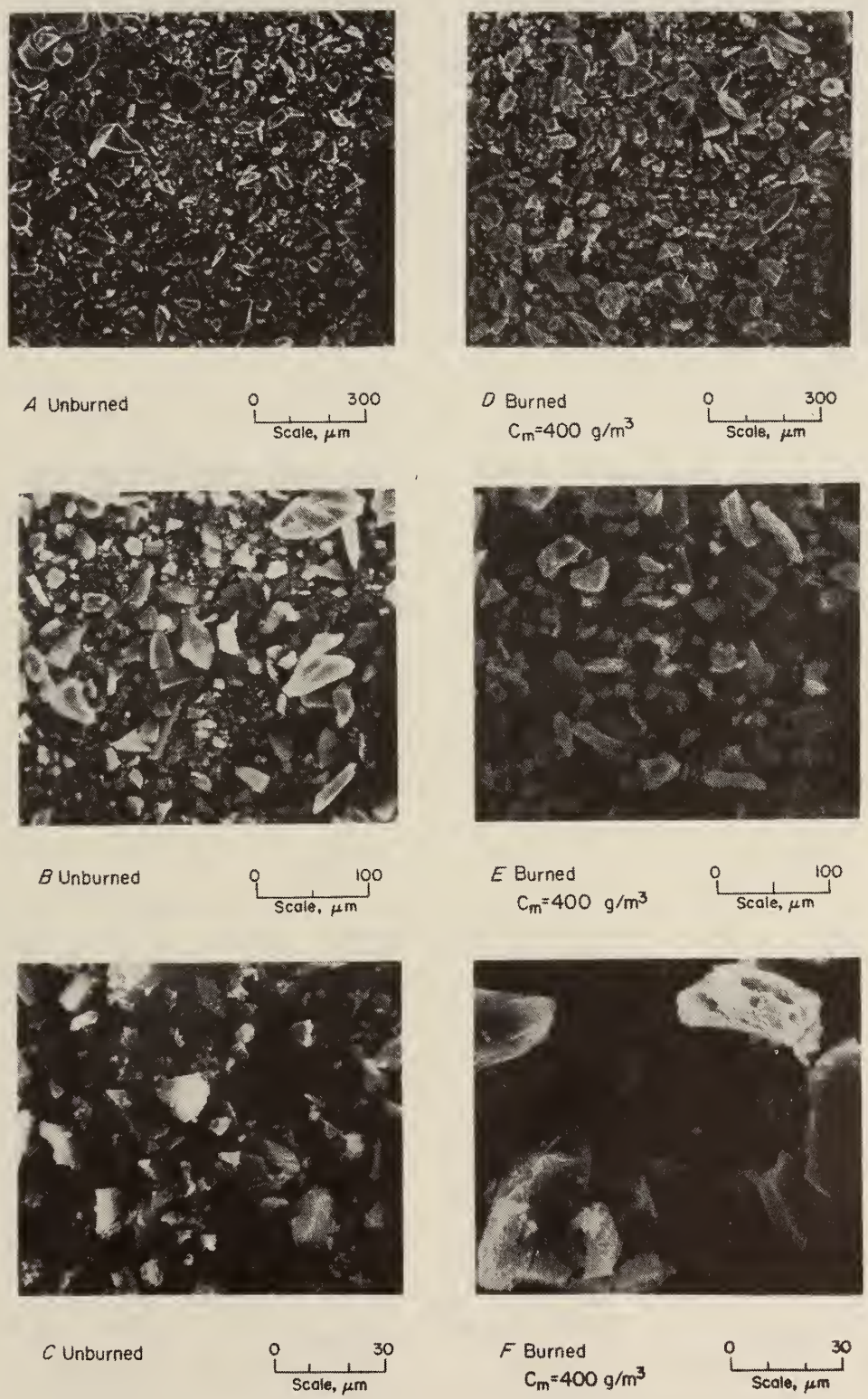

FIGURE 30. - Anthracite dust, unburned and burned in air.

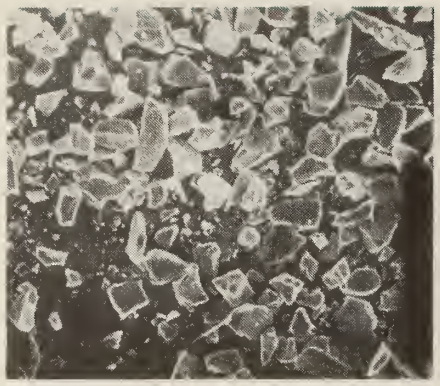

A Burned
C_m=400 g/m^3

0 300
Scale, μm

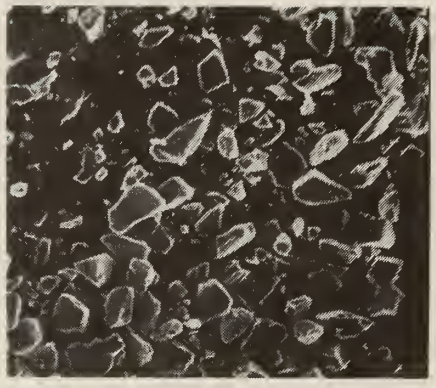

D Burned
C_m=400 g/m^3

0 300
Scale, μm

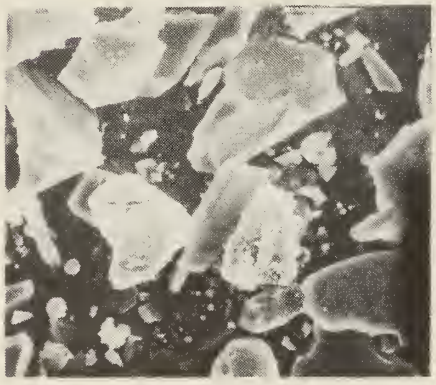

B Burned
C_m=400 g/m^3

0 100
Scale, μm

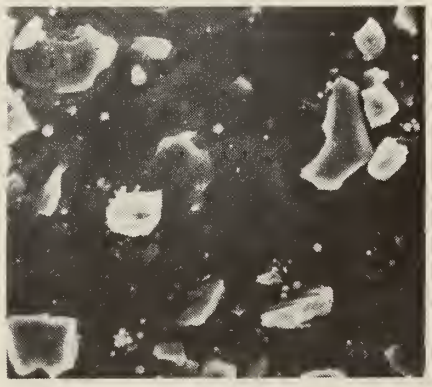

E Burned
C_m=400 g/m^3

0 100
Scale, μm

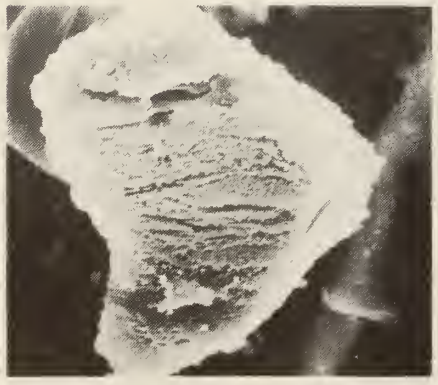

C Burned
C_m=400 g/m^3

0 30
Scale, μm

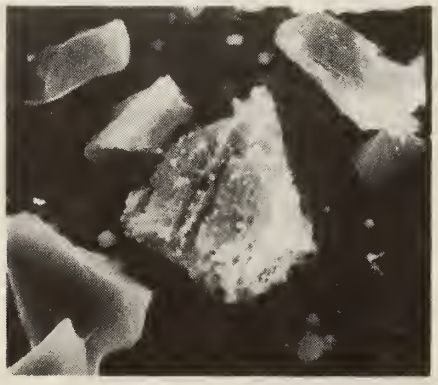

F Burned
C_m=400 g/m^3

0 30
Scale, μm

FIGURE 31. - Anthracite dust, burned in 50% O_2.

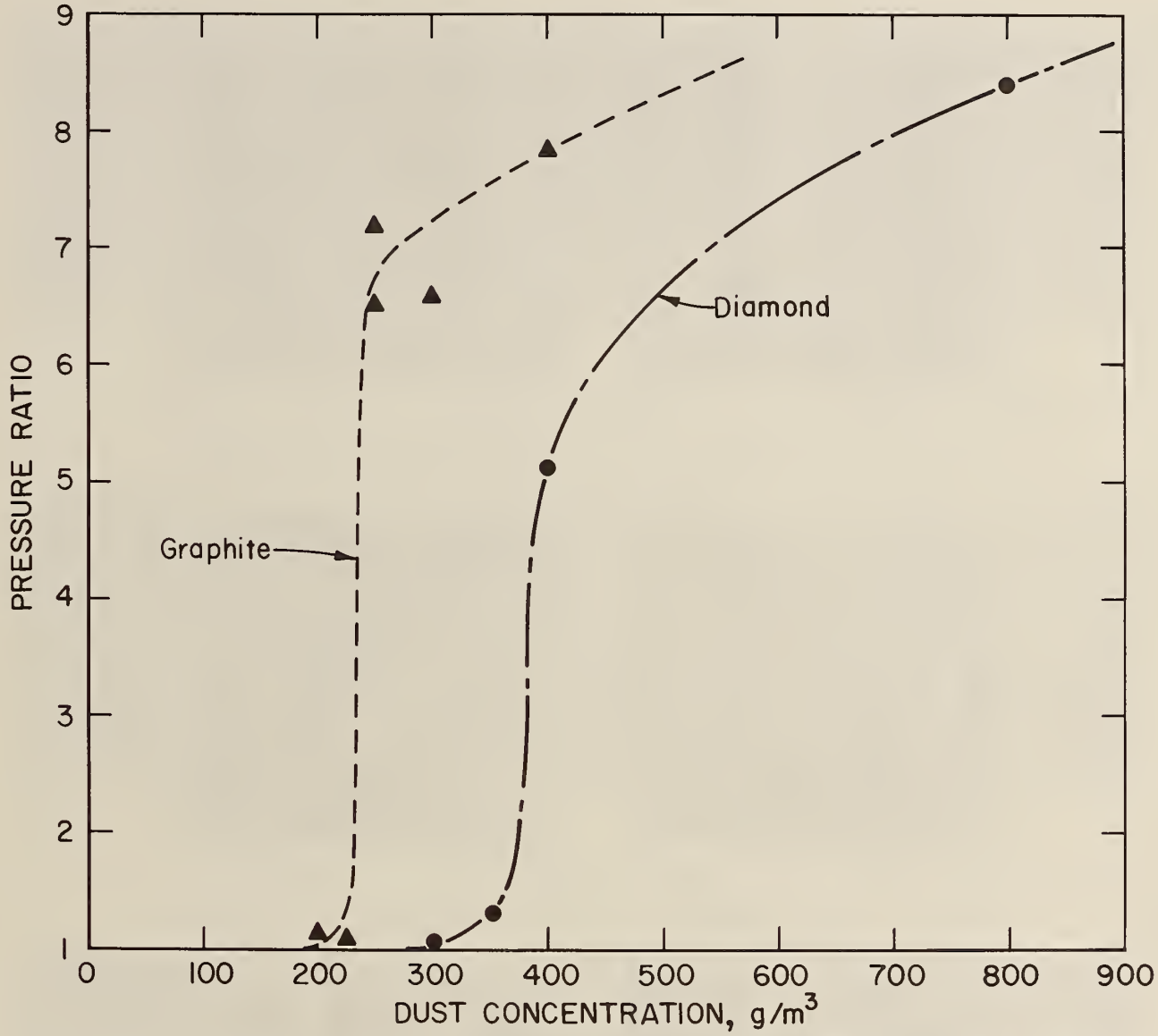

FIGURE 32. - Flammability data from the 8-L chamber for graphite and diamond dust in 50% O_2.

Diamond Dust in 50% O_2

The explosion pressures for synthetic diamond dust ($\bar{D}_s$ = 2.3 μm and $\bar{D}_w$ = 2.6 μm) are shown in figure 32. A rather large explosion (pressure ratio = 8) was produced at a dust concentration of 800 g/m^3 in 50% O_2, using a strong ignition source of six matches. The dusts before and after explosion have the same angular appearance (fig. 34). There are some smooth, spherical particles in the after-explosion samples (especially in figure 34*E*), but these are not diamond particles. Elemental distribution maps of the burned particles in figures 34*D*-34*F* were made using lead and cerium X-rays, and these are shown in figures 34*G*-34*I*. Comparing these maps with their respective micrographs shows that those particles having smooth surfaces were actually remnants from the electrical matches used to initiate the explosions. The X-ray spectrum of these match particles as well as that of the diamond particles is shown in figure 35. The strong M-lines of lead near 2.4 KeV and the L-lines of cerium near 5 keV were used to generate the X-ray maps in figures 34*G*-34*I*. The combustion of graphite

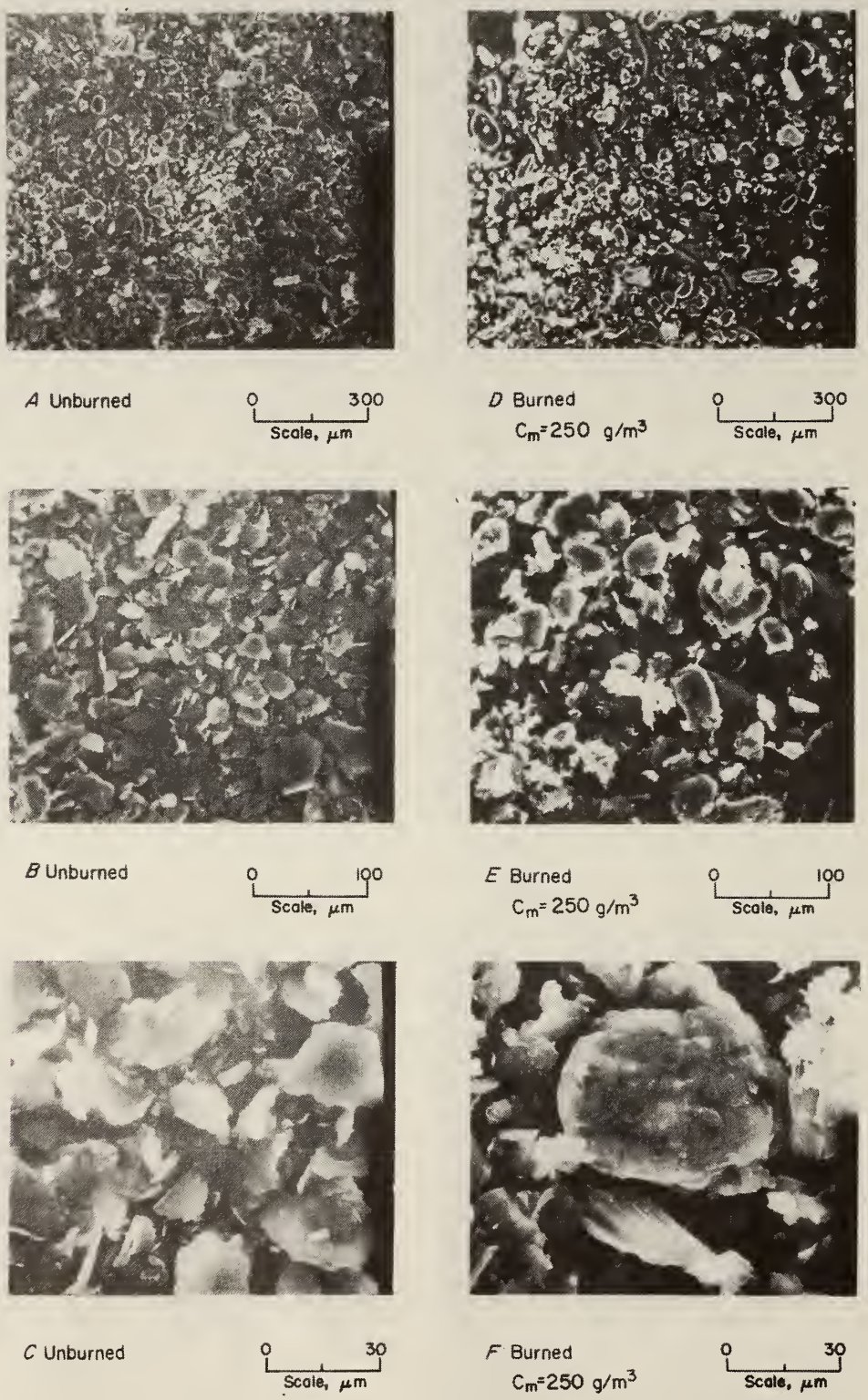

FIGURE 33. - Graphite dust (4-μm), unburned and burned in 50% O_2.

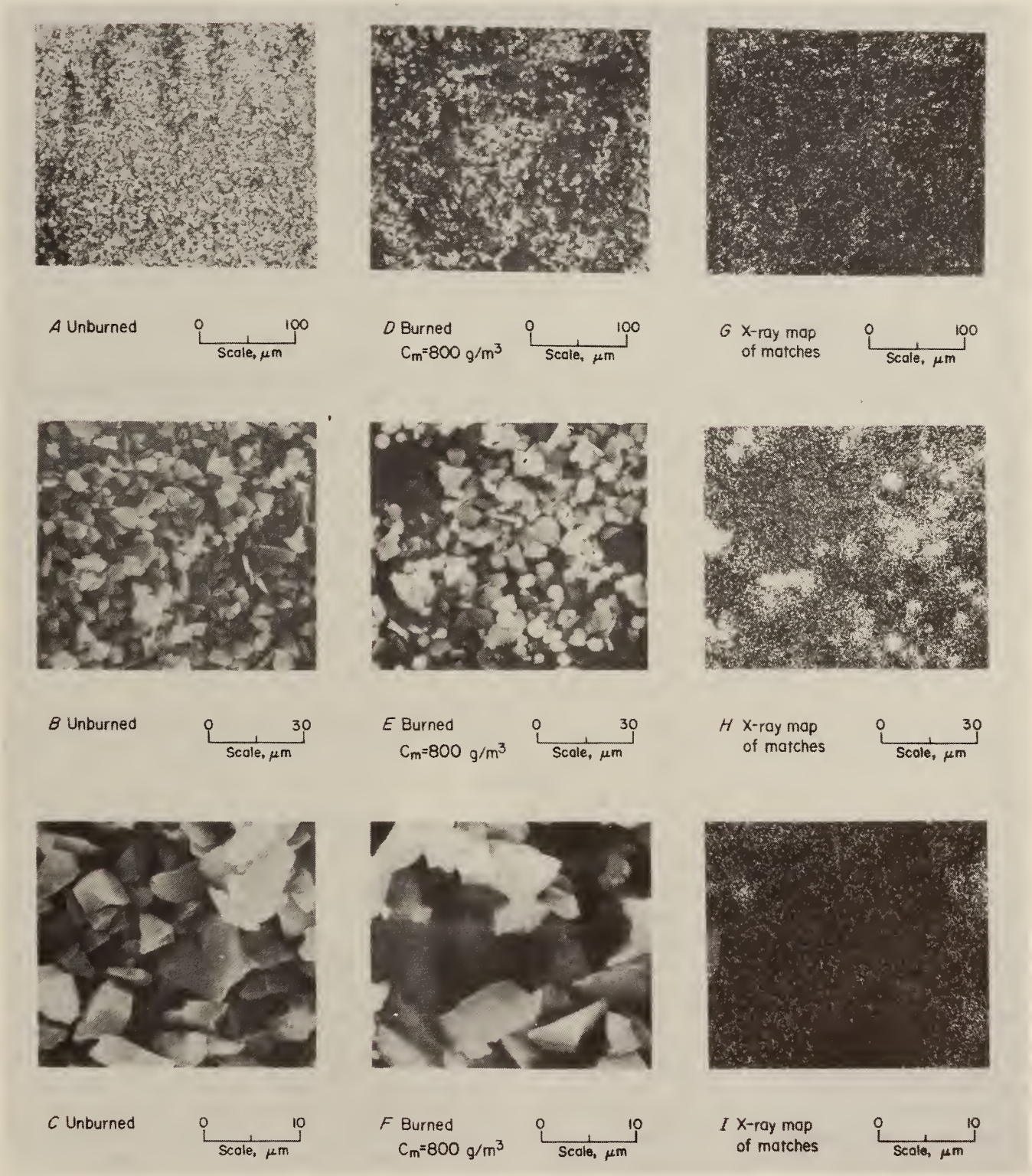

FIGURE 34. - Diamond dust (2-μm). *A-C*, unburned; *D-E*, burned in 50% O_2; *G-I*, X-ray map of match particles using the Pb and Ce lines.

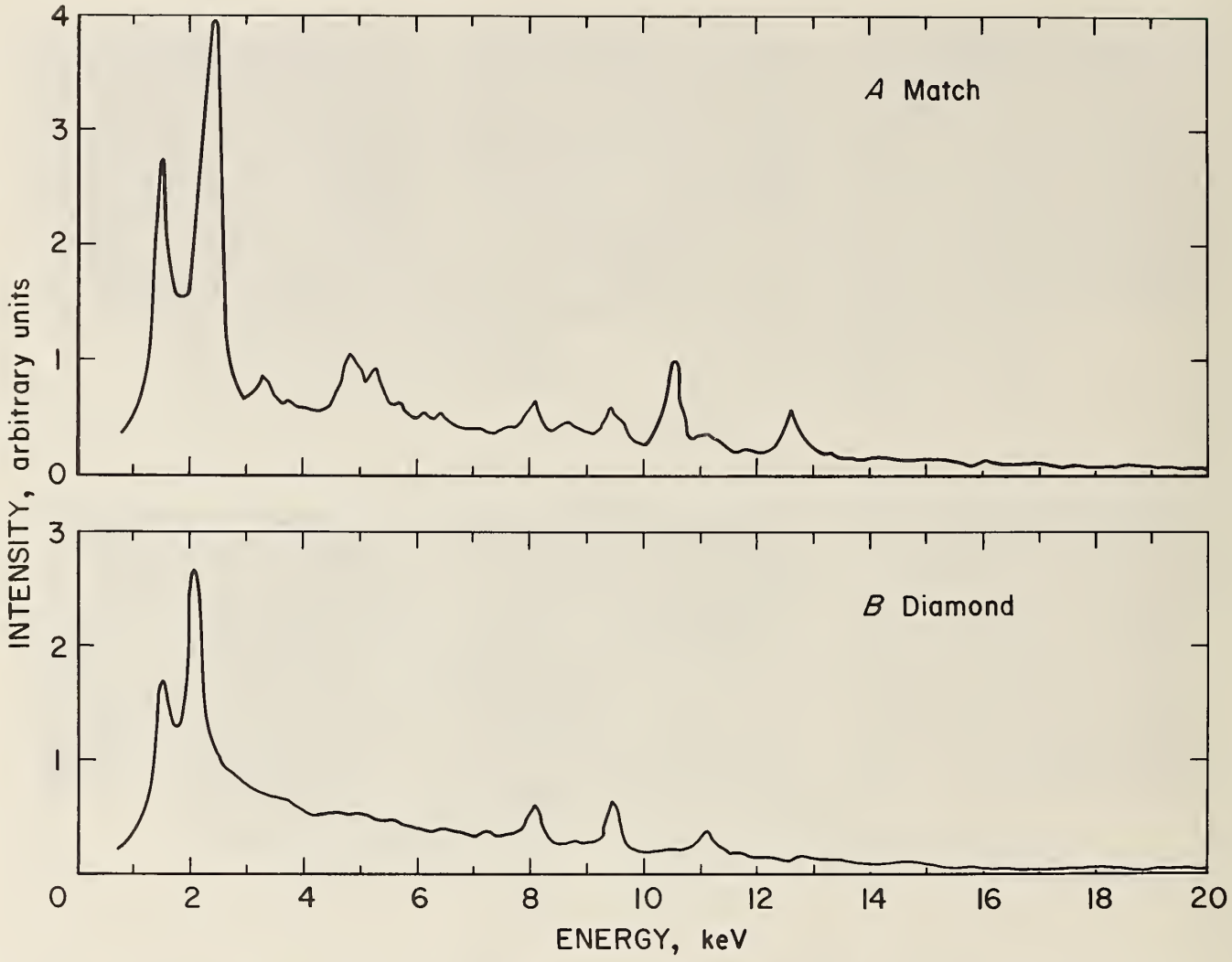

FIGURE 35. - X-ray spectra of diamond and match particles.

and diamond dusts must be quite similar to each other, but their residues are substantially different from those of volatile bituminous coal dusts. The anthracite dust residue is intermediate in nature.

Pittsburgh Coal and Rock Dust in Air

To prevent and suppress coal dust explosions, coal dust can be mixed with inerting agents which act as inhibitors. The one actually used in mines is rock dust. The relative effectiveness of a range of chemicals that can be used for this purpose was studied by the Bureau of Mines, and details are found in the appropriate reports (13-14, 16-17). Pittsburgh coal dust and limestone rock dust ($CaCO_3$) mixtures containing 40% incombustible (I) matter were tested in the 8-L chamber, and the pressure versus concentration data are shown in figure 36. Note that both the coal and total dust concentrations are shown on the horizontal axes. The incombustible content includes both the ash in the coal and the rock dust. Both the coal and rock dusts were minus 200 mesh ($D < 74$ μm), and the mixture had $\bar{D}_s$ = 23 μm and $\bar{D}_w$ = 40 μm. Also shown in the figure are the particle temperatures for these explosions. Comparing figure 36 with figure 10, it can be seen that the explosion pressures and particle temperatures are lower for the 40% incombustible mixture than for the pure coal dust.

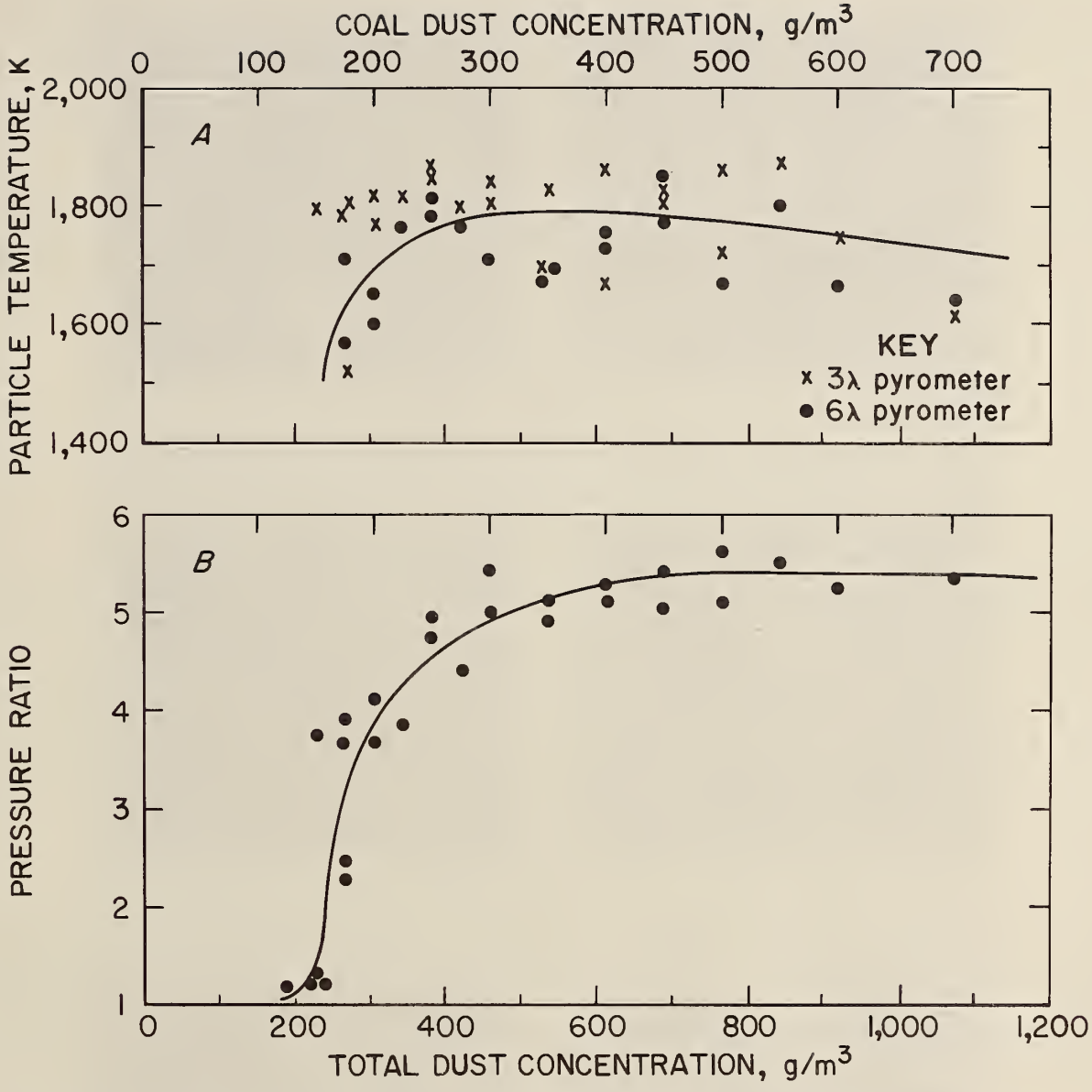

FIGURE 36. - Flammability data from the 8-L chamber for a Pittsburgh coal and rock dust mixture (40% I).

Figures 37*A*-37*C* are micrographs of before-explosion samples of this coal-rock dust mixture. Also shown are calcium K_α X-ray maps to the right of their respective micrographs. These maps can be used to identify the limestone rock dust ($CaCO_3$) particles in the dust mixture since only the rock dust particles appear on the calcium X-ray maps. This strong calcium X-ray line at 3.7 keV is obvious in figure 38, which compares the spectrum of limestone rock dust with that of coal dust. Figure 39 shows the SEM micrographs of the rock-dust-treated coal dust after an explosion at a coal concentration of 400 g/m^3. Also shown are the calcium K_α X-ray maps to the right of their respective micrographs. Notice that there are cenospheres and particles with blowholes, but a few of the particles are unaffected by the explosion and retain their unburned angular, sharp characteristic surfaces. By contrast, micrographs from explosions of the same concentrations of Pittsburgh coal dust (fig. 14) show that all the visible particles are extensively deformed due to heating, reacting,

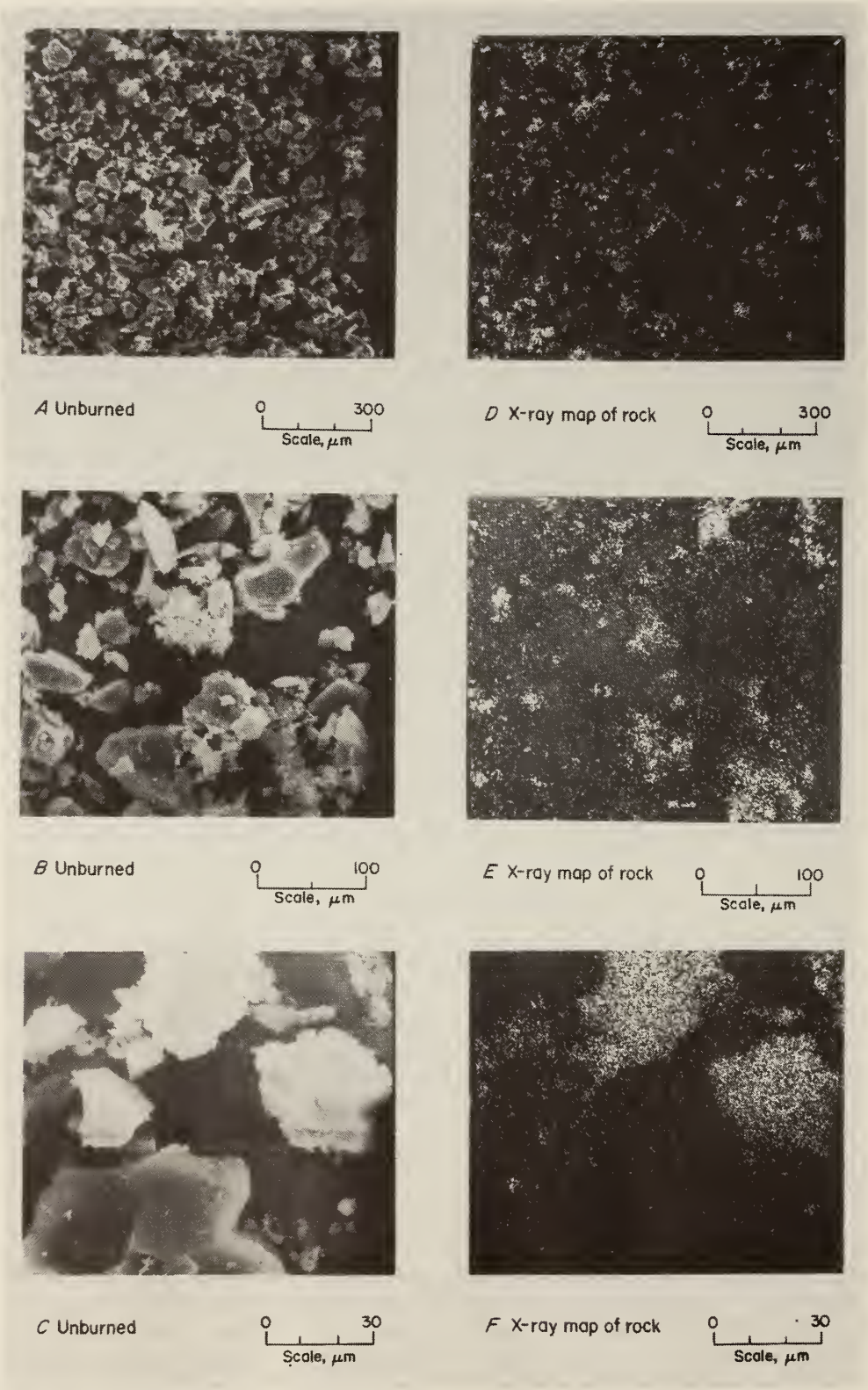

FIGURE 37. - Unburned Pittsburgh coal and rock dust mixture (40% I). X-ray maps made using the Ca line.

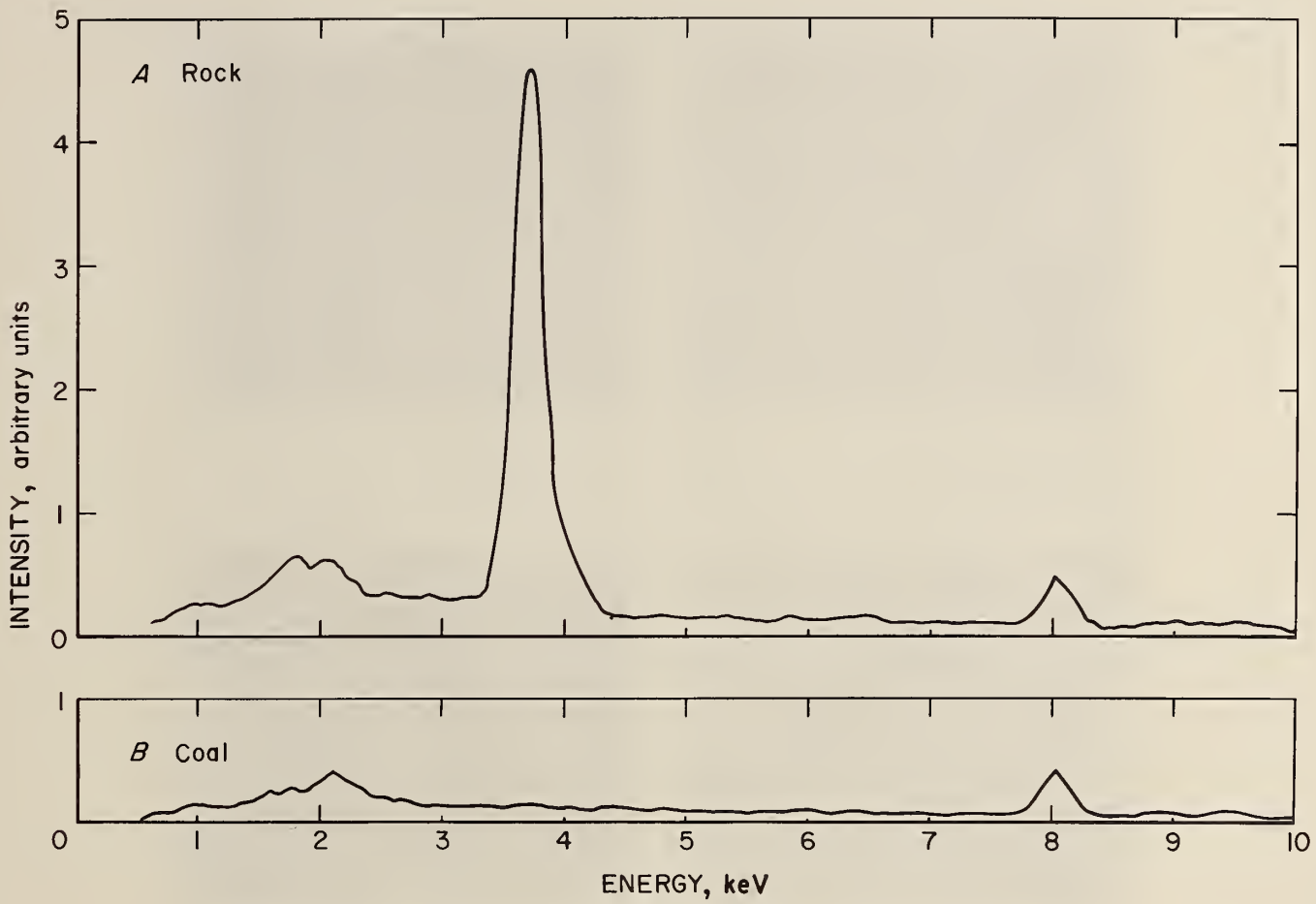

FIGURE 38. - X-ray spectra of limestone rock and coal particles.

outgassing, and devolatilization. The rock dust is believed to function mainly as a thermal inhibitor by absorbing heat from the explosion. The heat can be absorbed by the inert particle itself and/or by its endothermic decomposition to CaO and CO_2. The decomposition product, CO_2 gas, may also help to suppress the explosion.

EXPERIMENTAL MINE DUST EXPLOSIONS

Figure 40 shows an unburned mixture of coal dust with rock dust (60% I), and figure 41 shows the residue from a full-scale mine explosion of the same dust in the Bruceton Experimental Mine (30). Also shown are corresponding calcium X-ray maps to identify the rock dust particles in the micrographs. The appearance of the burned dust particles is very similar to that of those from the laboratory-scale experiment (fig. 39), showing good correlation between the extremes in scale of the experiments. This amount of rock dust (60% I) is less than the amount necessary to totally inert the coal-rock mixture, and therefore the flame propagated the entire length of the dusted zone in the mine. The dust samples for SEM analysis were collected by an automatic sampling system during the passage of the propagating flame.

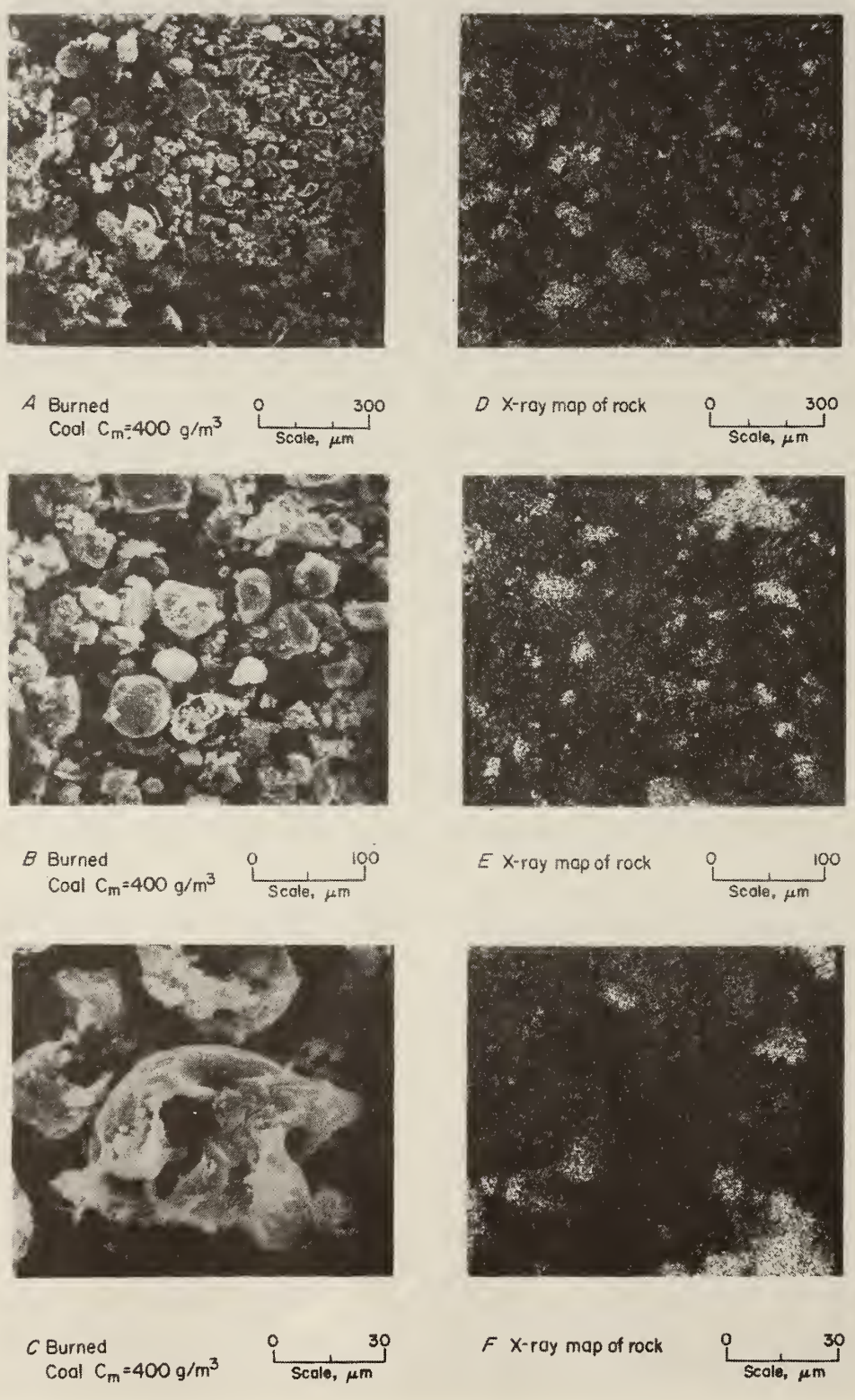

FIGURE 39. - Pittsburgh coal and rock dust mixture (40% I), burned in air. X-ray maps made using the Ca line.

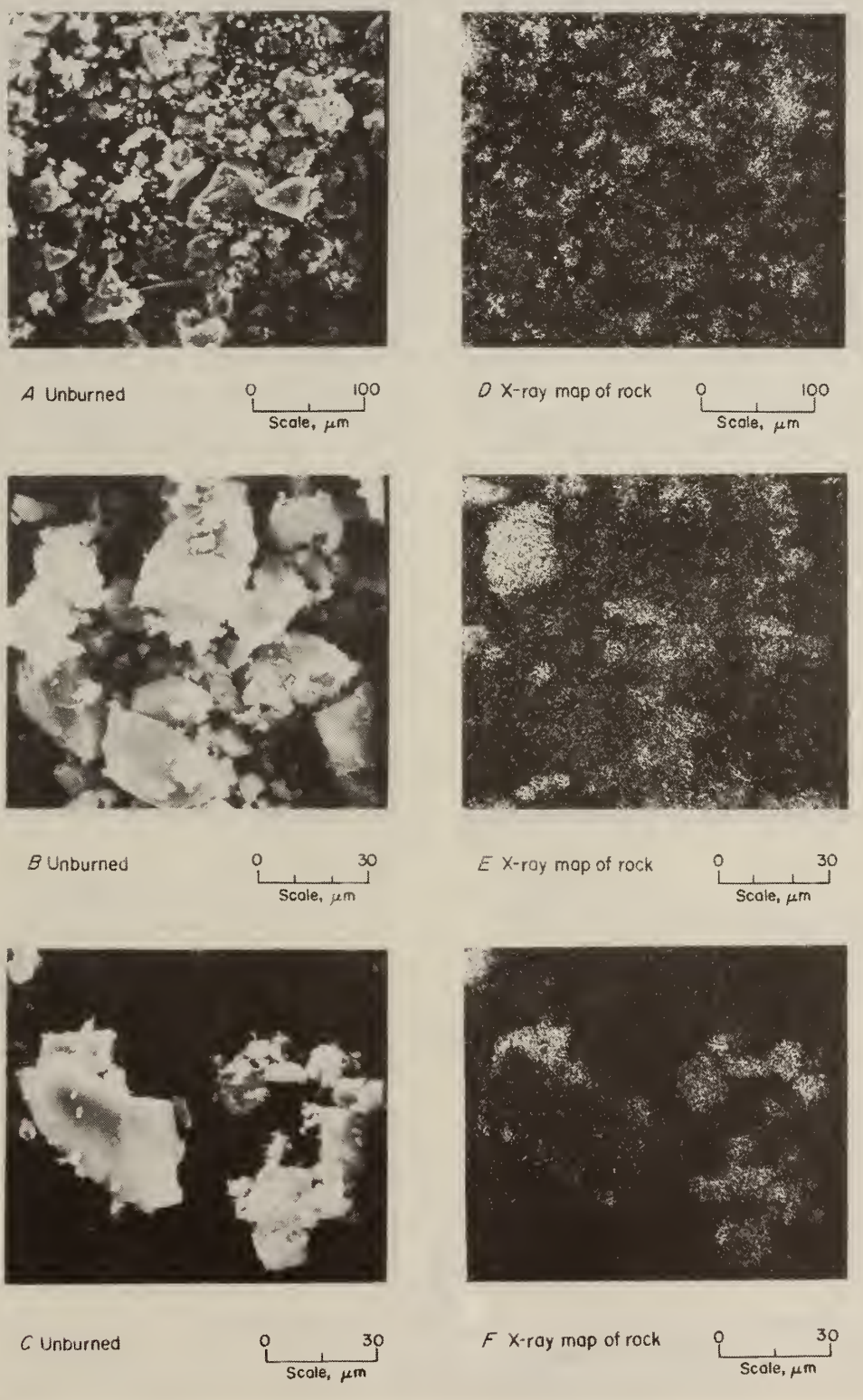

FIGURE 40. - Unburned Pittsburgh coal and rock dust mixture (60% I). X-ray maps made using the Ca line.

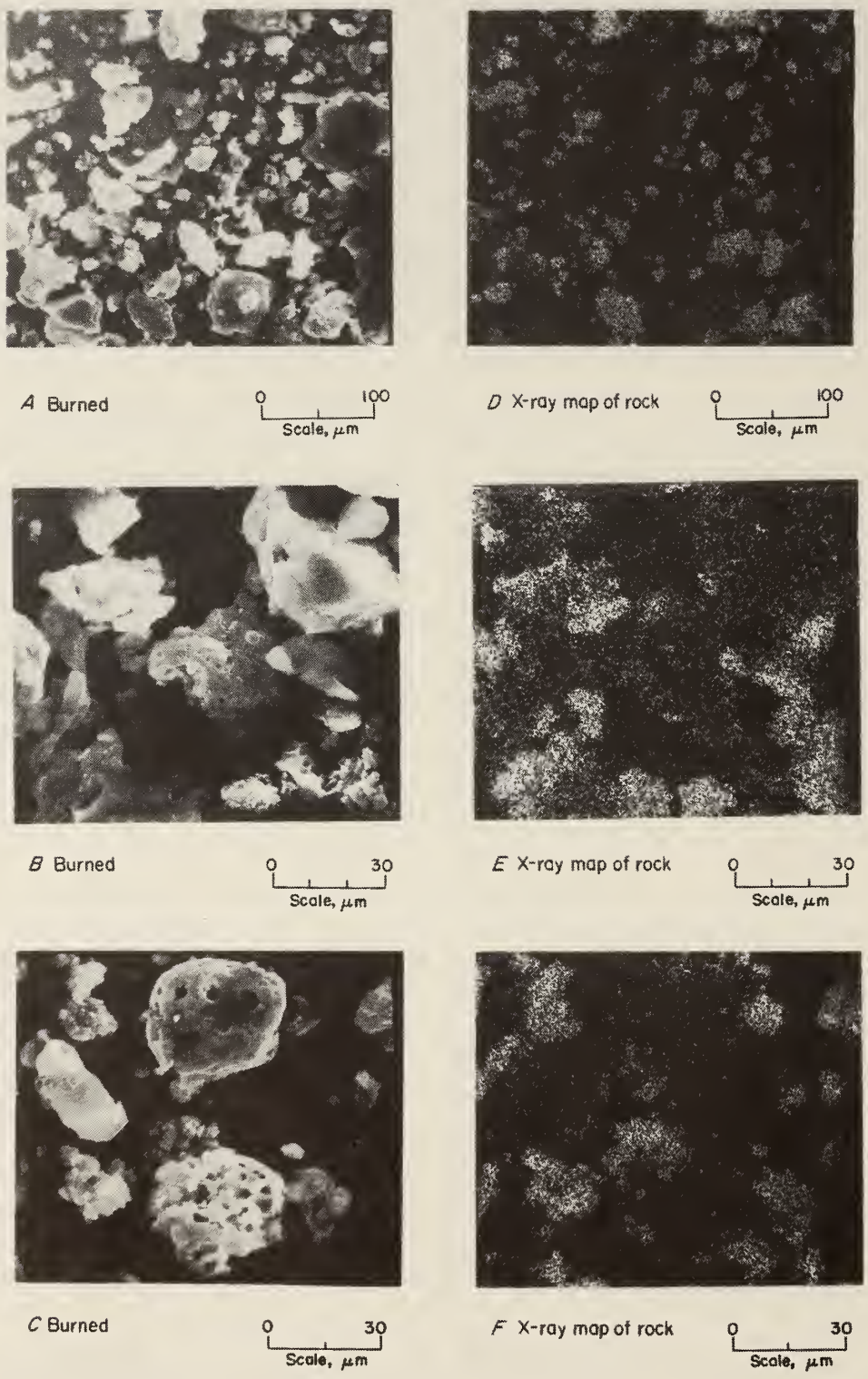

FIGURE 41. - Pittsburgh coal and rock dust (60% I), postexplosion sample from the Bruceton Experimental Mine. X-ray maps made using the Ca line.

MINE EXPLOSION DISASTER INVESTIGATIONS

The Bureau's scanning electron microscope has also been used to assist in the investigation of mine explosion disasters at the request of the Mining Safety and Health Administration (MSHA) of the Department of Labor. In one disaster (10) in which 15 miners were killed, a mine explosion occurred following a methane outburst in a Colorado mine. MSHA investigators suspected that the ignition source for the explosion might have been an electric arc in an improperly assembled explosion-proof compartment on a continuous mining machine. Dust samples collected from within this compartment were examined with the SEM. The presence of burned dust particles in the samples, together with other evidence, led the MSHA investigators to conclude that the probable ignition source was an arc in the improperly assembled compartment leading to a propagating methane explosion.

DUST EXPLOSIONS IN A 1.2-L FURNACE

Figure 42 is a schematic of a new 1.2-L furnace developed by Conti and others (8) to measure the thermal ignitability of dust clouds. The ceramic combustion chamber was wrapped with Nichrome heating wire and then surrounded with insulation. Four access holes pass through the furnace tube. Two are used for thermocouples, a 12.5-mil (320-μm) Chromel-Alumel type K thermocouple at the wall of the furnace for control of the furnace temperature, and a 1-mil (25-μm) platinum-rhodium type S thermocouple positioned in the center of the furnace to observe rapid changes in temperature at ignition. The other two holes are used for the microprocessor-controlled rapid-sampling system, which will be described in detail in a later paragraph. Probing vertically along the furnace tube with a thermocouple indicated a relatively uniform axial temperature profile along the tube length. A reasonably uniform dust

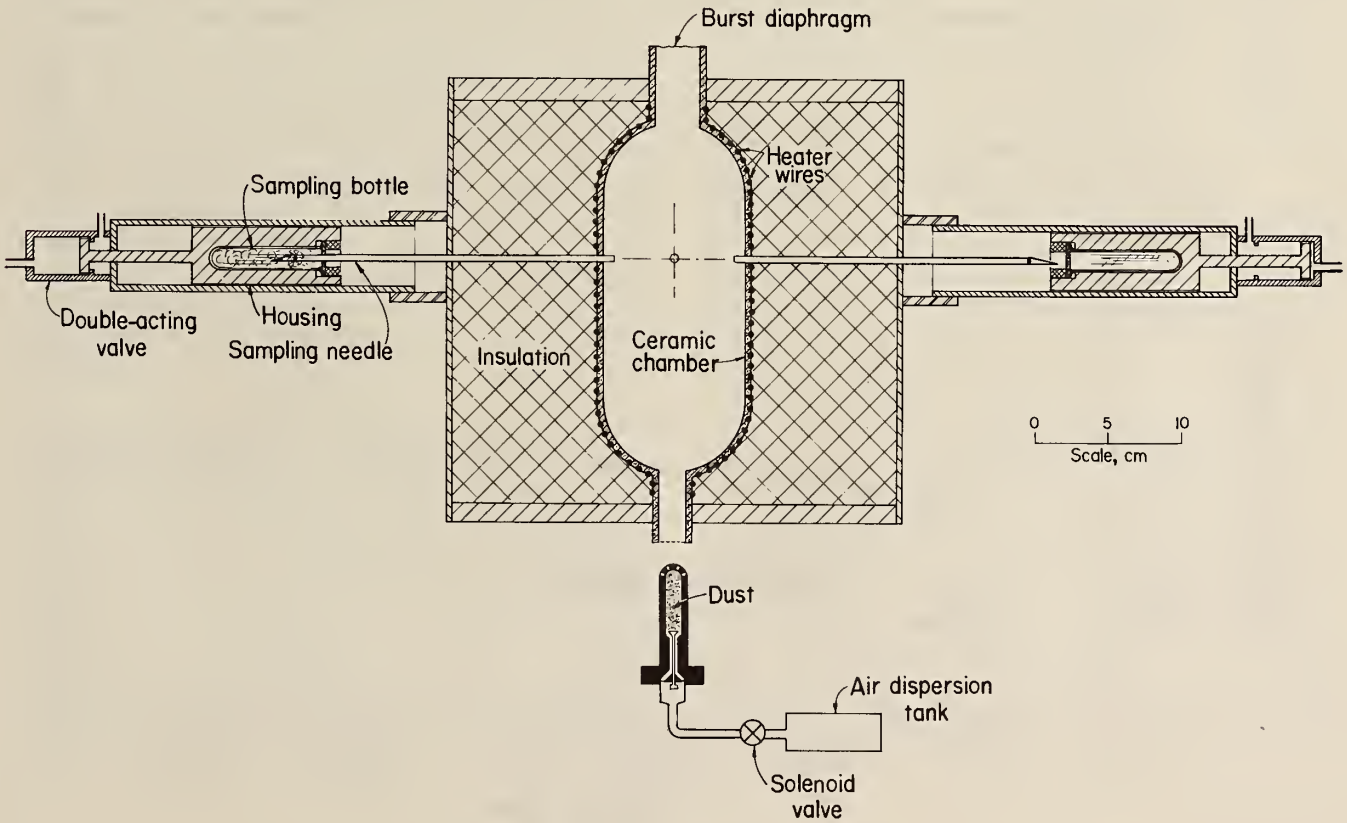

FIGURE 42. - 1.2-L furnace and rapid sampling system (8).

distribution within the furnace tube was also measured by a miniature dust probe (7).

The dust to be tested is placed in a brass dispersion receptacle at the base of the furnace. To minimize preheating of the dust, the receptacle was inserted into the furnace just before dispersion. The receptacle is also fitted with a ceramic cloth sleeve which serves as insulation and as a seal along the receptacle's length. The nozzle of the dust receptacle contains a number of small holes through which the dust is ejected by a 30-msec pulse of air from a dispersion tank. In these furnace tests, the maximum possible exposure time for the dispersed dust was several seconds, before the dust would settle. The criterion for ignition in the tests was the rupture of the diaphragm (at 0.2 to 0.3 bar) and flame emitting from the top of the furnace.

The data in figures 43 and 44 are used with the kind permission of R. S. Conti (8). Figure 43 shows pressure (absolute) and temperature (from the 1-mil thermocouple) traces for a thermal ignition of Pittsburgh coal at a concentration of 260 g/m^3 in the 1.2-L furnace. The furnace temperature was 600° C, slightly above the minimum autoignition temperature for

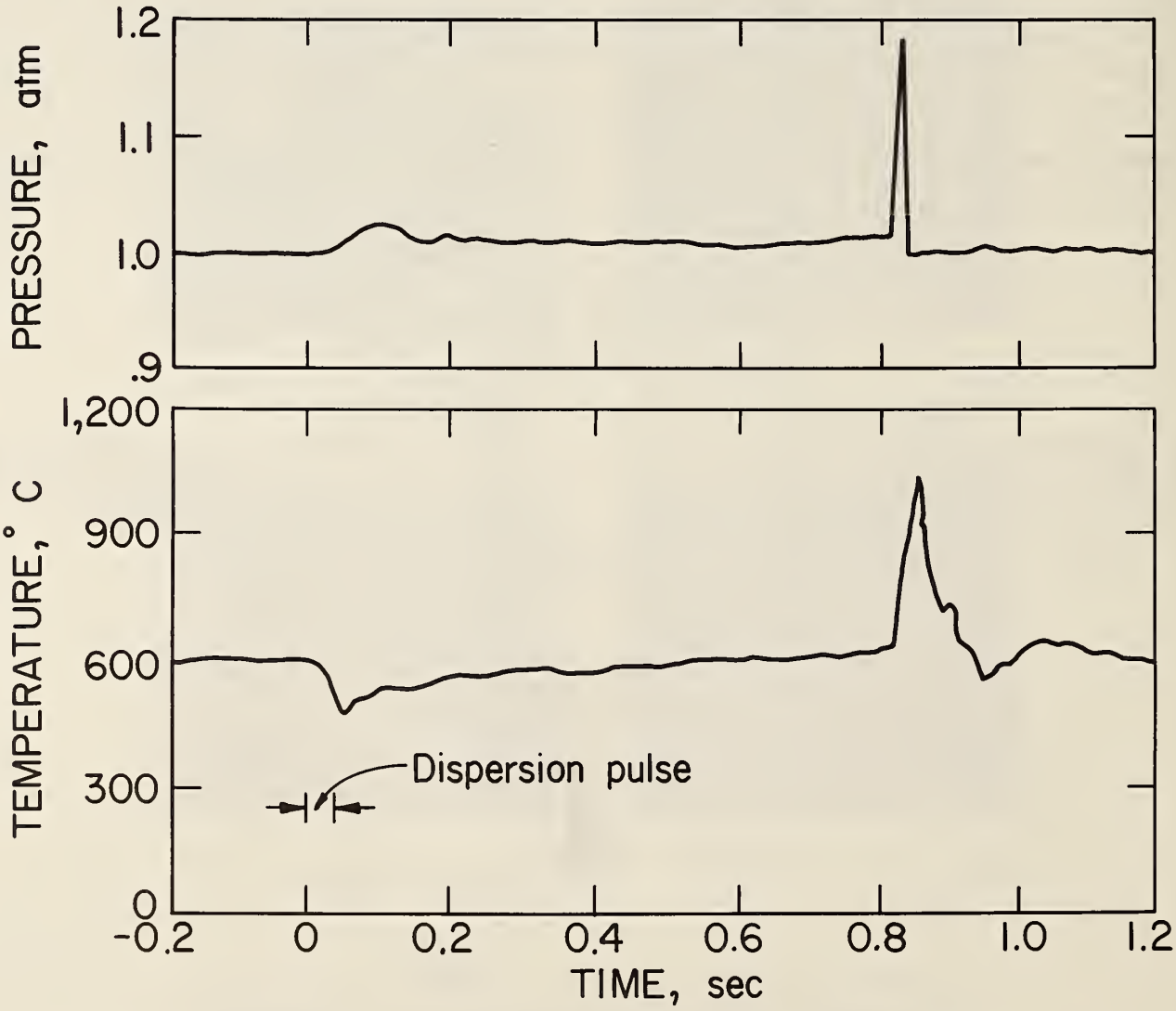

FIGURE 43. - Pressure and thermocouple recorder traces from an explosion in the 1.2-L furnace.

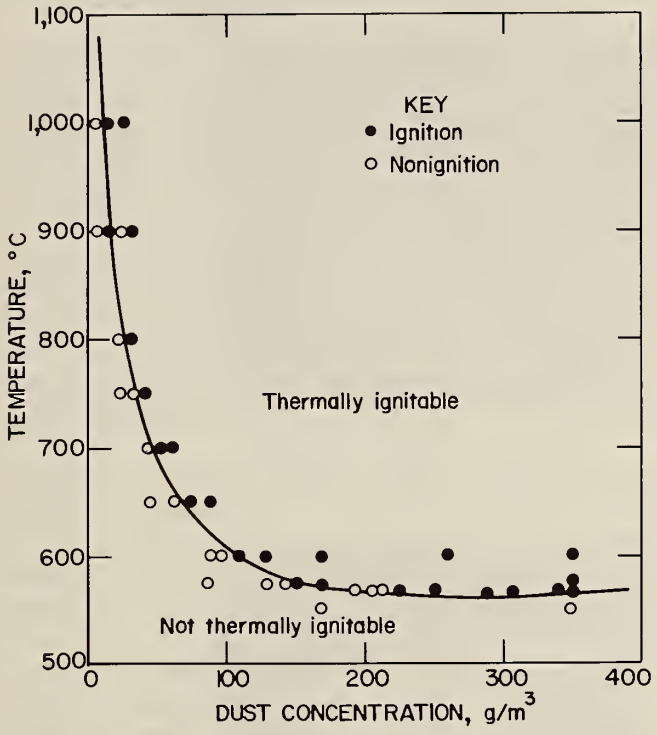

FIGURE 44. - Dust cloud thermal ignition data from the 1.2-L furnace for 55-μm Pittsburgh coal in air.

this dust. There is a drop in temperature as the dust is dispersed into the furnace, but the dust-air mixture temperature rises quickly to the set temperature of the furnace walls and then thermally ignites at about 0.8 sec after dispersion. Ignition is shown by the rapid rise in pressure and temperature, followed by a sudden drop in both as the diaphragm ruptures and the combustion products vent and cool.

Figure 44 shows the thermal autoignition temperature (AIT) data for the size-classified Pittsburgh seam coal dust (35% volatility, $\bar{D}_s$ = 55 μm, and $\bar{D}_w$ = 62 μm) dispersed in the preheated 1.2-L furnace. The concentrations are the nominal concentrations, namely the mass of dust divided by the chamber volume. No corrections are included for the reduction in the mass concentration of oxygen at the elevated temperatures. The minimum AIT is 550° C, and that minimum value is approached asymptotically at the higher dust concentrations. The general shape of the curve for coal is similar to that observed for other hydrocarbons, solid or liquid.

Dust residues as well as gaseous products were sampled with the apparatus shown in figure 42. Sampling is accomplished by plunging an evacuated glass tube (sealed with a rubber stopper) against the sharp needle. When the stopper is pierced by the needle probe, gaseous and dust samples are drawn into the sampling tube. The mechanism that actuates the sampling tube is controlled by a microprocessor. The timing and the duration of sampling are precisely controllable. For 55-μm Pittsburgh coal dust at a concentration of 260 g/m^3 and at an initial furnace temperature of 600° C, samples were collected while the dust was being heated and after it ignited. SEM micrographs of the unburned dust are shown in figure 45. The heated dust particles (fig. 46) were sampled at a time of 0.76 sec after dispersion (see fig. 43), and the burned particles (fig. 47) were sampled at a time of 1.06 sec, which was just after ignition and diaphragm rupture. In the preheated system (fig. 46), there is clearly substantial devolatilization of many particles prior to ignition. Although some particles are unchanged, others contain plentiful blowholes, and many particles appear as strongly devolatilized as the postignition residues. These data suggest that the autoignition process involved devolatilization prior to the thermal ignition of the gas phase mixture of coal tar volatiles in air. The postexplosion sample (fig. 47) contains mostly burned particles, but a few particles appear almost unchanged. This is due to the fact that the diaphragm ruptured before the explosion propagated throughout the entire chamber, thus leaving a few relatively unchanged particles.

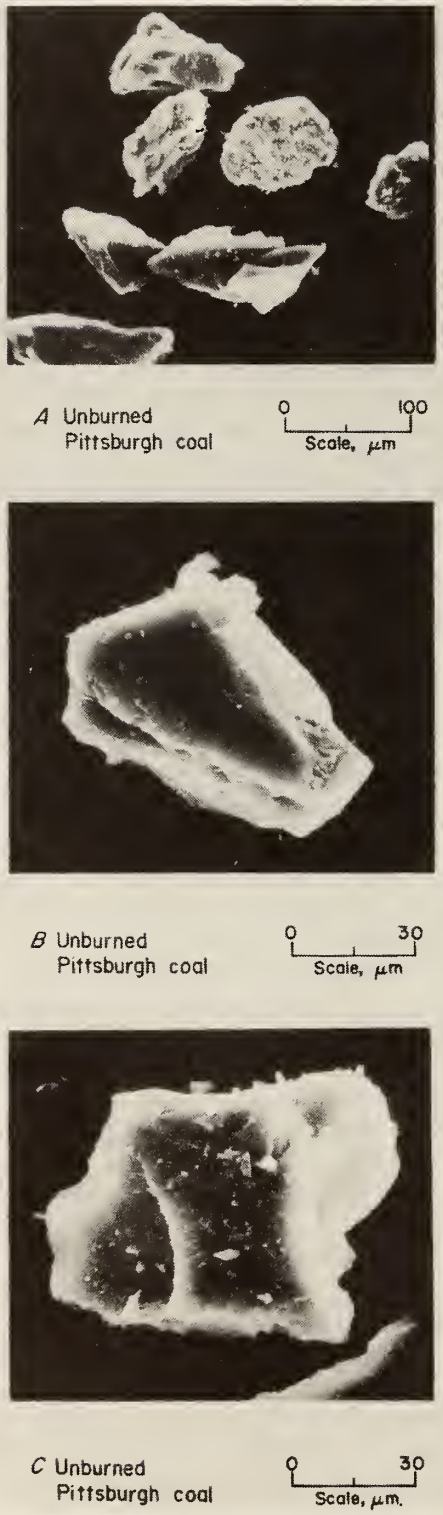

FIGURE 45. - Unburned Pittsburgh coal dust (55-μm).

LASER PYROLYSIS OF COAL DUST

The dust residues from the 8-L flammability apparatus described in the previous sections gave information about the combustible dusts after the explosion process was completed. The explosion event occurs in an experimental time τ_{exp} of seconds. During that time interval, the coal particles are subjected to intense energy fluxes, varying from about 30 to over 200 W/cm^2. The results observable after an explosion are integral effects of combustion over the time τ_{exp}.

One would like to be able to observe the coal particle at intermediate stages during the evolution of the explosion. This is very difficult in the 8-L apparatus because one cannot stop the progression of an explosion once it is initiated. A separate project was therefore initiated to address the question of coal pyrolysis under rapid and intense heating. A high-energy infrared CO_2 laser capable of delivering up to 200 W of continuous radiation at a wavelength of 10.6 μm or operating in the pulse mode for durations from 1 msec to tens of seconds is used to simulate the rapid heating condition in an explosion. A single pulse of laser radiation is directed at a small quantity of coal dust supported on a substrate, and the peak energy and duration of the laser pulse are varied to simulate the rapid heating of a coal particle in an explosion. The brief application of the pulse allows one to isolate the particle at different stages of the combustion process. Preliminary results in which an unfocused laser beam at approximately 80 W/cm^2 is operated in pulses of 70 to 1,000 msec are described here. The heated coal particles were examined in the SEM, and the results are shown in figure 48, where they are compared with the original, unheated dust. This was the size-classified Pittsburgh coal with $\bar{D}_s$ = 84 μm and $\bar{D}_w$ = 89 μm, shown in figure 9.

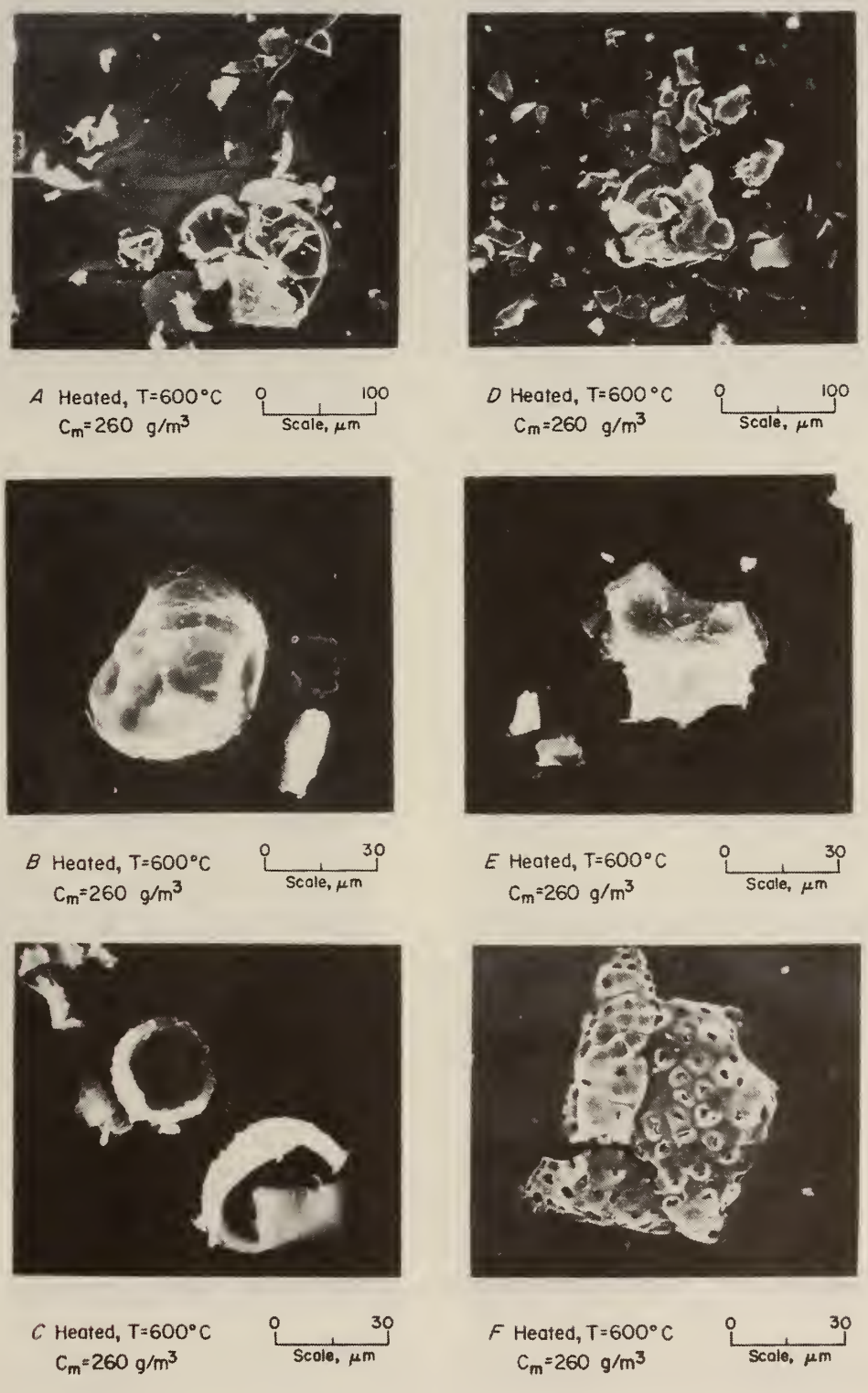

FIGURE 46. - Pittsburgh coal dust (55-μm), heated in the 1.2-L furnace but before thermal ignition.

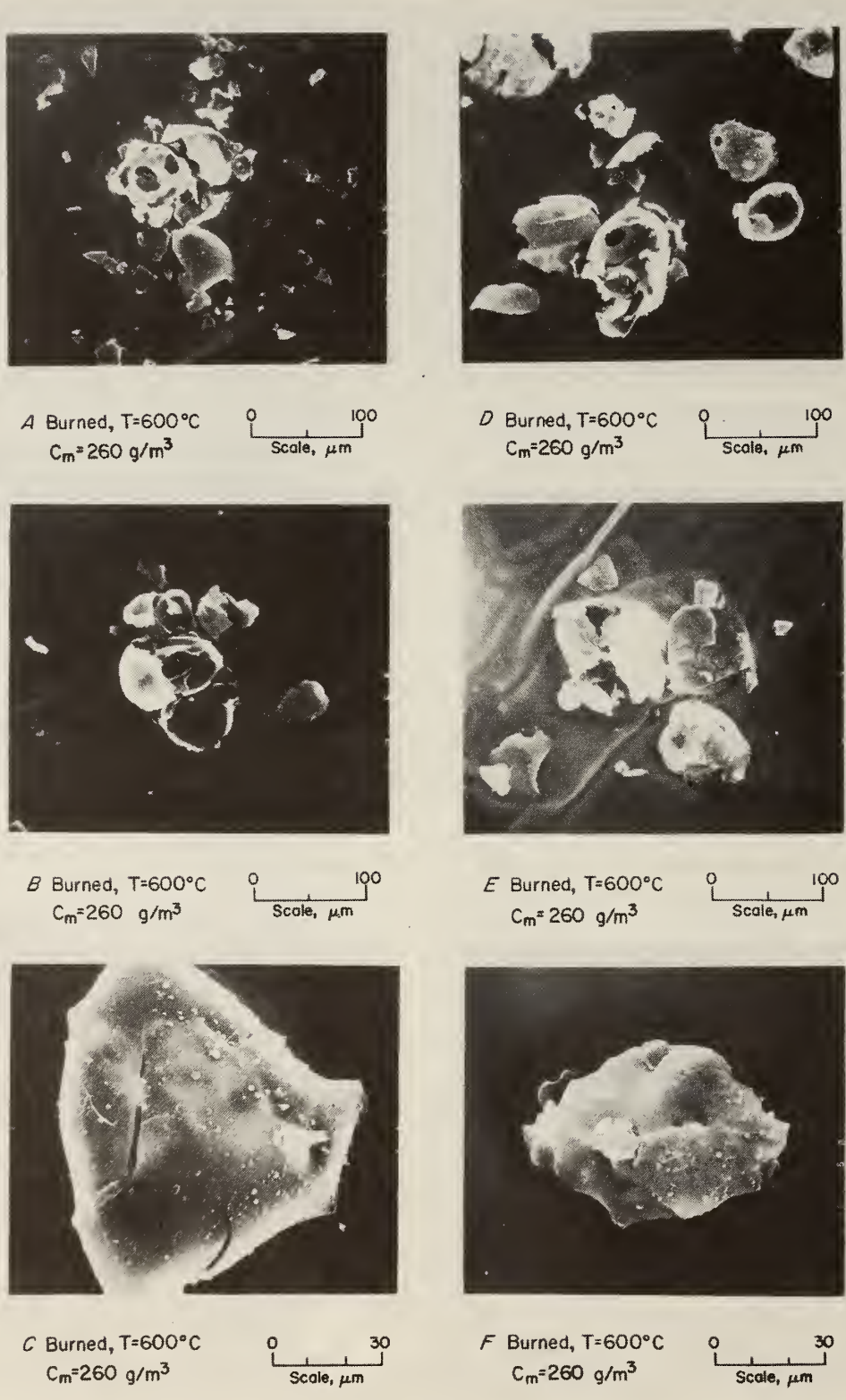

FIGURE 47. - Pittsburgh coal dust (55-μm) after an explosion in the 1.2-L furnace.

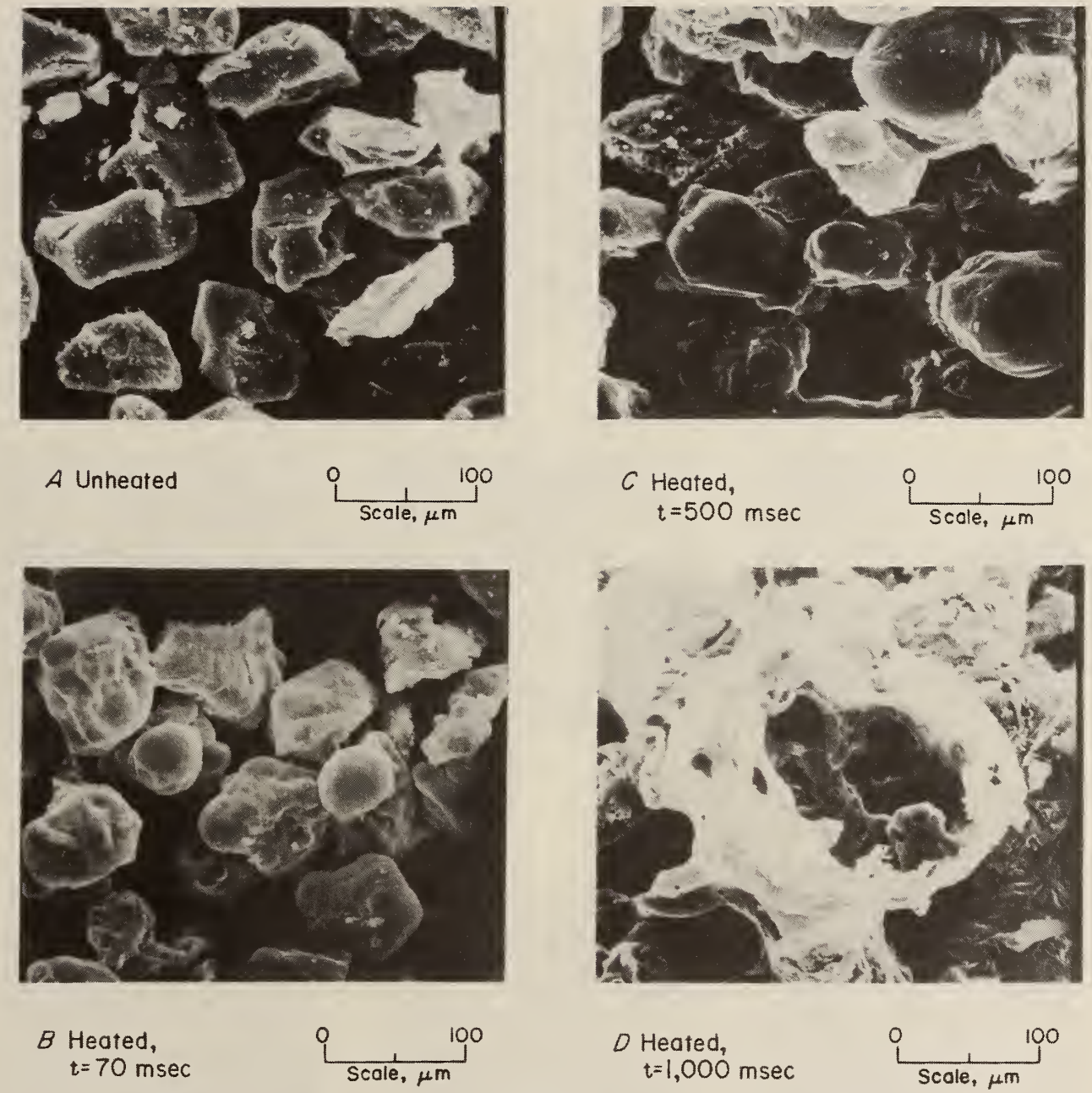

FIGURE 48. - Laser-pyrolyzed 84-μm Pittsburgh coal at various heating times.

At 70 msec (fig. 48*B*), the particles showed the first stage of devolatilization. The coal became plastic and fluid, and the characteristic sharp angles of the particle surfaces became smooth. With a longer pulse time (500 msec), the coal particles became more fluid, and surface tensional forces produced the surface of minimum energy which is a sphere (fig. 48*C*). At even longer pulse lengths (1,000 msec, fig. 48*D*), the volatiles began to ignite owing to the intense heating effect of the laser beam. Blowholes and the other familiar features of coal dust residue from a violent explosion in the 8-L apparatus were produced. Further development in this project and the SEM study of the coal dust residues should lead to better knowledge of the detailed combustion and explosion processes of coal.

SLOW HEATING OF COAL DUST

The surface characteristics of coal particles also change when the dust is heated slowly. To examine this effect, 20-g samples of Pittsburgh seam coal dust were placed in a preheated furnace at 120°, 140°, 300°, and 500° C. When the dust reached the furnace temperature, a sample was taken for SEM analysis, and the results were compared to the original, unheated dust. The dust studied was 200 by 100 mesh coal with an average size of about 100 μm.

At 120° and 140° C, the SEM micrographs of the heated dust showed no obvious changes from the original dust. Figure 49 shows the changes that occurred at the higher temperatures. On the left (figs. 49*A*-49*C*) are the original, unheated coal particles at three magnifications. The center column (figs. 49*D*-49*F*) shows changes in the surfaces of the particles at 300° C. The right column (figs. 49*G*-49*I*) shows the rounding of the particles as the coal becomes plastic at 500° C.

SURFACE CHARACTERISTICS OF BITUMINOUS AND LIGNITE COALS

The surface features of unheated Pittsburgh coal and a lignite coal are quite different, as can be observed in figure 50. The bituminous coal has very sharp angular edges but smooth surfaces. The lignite coal particles do not show any well-defined edges, and the surfaces are rough and show extensive pore structures. The difference in surface features could be the reason for the different properties of the two coals. Lignite coals are more susceptible to spontaneous combustion (20), which is due to the oxidation of coal by air. The release of heat in the oxidation process raises the temperature of the coal and eventually results in sustained combustion. The larger surface area per unit mass of lignite coal and the possible chemical structure differences of the coals are responsible for the increased susceptibility to spontaneous combustion.

CHEMICALLY TREATED WOOD

Timbers used in mines are sometimes chemically impregnated with fire-inhibiting chemicals for improved fire resistance (37). The impregnation is accomplished by immersing timbers in a solution under hydrostatic pressure. One such commercially available timber treatment (NCX) contains a phosphorus compound. When a sample was made from one of these chemically treated oak timbers and examined by the SEM using the energy-dispersive X-ray analyzer (EDS), the only prominent X-ray signal detected was the phosphorus X-ray line. The relative concentration profile of the phosphorus-containing chemical was determined by plotting the relative intensity of the phosphorus X-ray signal as a function of distance from the surface of the sample. The result is shown in figure 51, which includes a photograph of the wood cross section and a corresponding graph of the relative distribution of phosphorus in the treated wood. The graph shows a gradual decrease in the amount of phosphorus from the surface (left side of figure) to the interior (right side) of the wood sample. Another sample from a piece of this chemically treated wood that was charred (21) by exposure to an intense heat lamp for 1 min was similarly prepared and examined. The resulting relative concentration profile and corresponding photograph are shown in figure 52. There seems to be an enrichment of the phosphorus chemical on the surface, which might be due to migration to the surface of the phosphorus compound during heating. This may be a contributing factor to the well-known fire resistance characteristic of a phosphorus-treated material (25, ch. 2).

FIGURE 49. - Pittsburgh coal dust slowly heated in a furnace at various temperatures.

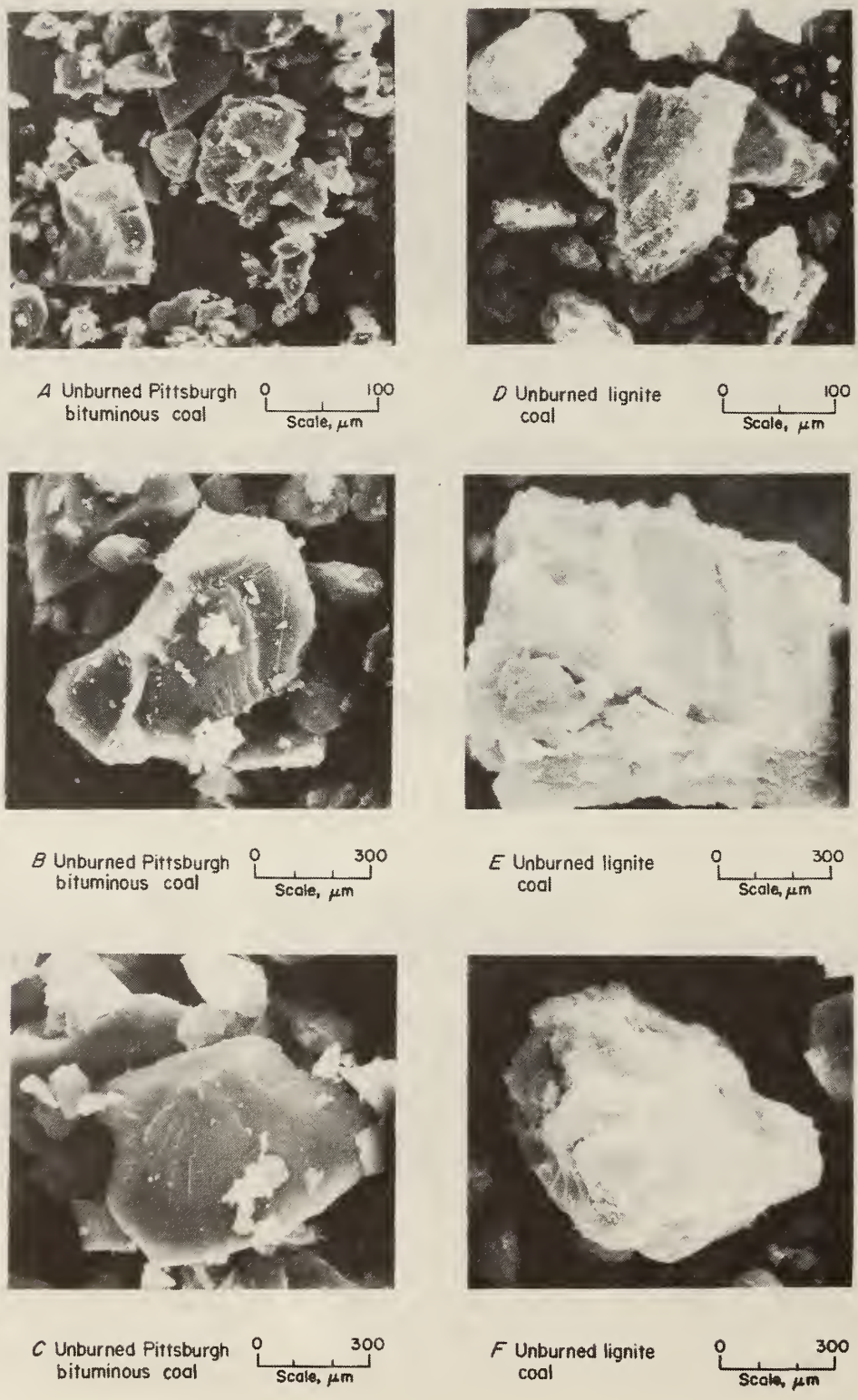

FIGURE 50. - Comparison of surface characteristics of bituminous and lignite coals.

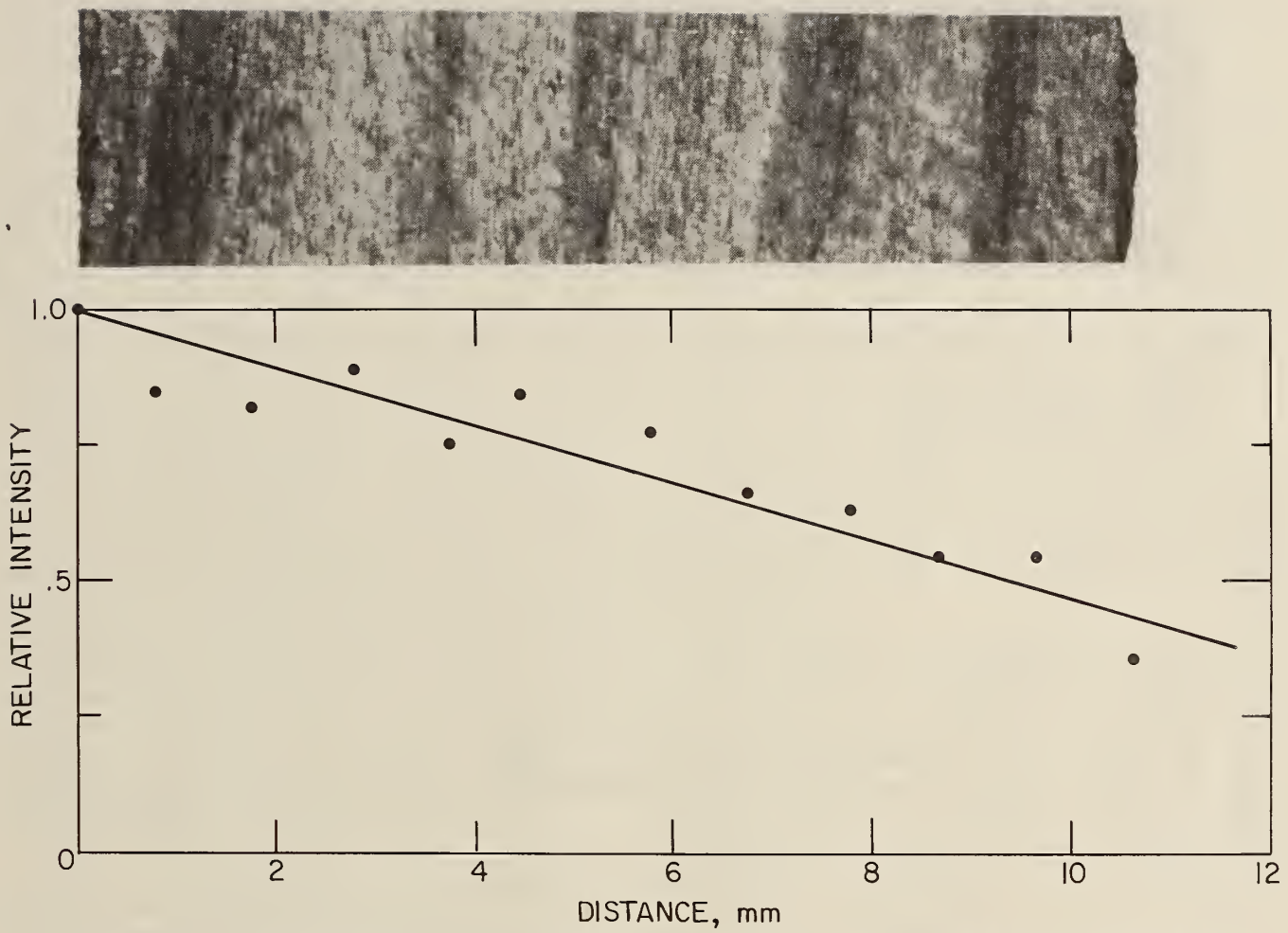

FIGURE 51. - Relative distribution of phosphorus as a function of distance from the surface, in oak timber chemically treated with NCX inhibitor.

DISCUSSION

Microscopic observations such as those in the present report should certainly contribute to improved theories of combustion. Unfortunately, only a few researchers have studied the true microscopic details of combustion events in dust explosions. Smoot, Horton, and their colleagues (18, 33-34) published scanning electron micrographs of Pittsburgh seam coal particles before and after traversing the flame front of a coal dust-air burner flame. During the short time (about 50 msec) that the particles traversed the flame front, they lost their original sharp edges and angular appearance and became more spherical. Many particles showed blowholes due to escaping volatiles. From the SEM micrographs, the particles did not appear to change much in size during the traverse of the flame front, but a Coulter Counter size analysis of collected particles showed a slight increase in average size.

Similar results were found by Milne and Beachey (27), who also used a flat flame burner to study coal dust flame propagation. Their SEM micrographs also show rounded particles with extensive blowholes.

Lightman and Street (24) extensively studied coal particles heated in furnaces, shock tubes, and large combustors.

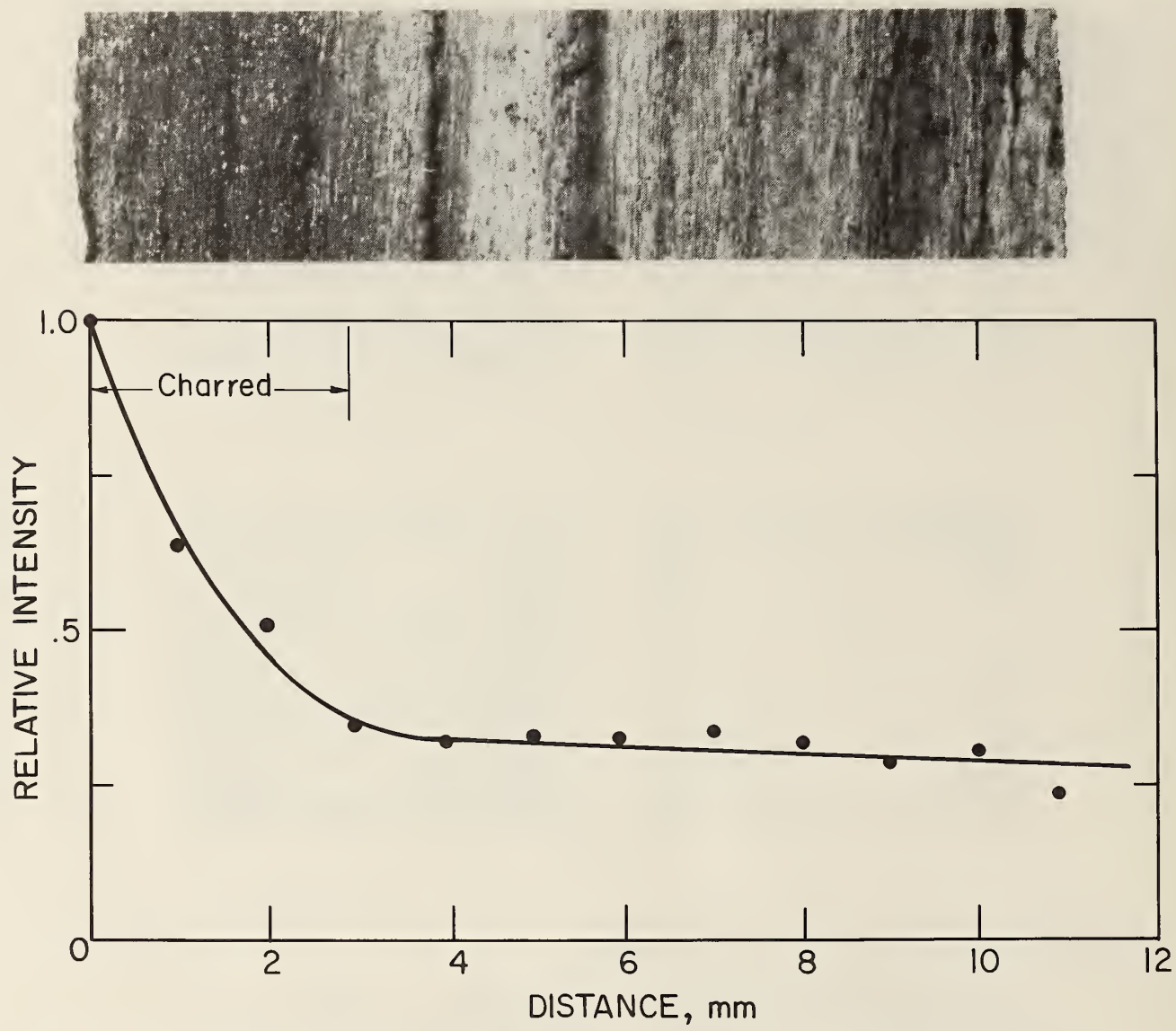

FIGURE 52. - Relative distribution of phosphorus as a function of distance from the surface, in chemically treated oak timber after charring.

They observed the collected particles with both electron and optical microscopy. In the drop tube furnace, 60- to 110-μm particles were heated in air as they fell through the furnace in a period of about 1 sec. At furnace temperatures of 400° to 500° C, they observed internal gas bubbles in the particles due to the evolving volatiles and some blowholes as the volatiles escaped the surfaces of the particles. At higher temperatures (up to 1,200° C), various types of cenospheres (29) were observed. These particles were sometimes twice their original size. The lower temperature furnace results are comparable to the SEM micrographs from the 1.2-L furnace (figs. 46-47). The high-temperature results are similar to the postexplosion residue for 84-μm Pittsburgh coal from the 8-L chamber (fig. 25).

Lightman and Street (24) used shock tubes to study the rapid heating of coal particles in atmospheres of air and nitrogen. Cenospheres were observed for temperatures of 900° to 1,300° C behind the reflected shock wave. The residues

from their large combustor showed four types of char: solid particles, lacy cenospheres, balloon cenospheres, and thick-walled cenospheres. The internal structure of the cenospheres was studied by embedding the particles in a resin, and then sectioning the sample and observing it with an optical microscope.

In a later study, Street, Weight, and Lightman (36) studied the structural changes in pulverized coal during rapid heating in the drop-tube furnace in atmospheres of air and nitrogen. The structures of the chars formed in the oxidative and inert gases were different. The particles heated in nitrogen tended to be more open and form more "balloons" or cenospheres; they also had smaller pores than the particles heated in air. Swelling of the coal particles was observed to be influenced by the duration and temperature of the experiment. They also found that, with the exception of fusain (which formed solid particle chars), it was impossible to relate exactly the char types to particular lithotypes of the original particles.

Seeker and others (31) also studied the behavior of individual particles (40 and 80 μm) passing through a heated gas zone, created by a lean methane-air flame. They collected particles for SEM analysis and also used holography to study the devolatilizing particles in situ. Particle heat-up times were of the order of 10^5 ° C/sec. For bituminous coals, they observed volatiles jetting from the particles and an increase in particle size. Blowholes were also observed in the collected particles. For anthracite, they did not observe the volatile jets.

McLean, Hardesty, and Pohl (26) also observed the pyrolysis of coal particles (about 100-μm size) by injecting them into the centerline of a high-temperature reactor fueled by a flat-flame gas burner. They used high-magnification shadowgraphs of the in situ particles and micrographs of the collected particles. They observed the generation of volatiles from the bituminous coal particles with the shadowgraph. The collected particles appeared to have melted and swelled, similar to those in figure 25.

Helwig (12) studied the rapid (>>1,000° C/sec) pyrolysis of narrow size distributions of coal dusts in an inerted furnace. For 20- to 30-μm particles at a furnace temperature of 1,000° C, a "lively bursting" and devolatilization is observed. For larger (60- to 75-μm) particles, a swelling of the particles is observed as they become plastic, but the heating rate is not sufficient to rupture the particles. Helwig suggests that under a given condition, only coal particles smaller than a certain size could attain a high enough heating rate to become liquid and allow a high enough gas pressure to build up to rupture the liquid surface as resolidification was occurring.

The Bureau's systematic microscopic investigations of postexplosion dust residues have led to similar observations. The burned bituminous coal dusts are usually significantly larger than the unburned particles. The surfaces of these burned char residues are rounded and smoothed, in contrast to the angular features and sharp edges of the unburned coal. The burned particles are pockmarked with blowholes, and some are blown into large cenospheres. Clearly, the coal particles that generated the dust explosions were subjected to rapid heating, causing them to pyrolyze and to soften or melt into a plastic phase. The heavier, higher-molecular-weight pyrolysis products are liquid, and surface tension forces cause them to assume a spherical shape. However, at the same time, the lighter-molecular-weight products of pyrolysis are devolatilizing (38). The internal pressures resulting from the devolatilization of these lighter components generate bubbles in the liquid mass of the heavier components. But the liquid mass is simultaneously reacting internally, and at about the same time that gas bubbles are appearing and bursting, competing condensation reactions occur in the liquid that generate an inert solidifying char matrix from the heavier components. The net results are

the deformed, swollen, char residues pockmarked with "frozen" blowholes of various shapes and sizes.

If bituminous coal particles come into contact with one another during their short-lived plastic stage, they will stick together to form large agglomerates. At high dust concentrations, the collision frequency between particles increases and the probability of collision during the short time the particles are in the plastic stage becomes high. The residues observed after explosions at high concentrations are large, coked, agglomerated masses that have little resemblance in size or shape to the original coal particles.

The temperature-time histories experienced by the coal particles during such explosions involve temperatures in the range of 1,500 to 2,000 K for times of the order of several tenths of a second (5, 13), although the time the particle spends in the flame front is much shorter. The corresponding energy flux to the particles from flame front heating is in the range of 30 to 300 W/cm^2. The effects displayed in the SEM micrographs of residues from the 8-L chamber explosions are therefore integral effects that occur over relatively long time scales compared to the reaction time scales within the active flame front. It is possible to simulate the coal pyrolysis and devolatilization processes occurring within a flame front on a time scale that matches the coal particle residence time and heating flux and that avoids the subsequent exposure in the burned gas fireball during the longer time scale. This has been done with the high-power CO_2 laser operating at a flame flux level of approximately 80 W/cm^2 in a pulse mode that controls the exposure time.

A theory (15, 17) to describe the devolatilization and combustion of coal dusts based on results obtained from the electron microscopic investigation of dust residues as well as on other flammability data was developed, and good agreement with experimental data was achieved.

The contribution of microscopy, and electron microscopy in particular, to the science of combustion can be extremely valuable in avoiding errors in theory. Consider, for example, recent studies (22, 32) on the ignition behavior of coal particles (3 to 25 μm in size) in a shock tube at temperatures of 1,700 to 2,200 K. In those studies, the change in light transmission through the dust cloud on the time scale of milliseconds was used to follow the reaction rate. A surface oxidation rate was inferred, using a shrinking sphere model for the particles in the burning dust cloud. As a result, activation energies and reaction orders were inferred, with the assumption that the optical diameter of each particle diminished uniformly as it reacted. However, direct microscopic evidence of many other investigators, noted previously in the Discussion section, showed quite clearly that in the first several milliseconds the coal combustion process proceeds with essentially no change in the particle diameter, or with an increase in diameter. This initial process involves the devolatilization of the particle, which leaves a charred residue that is at least the same size as the original coal particle from which it was generated. In particular, Lightman and Street (24) observed the formation of cenospheres from bituminous coal particles in a shock tube at similar temperatures. Obviously, the available microscopic evidence contradicts the shrinking sphere model. The observed light transmission changes were thus probably unrelated to the rate of combustion reaction and are most likely caused by other processes.

CONCLUSION

The SEM together with its X-ray accessory equipment is very useful in coal dust explosion research. It provides information concerning the heating, devolatilization, and combustion of coals and other carbonaceous dusts. Dusts of different volatile content behave differently, as evidenced by the resulting surface characteristics. In addition to combustible dusts, the SEM is useful in the study of inhibitors and for qualitative and semiquantitative chemical analyses.

The SEM is also a useful tool in investigations of mine explosion disasters. Comparison of particles collected at disaster sites with those from laboratory explosion studies assists in determining the extent and causes of disasters.

REFERENCES

1. American Society for Testing and Materials. Standard Test Method for Volatile Matter in the Analysis Sample of Coal and Coke. D3175-77 in 1981 Annual Book of ASTM Standards, Part 26: Gaseous Fuels; Coal and Coke; Atmospheric Analysis. Philadelphia, Pa., 1981, pp. 372-375.

2. Beiser, A. Concepts of Modern Physics. McGraw-Hill, New York, 1963, 405 pp. (ch. 3).

3. Born, M., and E. Wolf. Principles of Optics. Pergamon Press, New York, 5th ed., 1975, pp. 333-335, 396, 414-419.

4. Cashdollar, K. L. Three Wavelength Pyrometer for Measuring Flame Temperatures. Appl. Opt., v. 18, 1979, pp. 2595-2597.

5. Cashdollar, K. L., and M. Hertzberg. Infrared Pyrometers for Measuring Dust Explosion Temperatures. Opt. Eng., v. 21, 1982, pp. 82-86.

6. Cashdollar, K. L., M. Hertzberg, and C. D. Litton (assigned to U.S. Department of the Interior). Multichannel Infrared Pyrometer. U.S. Pat. 4,142,417, Mar. 6, 1979.

7. Cashdollar, K. L., I. Liebman, and R. S. Conti. Three Bureau of Mines Optical Dust Probes. BuMines RI 8542, 1981, 26 pp.

8. Conti, R. S., K. L. Cashdollar, I. Liebman, and M. Hertzberg. Thermal Ignition of Dust Clouds. Pres. at Fall Technical Meeting of the Eastern Section: The Combustion Institute, Pittsburgh, PA., Oct. 27-29, 1981, 4 pp.; available from Pittsburgh Research Center, Bureau of Mines, Pittsburgh, Pa.

9. Ditchburn, R. W. Light. Academic Press, London, 3d ed., 1976, pp. 255, 270, 277.

10. Elam, R. A., C. E. Lester, A. O'Rourke, R. A. Strahin, T. J. Thompson, and E. M. Kawenski. Underground Coal Mine Explosion. Dutch Creek No. 1 Mine, April 15, 1981. Mining Safety and Health Administration Report of Investigation, ID No. 05-00301, 55 pp. plus 22 appendixes.

11. Goldstein, J. I., and H. Yakowitz (eds.). Practical Electron Microscopy. Plenum Press, New York, 1975, 582 pp.

12. Helwig, N. Investigations on the Influence of Particle Size on the Progress of Coal-Dust Explosions. Staub, v. 2, 1966, pp. 25-31.

13. Hertzberg, M., K. L. Cashdollar, and C. P. Lazzara. The Limits of Flammability of Pulverized Coals and Other Dusts. Paper in Eighteenth Symposium (International) on Combustion. The Combustion Institute, Pittsburgh, Pa., 1981, pp. 717-729.

14. Hertzberg, M., K. L. Cashdollar, C. P. Lazzara, and A. C. Smith. Inhibition and Extinction of Coal Dust and Methane Explosions. BuMines RI 8708, 1982, 29 pp.

15. Hertzberg, M., K. L. Cashdollar, D. L. Ng, and R. S. Conti. Domains of Flammability and Thermal Ignitability for Pulverized Coals and Other Dusts: Particle Size Dependences and Microscopic Residue Analyses. Paper in Nineteenth Symposium (International) on Combustion. The Combustion Institute, Pittsburgh, Pa., 1983, pp. 1169-1180.

16. Hertzberg, M., K. L. Cashdollar, and J. J. Opferman. The Flammability of Coal Dust-Air Mixtures: Lean Limits, Flame Temperatures, Ignition Energies, and Particle Size Effects. BuMines RI 8360, 1979, 70 pp.

17. Hertzberg, M., J. K. Richmond, and K. L. Cashdollar. Flammability Limits and the Extinguishment of Explosions in Gases, Dusts, and Their Mixtures: Theory, Experiment, and the Problem of Scale. Proc. Colloque Internat.: Berthelot-Vieille-Mallard-LeChatelier, 1st Specialists Meeting (Internat.) of the Combustion Inst., Bordeaux, France, July 20-24, 1981. French Section of the Combustion Institute, Orleans, France, 1981, pp. 202-210.

18. Horton, M. D., F. P. Goodson, and L. D. Smoot. Characteristics of Flat, Laminar Coal-Dust Flames. Combust. Flame, v. 28, 1977, pp. 187-195.

19. Kobayashi, H., J. B. Howard, and A. F. Sarofim. Coal Devolatilization at High Temperatures. Paper in Sixteenth Symposium (International) on Combustion. The Combustion Institute, Pittsburgh, Pa., 1977, pp. 411-425.

20. Kuchta, J. M., V. R. Rowe, and D. S. Burgess. Spontaneous Combustion Susceptibility of U.S. Coals. BuMines RI 8474, 1980, 37 pp.

21. Lee, C. K., and J. R. Diehl. Combustion of Irradiated Dry and Wet Oak. Combust. Flame, v. 42, 1981, pp. 123-138.

22. Lester, T. R., W. R. Seeker, and J. F. Merklin. The Influence of Oxygen and Total Pressure on the Surface Oxidation Rate of Bituminous Coal. Paper in Eighteenth Symposium (International) on Combustion. The Combustion Institute, Pittsburgh, Pa., 1981, pp. 1257-1265.

23. Liebman, I., R. S. Conti, and K. L. Cashdollar. Dust Cloud Concentration Probe. Rev. Sci. Instr., v. 48, 1977, pp. 1314-1316.

24. Lightman, P., and P. J. Street. Microscopic Examination of Heat Treated Pulverized Coal Particles. Fuel, v. 47, 1968, pp. 7-28.

25. Lyons, J. W. The Chemistry and Uses of Fire Retardants. Wiley-Interscience, New York, 1970, 462 pp. (ch. 2).

26. McLean, M. J., D. R. Hardesty, and J. H. Pohl. Direct Observations of Devolatilizing Pulverized Coal Particles in a Combustion Environment. Paper in Eighteenth Symposium (International) on Combustion. The Combustion Institute, Pittsburgh, Pa., 1981, pp. 1239-1248.

27. Milne, T. A., and J. E. Beachey. Exploratory Studies of Flame and Explosion Quenching (Contract HO122127, Midwest Res. Inst.). BuMines OFR 112-77, June 25, 1976, 254 pp.; NTIS PB 268 695/AS.

28. Moseley, H. The High Frequency Spectra of Elements. Phil. Mag., v. 26, 1913, p. 1024.

29. Newall, H. E., and F. S. Sinnatt. The Carbonisation of Coal in the Form of Fine Particles. I. The Production of Cenospheres. Fuel Sci. Pract., v. 3, 1924, pp. 424-434.

30. Richmond, J. K., I. Liebman, and L. F. Miller. Effect of Rock Dust on Explosibility of Coal Dust. BuMines RI 8077, 1975, 34 pp.

31. Seeker, W. R., G. S. Samuelsen, M. P. Heap, and J. D. Trolinger. Paper in Eighteenth Symposium (International) on Combustion. The Combustion Institute, Pittsburgh, Pa., 1981, pp. 1213-1226.

32. Seeker, W. R., D. G. Wegener, T. W. Lester, and J. F. Merklin. Single Pulse Shock Tube Studies of Pulverized Coal Ignition. Paper in Seventeenth Symposium (Interntional) on Combustion. The Combustion Institute, Pittsburgh, Pa., 1979, pp. 155-166.

33. Smoot, L. D., and M. D. Horton. Exploratory Studies of Flame and Explosion Quenching. Vol. 1 (Contract G0177034, Brigham Young Univ.). BuMines OFR 104-82, Mar. 31, 1978, 315 pp.

34. Smoot, L. D., M. D. Horton, and G. A. Williams. Propagation of Laminar Pulverized Coal-Air Flames. Paper in Sixteenth Symposium (International) on Combustion. The Combustion Institute, Pittsburgh, Pa., 1977, pp. 375-387.

35. Street, P. J. Microscopical Examination of U.S. Bureau of Mines Pulverized Coal Explosion Residue. Private communication, July 20, 1982; available upon request from D. Ng, Bureau of Mines, Pittsburgh, Pa.

36. Street, P. J., R. P. Weight, and P. Lightman. Further Investigations of Structural Changes Occurring in Pulverized Coal Particles During Rapid Heating. Fuel, v. 48, 1969, pp. 343-365.

37. Tewarson, A. and J. S. Newman. An Experimental Investigation of the Fire Hazards Associated With Timber Sets in Mines. Paper in Underground Metal and Nonmetal Fire Protection. Proceedings: Bureau of Mines Technology Transfer Seminars, Denver, Colo., Nov. 3, 1981, and St. Louis, Mo., Nov. 6, 1981. BuMines IC 8865, 1981, pp. 86-103.

38. Unger, P. E., and E. M. Suuberg. Modeling the Devolatilization Behavior of a Softening Bituminous Coal. Paper in Eighteenth Symposium (International) on Combustion. The Combustion Institute, Pittsburgh, Pa., 1981, pp. 1203-1211.

39. Wells, O. C. Scanning Electron Microscopy. McGraw-Hill, New York, 1974, 421 pp.

40. Zworykin, V. K., J. Hillier, and R. L. Snyder. A Scanning Electron Microscope. American Society for Testing and Materials, Philadelphia, Pa., Bull. 117, 1942, pp. 15-23.

☆U.S. GOVERNMENT PRINTING OFFICE: 1983-605-015/39

INT.-BU.OF MINES,PGH.,PA. 26913

H32 84

THE LIBRARY OF CONGRESS

DEC 83
N. MANCHESTER,
INDIANA 46962

LIBRARY OF CONGRESS
0 002 959 874 5